Sensing the wind profile

Pena Diaz, Alfredo

Publication date:
2009

Document Version
Publisher's PDF, also known as Version of record

Sensing the wind profile

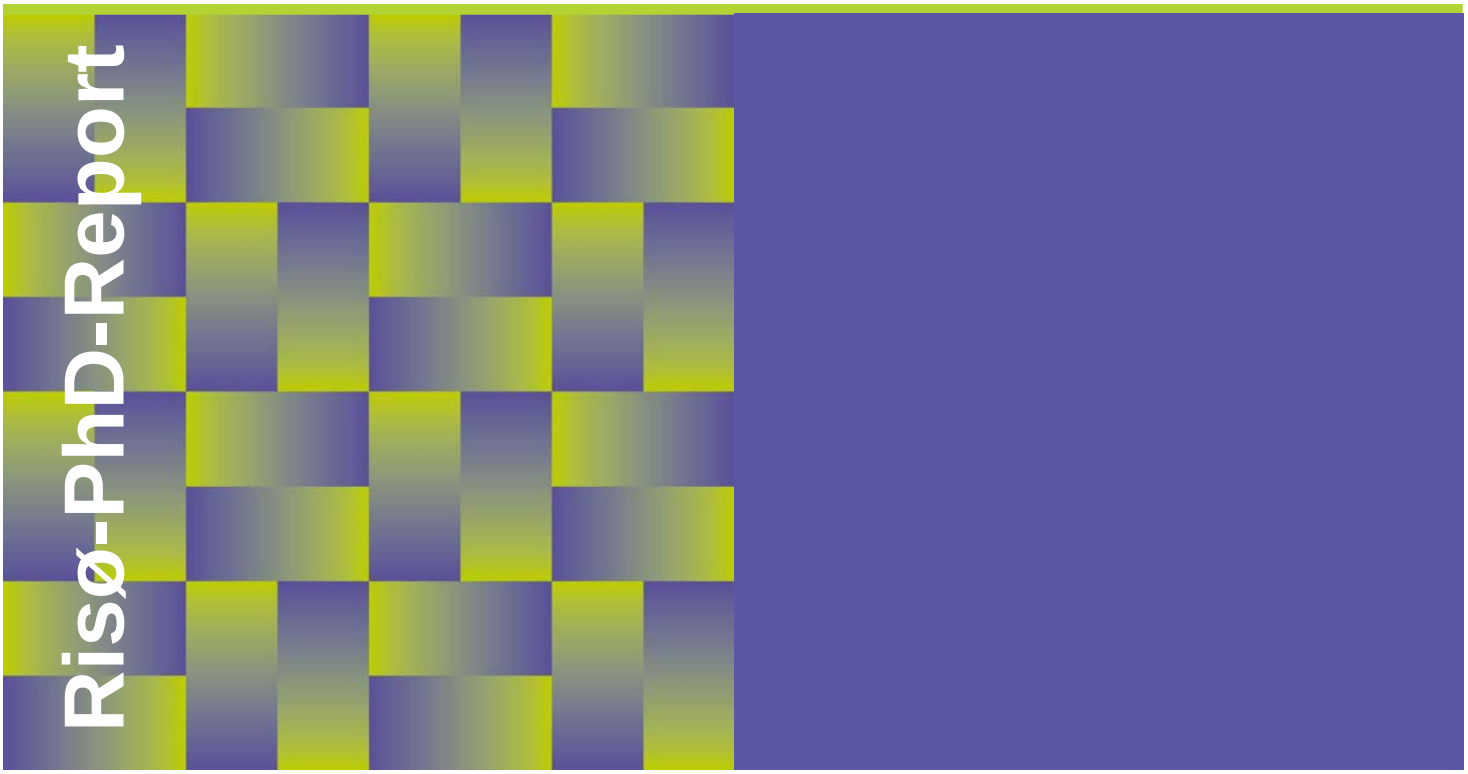

Alfredo Peña
Risø-PhD-45(EN)
March 2009

Risø DTU
National Laboratory for Sustainable Energy

DET NATURVIDENSKABELIGE FAKULTET
KØBENHAVNS UNIVERSITET

Author: Alfredo Peña[1,2]

Title: Sensing the wind profile

1 Risø National Laboratory for Sustainable Energy,
Technical University of Denmark, Roskilde, Denmark
2 Department of Geography and Geology,
Faculty of Science{University of Copenhagen,
Copenhagen, Denmark

This thesis is submitted in partial fulfillment of the requirements for the Ph.D. degree at the University of Copenhagen.

Abstract (max. 2000 char.):
This thesis consists of two parts. The first is a synopsis of the theoretical progress of the study that is based on a number of journal papers. The papers, which constitute the second part of the report, aim to analyze, measure, and model the wind prole in and beyond the surface layer by combining observations from cup anemometers with lidars. The lidar is necessary to extend the measurements on masts at the Horns Rev offshore wind farm and over at land at Høvsøre, Denmark. Both sensing techniques show
a high degree of agreement for wind speed measurements performed at either sites. The wind speed measurements are averaged for several stability conditions and compare well with the surface-layer wind profile. At Høvsøre, it is sufficient to scale the wind speed with the surface friction velocity, whereas at Horns Rev a new scaling is added, due to the variant roughness length. This new scaling is coupled to wind prole models derived for
flow over the sea and tested against the wind proles up to 160 m at Horns Rev. The models, which account for the boundary-layer height in stable conditions, show better agreement with the measurements than compared to the traditional theory. Mixing-length parameterizations for the neutral wind prole compare well with length-scale measurements up to 300 m at Høvsøre and 950 m at Leipzig. The mixing-length-derived wind proles strongly deviate from the logarithmic wind prole, but agree better with the wind speed measurements. The length-scale measurements are compared to the length scale derived from a spectral analysis performed up to 160 m at Høvsøre showing high agreement. Mixing-length parameterizations are corrected to account for stability and used to derive wind prole models. These compared better to wind speed measurements up to 300 m at Høvsøre than
the surface-layer wind prole. The boundary-layer height is derived in near-neutral and stable conditions based on turbulent momentum
uxes only and in unstable conditions based on profiles of aerosol backscatter from ceilometer measurements. The lidar measuring technique is used to estimate momentum flux, showing high agreement compared to measurements at Høvsøre and Horns Rev when the filtering effects of the lidar are taken into account.

Risø-PhD-45(EN)
March 2009

ISBN 978-87-550-3709-0

Contract no.:

Group's own reg. no.:

Sponsorship:
The Danish Council for Strategic Research and the Wind Energy Educational Programme at Risø DTU

Cover :

Pages: 80
Tables: 2
References: 91

Information Service Department
Risø National Laboratory for Sustainable Energy
Technical University of Denmark
P.O.Box 49
DK-4000 Roskilde
Denmark
Telephone +45 46774004
bibl@risoe.dk
Fax +45 46774013
www.risoe.dtu.dk

Contents

Acknowledgements

I would like to express all my gratitude to the people of the Wind Energy Division at Risø, to my colleagues at the Meteorology Program, and in particular to my supervisors Charlotte Bay Hasager and Sven-Erik Gryning. Charlotte gave me the opportunity to work at Risø, the liberty to explore the areas in meteorology that I thought were relevant for my PhD study, and the trust to develop my studies in a free, friendly, and optimum workplace during the last three years. Sven-Erik has been extremely important and helpful, because of his constant scientific input, the interesting discussions, and because he made me understand and appreciate the significance of the wind profile. I would like to thank the scientific input and continuous help at Risø of Jakob Mann, Michael Courtney, Hans E. Jørgensen, and Søren Larsen. I also thank Charlotte and Hans for the permission to write part of this report in Colombia.

Thanks to my PhD fellows and colleges at Risø, and in particular to Pierre-Elouan Réthoré for his invaluable friendship, Ferhat Bingöl and Eleni Markou that have been always very close to me, Claire Vincent for her suggestions and inputs concerning English language in most of my manuscripts (including this PhD report), and Rozenn Wagner and Jacob B. Jørgensen for their support and help.

I would like to thank my supervisor Henrik Søgaard at the University of Copenhagen for his help, criticisms, and suggestions.

I also acknowledge the funding of my PhD from The Danish Council for Strategic Research trough the project “12 MW” Sagsnr. 2104-05-0013.

Thanks to the friendship and help of Zascha Straube and Sandra Kumiko Ito, which have tried to entertain me during my life in Denmark.

Finally, I would like to thank the constant support and love of my family in Colombia.

1 Introduction

In the geographical description of atmospheric flow, whether over land or sea, flat or mountainous terrain, bare or forested surfaces, the wind profile is important. The wind profile, i.e. the wind speed variations as a function of height, varies in the landscape and varies through time. For the observation of the wind profile, frequent and accurate wind speed observations are required. The present work extends previous knowledge of the wind profile through a micro-meteorological approach, combining physical theory with field observations and data analysis.

The modern study of the atmospheric boundary layer (ABL) began after the advancement of fluid dynamics in the second part of the 19th century, namely after the works of Reynolds (1883) on laminar and turbulent motion of viscous flows, and at the beginning of the 20th century with the works on boundary-layer flows of Taylor (1915) and Prandtl (1925). Since then, field experiments have been prepared to demonstrate the theoretical work, while part of the theory has been developed from the observations. Such experiments require the use of sensors to observe the characteristics of the ABL. As reported by Lumley and Yaglom (2001), hot-wire anemometers were already used for air velocity measurements in the first decade of the 20th century in order to study developed turbulence in the atmosphere at high Reynolds numbers. This type of anemometers falls into the category known as in situ sensors that can be mounted on the ground, on masts, towers, balloons, or aircraft (Kaimal and Finnigan 1994). Cup and sonic anemometers, which have been improved during the last 50 years, are also part of the in situ sensors and both probably constitute the most traditional and used instruments in micrometeorology, i.e. for surface and lower boundary-layer studies. This is due to their robustness, simplicity, reliability, high accuracy, and time and spatial resolution (Kaimal et al. 1968; Kristensen 1993).

However, traditional instruments suffer of some drawbacks related to their placement. Tower and boom effects are always present in the measurements and although they have been studied for a long time (Izumi and Barad 1970), each installation must be examined to account for anemometer over- and under-speeding, due to shading effects. Another disadvantage, probably the most important in connection to this study, is that for heights above 80–100 m, mast installation becomes expensive and logistically complex. These problems add a special value to the second category of sensors, the so-called remote sensing techniques, because they have an increased observational range and do not require mast mounting. Remote sensors, which work based on acoustic, microwave, and optical propagation, are nevertheless more expensive, have lower accuracy, reliability, and limitations regarding the temporal and spatial resolution.

The need for measurements at high levels in the atmosphere and, particularly, the increasing use of wind energy have accelerated the development of lidars in the last years. These remote sensors, which are based on the scattering of light in the atmosphere, have profited from the advancement in fiber optic components, laser technology, and electronics, becoming less expensive and as accurate as the cup/sonic anemometers for wind speed measurements, as shown in Smith et al. (2006), Antoniou et al. (2006), Kindler et al. (2007), and Mann et al. (2007) for flow over flat land, over sea, and over forests. The importance of the lidars for this study is basically related to their ability to perform measurements at different heights, from which the wind profile can be derived.

It is the sensing of the wind profile that is the major objective of this thesis. Sensing refers to the observation, analysis, description, and modeling of the wind profile in and beyond the atmospheric surface layer, which is here performed by combining measurements of traditional instruments with high accurate remote sensors, such as the lidar wind profilers. Extended wind speed measurements, from surface-layer to beyond surface layer observations, and accurate wind profile models for the ABL are of great importance, not only for wind resource assessment used extensively for wind energy exploitation, but also

for the understanding of the global and regional climate, for weather forecasting, agricultural and dispersion modeling, architectural design, and wind engineering. The wind profile models are derived based on mixing-length theory, introduced by Prandtl (1932), and it is shown that the theory, which is proposed for the lower part of the boundary layer, can be extended to the entire boundary layer and for different atmospheric stability conditions. For practical application, the findings of this study are most useful for the wind power industry, which still uses a single cup anemometer to assess the potential wind resource of an area that may cover the first 200 m of the ABL, thus, requiring a detailed description of the wind profile, which is not provided by the traditional practices.

This thesis consists of two parts. The first corresponds to a synopsis of the major subjects considered during the PhD study. It has the intention to make a continuous reference of the journal papers that have been prepared during the last three years and to recreate their line of thinking by approaching the theory. It also provides results and analysis, which are not included in the journal papers. The synopsis has been divided into four main sections. Section 2 describes the general characteristics of the ABL and the surface layer, and introduces the wind profile, the influence of stability, and the mixing-length concept. Section 3 describes two sites in Denmark where measurements of the wind profile and turbulence were performed. Section 4 is related to the remote sensing techniques used for the observation of the wind profile and the boundary-layer height. Finally, Section 5 illustrates the analysis of the wind profile in the surface layer for flow over flat land and over the sea, and the characteristics and modeling of the mixing length and the wind profile beyond the surface layer.

The second part of the thesis corresponds to a collection of journal papers. A brief summary of them is given here:

- **Paper I** Comparisons of horizontal mean wind speeds from cup anemometers on the masts at the Horns Rev wind farm with lidar measurements are illustrated. They show high agreement and correlations, allowing the extension of the wind profile observed at the masts with the lidar observations up to 160 m for different upwind sectors. The extended profiles, averaged over all stability conditions and roughness lengths, agree well with the logarithmic wind profile.

- **Paper II** Wind speed profiles observed within a free upwind sector at Horns Rev are analyzed using a tool that extracts the dependency of the roughness of the sea on the wind speed, based on the roughness model of Charnock (1955), allowing the study of the marine wind profiles for different stability conditions, in the same fashion as the wind profile is analyzed for constant roughness length over flat and homogenous terrain.

- **Paper III** Using the tool developed in Paper II, extended lidar/cup wind profiles at Horns Rev up to 160 m are analyzed and it is shown that these compare well to marine wind profile models derived from a mixing-length parametrization that accounts for the boundary-layer height in stable conditions, which is estimated accounting for the contribution of mechanical turbulence only.

- **Paper IV** The neutral wind profile for flat and homogeneous terrain is derived using a number of mixing-length parameterizations that show good agreement with measurements of the length scale of the Leipzig wind profile up to 950 m and of the Høvsøre wind profile up to 300 m from extended lidar/cup anemometer observations. The derived wind profiles agree well with the wind speed measurements for the two datasets and show a strong deviation from the logarithmic wind profile. The length scale derived from the wind speed observations is related to the length scale derived from a spectral analysis of the turbulence measurements up to 160 m at Høvsøre.

- **Paper V** Two of the mixing-length parameterizations analyzed in Paper IV are extended to account for diabatic conditions and used to derive wind profile models for the entire ABL. The models are compared to wind speed measurements up

to 300 m at Høvsøre for a wide range of atmospheric stability conditions, showing better agreement when compared to the traditional surface-layer wind profile. The boundary-layer height needed for the models is estimated from turbulence measurements in neutral and stable conditions and from ceilometer observations in unstable conditions.

- **Paper VI** A number of remote sensing techniques used in offshore wind energy are described. Lidar and sodar measurements show capabilities for the observation of the marine wind profile, whereas SAR and scatterometer offer a basis for detailed offshore wind resource estimation, covering a large observational area.
- **Paper VII** The momentum flux in and above the surface layer is observed using two lidar wind profilers over flat and homogeneous terrain and over the sea in Denmark. The comparison of the momentum flux with sonic anemometer measurements show good agreement for several heights up to 160 m. The filtering effect on the turbulence of the lidars is estimated using the model in Mann (1994) and this is in agreement with the measurements.

In addition to the journal papers, a number of conference papers, a book chapter, and a technical report were prepared. These are not referenced in the thesis, because they correspond to the first stages or summaries of the results of the journal papers. These are:

1. **Peña, A.**, C. B. Hasager, S.-E. Gryning, M. Courtney, I. Antoniou, T. Mikkelsen, and P. Sørensen, 2007: On the study of wind energy at great heights using remote sensing techniques. *Proc. of the European Wind Energy Conf.*, [http://www.ewec2007proceedings.info/allfiles2/125_Ewec2007fullpaper.pdf], Milan.
2. **Peña, A.**, C. B. Hasager, S.-E. Gryning, M. Courtney, I. Antoniou, T. Mikkelsen, and P. Sørensen, 2007: Offshore wind using remote sensing techniques. *J. Phys: Conf. Proc.* **75**, 012038 (11 pp).
3. **Peña, A.**, S. E. Gryning, and C. B. Hasager, 2007: Lidar observations of offshore winds at future wind turbine operating heights. *Proc. of the European Offshore Wind Conf.*, [http://www.eow2007proceedings.info/allfiles2/176_Eow2007fullpaper.pdf], Berlin.
4. Ohsawa, T., A. Kataoka, D. Heinemann, B. Lange, **A. Peña**, and C. B. Hasager, 2007: Derivation and application of an empirical equation to estimate hub-height wind speed from sea surface wind speed. *Proc. of the European Offshore Wind Conf.*, [http://www.eow2007proceedings.info/allfiles2/244_Eow2007fullpaper.pdf], Berlin.
5. Hasager, C. B., **A. Peña**, T. Mikkelsen, M. Courtney, I. Antoniou, S.-E. Gryning, P. Hansen, and P. B. Sørensen, 2007: 12MW Horns Rev experiment. Tech. Rep. Risø-R-1506(EN), Risø National Laboratory, 83 pp.
6. **Peña, A.**, 2008: Wind speed distributions in neutral atmospheres over homogeneous terrain. *Extended abstract for the 4th PhD seminar on Wind Energy in Europe*, Magdeburg.
7. **Peña, A.**, S.-E. Gryning, and C. B. Hasager, 2009: Extending the wind profile much higher than the surface layer. *Proc. of the European Wind Energy Conf.*, Marseille.
8. Hasager, C. B., M. B. Christiansen, **A. Peña**, J. Badger, I. Antoniou, M. Nielsen, P. Astrup, and M. Courtney, 2009: Advances in offshore wind resource estimation. *Advances in Wind Energy Conversion Technology*, S. Mathew and G. S. Philip, Eds., Springer-Verlag. In preparation.

2 The Atmospheric Boundary Layer

The atmospheric boundary layer is the region of the Earth's atmosphere that is directly influenced by the surface. Frictional drag, heat transfer, and evaporation are forcings produced by the interaction of air masses with the Earth's surface and the strength of these forcings determines the thickness of the ABL, z_i. Turbulence in the ABL is primarily produced by wind shear, mainly generated by friction with the surface, and buoyancy, mainly from the heating of the ground.

Three basic regimes in a homogeneous boundary layer can be distinguished depending on the dominant source of turbulence:

- Convective or unstable: The convectively driven turbulence is mainly generated from heat transfer from the warm ground surface. Insolation is the main source of buoyancy at the surface, therefore, the convective boundary layer (CBL) starts growing in the morning after sunrise and in a cloud-free day reaches its maximum depth in the late afternoon. Large turbulent 'eddies' characterize the CBL, which is extended 1–2 km above ground in middle latitudes.
- Stable: Statically stable air, typically from cooling of the surface at night times, tends to suppress turbulence. A stable boundary layer (SBL) is formed, typically within the first 100–200 m above the ground, where the flow is characterized by strong wind shear, small eddies, and occasional wave activity. Winds above the SBL may accelerate to super-geostrophic speeds commonly known as low-level jet (LLJ).
- Neutral: Although neutral conditions are not well-defined in the ABL, the flow can be characterized by the combination of wind shear and no convection. In the neutral boundary layer, the heat flux is close to zero and the wind speeds tend to be very high near the surface, therefore, these are ideal conditions for wind energy harvesting.

The structure of the ABL is illustrated in Figure 1 during an ideal evolving diurnal cycle. The surface layer, which covers the lower 5–10% of the ABL, is also shown in the figure. Within the surface layer the momentum, heat, and moisture fluxes are approximately constant with height, z, and the vertical gradients of wind, temperature, and humidity are generally strong. Before sunset, the entrainment zone is continuously displaced to lower heights in Figure 1, due to subsidence in the atmosphere.

Above the surface layer within the CBL, the air is well mixed where relatively constant profiles of virtual potential temperature, Θ_v, and horizontal wind speed, U, are observed (see Figure 2) until it reaches the entrainment zone that results from the interaction of the stable free atmosphere and the turbulent thermals and eddies at the top of the CBL. The temperature increases with height in the entrainment zone resulting in a so-called inversion. Normally, z_i is taken in the intermediate part of the entrainment zone, when used as a parameter for CBL modeling.

Above the surface layer within the SBL, the profiles of temperature and wind speed are not constant (see Figure 3), in contrast with their behavior in the CBL, and turbulence is suppressed until the smaller eddies reach the residual layer marking the height of the SBL. The residual layer is a near-neutral air layer where turbulence decays from the formerly CBL and is capped by the former entrainment zone. Several inversions may occur within the residual layer. It is between the residual layer and the SBL where LLJs may form, therefore, the height where the wind speed reaches a maximum is a parameter often used for the determination of z_i.

Ideal ABL-regimes, i.e. stationary neutral, convective, or stable boundary layers, are difficult to find in the nature. Due to its dynamics, the ABL is a mixture of all kinds of stability conditions. Therefore, the approach in this summary–unless otherwise stated– and used particularly in **Paper II**, **III**, **IV**, **V**, and **VII**, is to classify the atmospheric

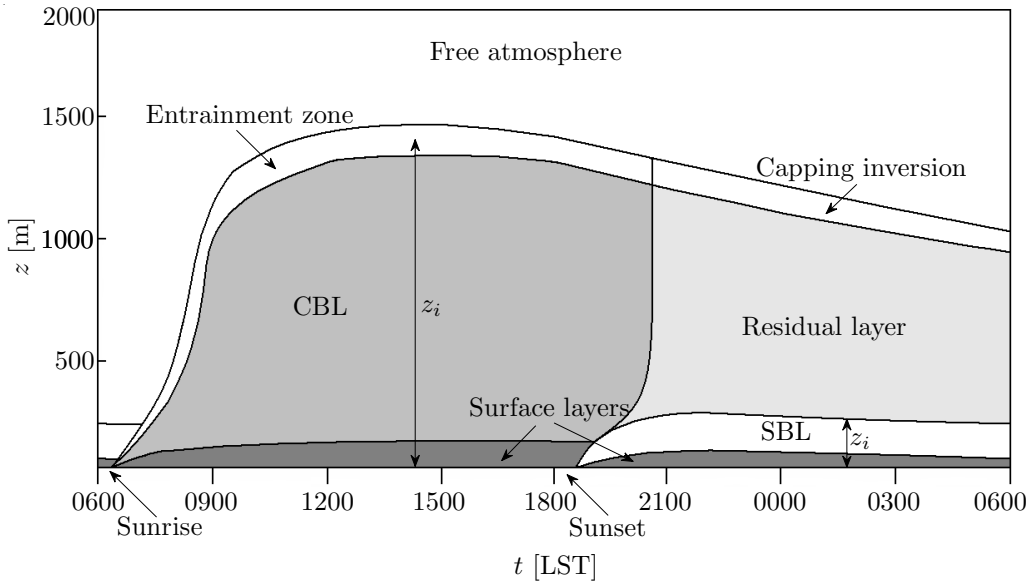

Figure 1. The evolution of the atmospheric boundary layer with height during an ideal diurnal cycle. The convective boundary layer (CBL), stable boundary layer (SBL), surface layer, residual layer, entrainment zone, and boundary-layer height, z_i, are distinguished. Local standard time (LST) is used in the x-axis.

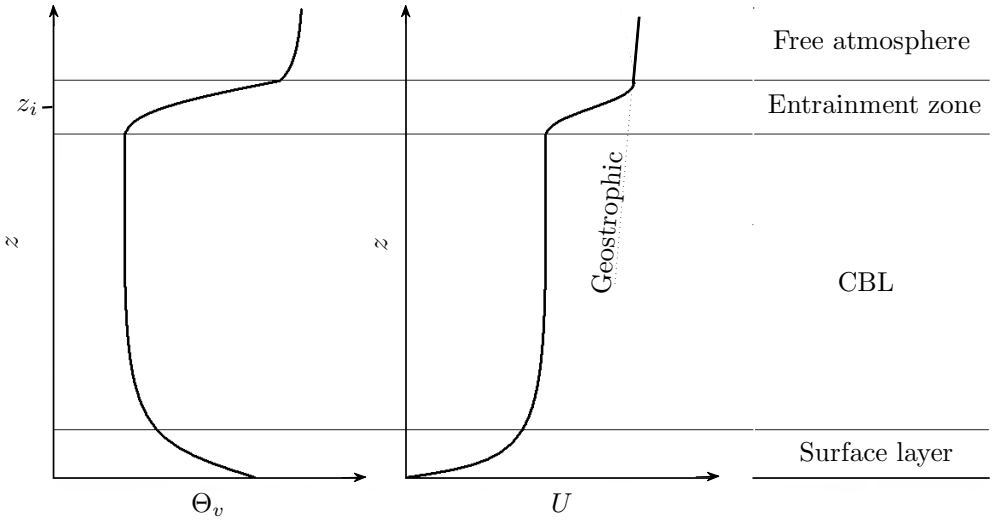

Figure 2. Profiles of virtual potential temperature, Θ_v, and horizontal wind speed magnitude, U, for an idealized convective boundary layer.

flow according to stability conditions, based on measurements close to the ground, i.e. in the surface layer.

The diurnal variation of the structure of the ABL can be followed, e.g. using ceilometer observations of the backscatter light from aerosols dispersing in the air, as illustrated in Figure 4.[1] In analogy to Figure 1, during two consecutive cloud-free summer days, the aerosols moved upwards after sunrise and high concentrations of pollutants reached heights $\approx$ 1000–1500 m at 1500–2100 LST. The air and the aerosols moved towards the ground after sunset, but some aerosol structures were still present from the formerly CBL, showing several residual layers.

From similarity theory, the structure of the ABL depends on the height above ground,

[1] A description of the ceilometer observations is given in Section 4.2.

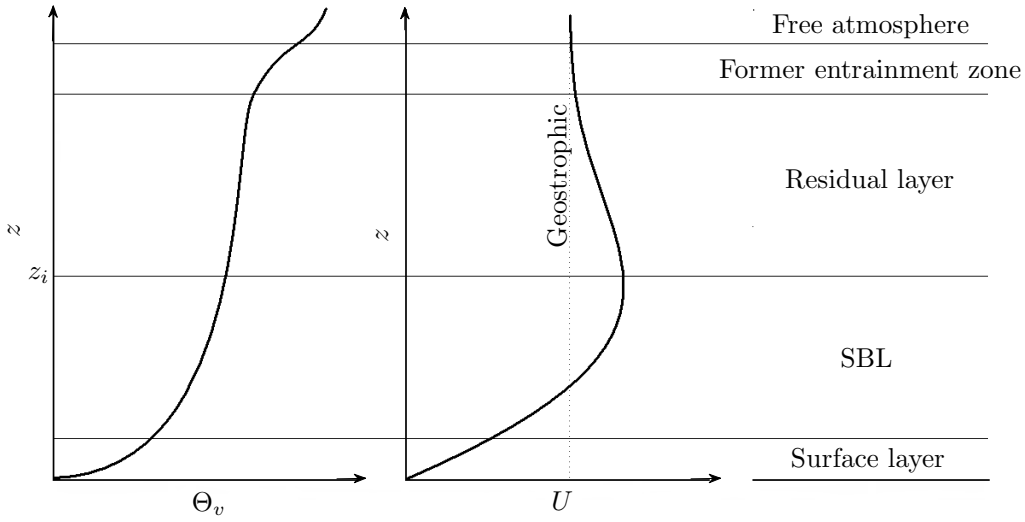

Figure 3. As Figure 2, but for an idealized stable boundary layer.

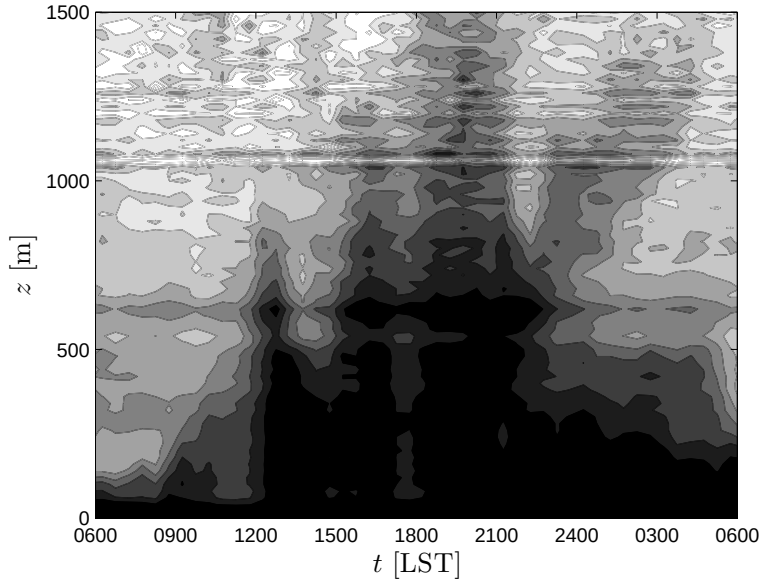

Figure 4. Aerosol backscatter in the atmosphere during a diurnal cycle over two consecutive summer days (11 May 2006–12 May 2006) from ceilometer observations at Risø DTU in Roskilde, Denmark. The darker the color the higher the aerosol concentration.

z, the boundary-layer height, z_i, and the Obukhov length, L, which is approximately the height where production of mechanical and convective turbulence is equal (see Section 2.1). A diagram that divides the ABL into different domains each characterized by a set of scaling parameters related to z, z_i, and L was presented in Holtslag and Nieuwstadt (1986) and Gryning et al. (1987) and is illustrated in Figure 5. From the figure, it is shown that certain scales may become irrelevant for ABL parametrization, depending on the distance from the ground and the stability of the atmosphere, illustrating the importance of the determination of z_i and L for this study.

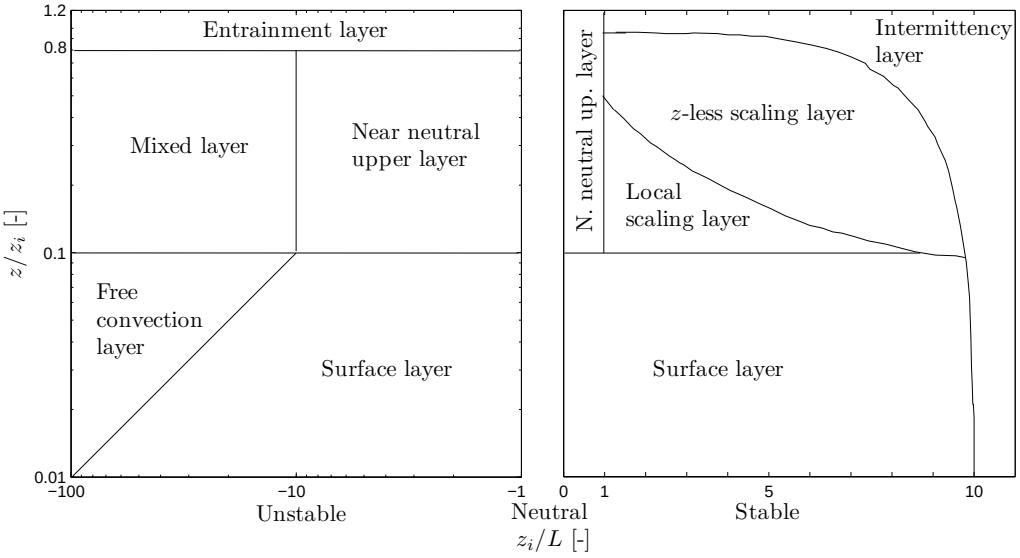

Figure 5. Scaling regimes of the atmospheric boundary layer. A detailed description is found in Holtslag and Nieuwstadt (1986) and Gryning et al. (1987).

2.1 The Surface Layer

The surface layer extends only a few meters above the ground in very stable conditions and might grow beyond 100 m in very convective situations. As mentioned above, the variation of the vertical fluxes of momentum, heat, and moisture within this layer are relatively constant with height and the wind and temperature gradients are large. Therefore, it is not only for practical purposes–most meteorological masts do not exceed 100 m–, but also due to signal strength and quality that the observation of atmospheric variables is easier when performed close to the ground.

Obukhov (1946) found a scaling parameter that describes turbulent exchange processes from the combination of the parameters g/T (g and T are the gravitational acceleration and temperature, respectively), u_* (a velocity scale or friction velocity), and $H/(c_p\rho)$ (H, c_p, and ρ are the kinematic heat flux, specific heat, and density of the air, respectively). This scaling parameter has the dimensions of length and is known as the Obukhov length:

$$L = -\frac{{u_*}^3}{\kappa \left(\frac{g}{T}\right)\left(\frac{H}{c_p\rho}\right)} \tag{1}$$

where κ is the von Kármán constant. The Obukhov length gives in a natural way a measure of the degree of dominance of buoyancy over mechanical and shearing effects, and can therefore be used to directly characterize the stability of the atmosphere. Obukhov (1946) used the temperature of dry air to calculate the heat flux, but currently the term $H/\left(c_p\rho\right)$ in Eq. (1) is replaced by the vertical flux of virtual potential temperature $\overline{w'\Theta_v{}'}$, where w is the vertical component of the velocity, the primes represent fluctuations, and the overbar a time mean.[2] Θ_v accounts for moisture in the air and changes in air pressure (see Appendix B).

Due to the relatively constant fluxes close to the ground, L is a useful scaling parameter in the surface layer. Therefore, the temperature, friction velocity, and heat flux should be observed close to the ground–here indicated by the subindex o. The Obukhov length used along this summary and in **Paper II**, **III**, **IV**, **V**, and **VII**, is given by:

$$L = -\frac{{u_{*o}}^3 T_o}{\kappa g \overline{w'\Theta_v{}'}_o} \tag{2}$$

[2]The derivation of the Obukhov length from the budget of turbulent kinetic energy is given in Appendix A.

where T_o is the mean surface-layer temperature. The surface friction velocity is normally aligned with the mean wind close to the ground, thus, it can be computed directly as the square root of the momentum flux, $\overline{u'w'}$, in the surface layer:

$$u_{*o} = \left(-\overline{u'w'}_o\right)^{1/2} \tag{3}$$

where u is the longitudinal component of the wind velocity.

Another measurement of flow stability is the Richardson number. The so-called flux Richardson number is a dimensionless parameter that results, as the Obukhov length, from the ratio between the buoyancy and the mechanical turbulent production, namely the ratio between the two terms in the right hand side of Eq. (A-2). However, it is not often used, because it involves the ratio of the turbulent correlations, $\overline{w'\Theta_v{}'}$ and $\overline{u'w'}$, which is difficult to estimate without a sonic anemometer. Instead, the gradient Richardson number, Ri,

$$\mathrm{Ri} \propto \frac{\frac{g}{T}\frac{\partial \Theta_v}{\partial z}}{\left(\frac{\partial U}{\partial z}\right)^2} \tag{4}$$

is preferred, because it applies temperature and wind speed gradients that are assumed to be proportional to the turbulent correlations involved in the flux Richardson number. Because the observations are normally taken at discrete heights, the terms $\partial\Theta_v/\partial z$ and $\partial U/\partial z$ are approximated by Θ_{vd}/z_d and U_d/z_d, respectively, where the subindex d indicates the difference between two observational levels. The result of this approximation is the bulk Richardson number, Ri_b, given as

$$\mathrm{Ri}_b = \frac{g\Theta_{vd}z_d}{T{U_d}^2}. \tag{5}$$

Ri_b might be more appropriate than Ri, because it can be calculated from measurements between an observational height and the ground or sea levels where the wind speed is assumed to be zero. Thus, it is less sensitive to inaccurate measurements of temperature and wind speed. Both Ri and Ri_b are related to L (Deardorff 1968; Businger et al. 1971). The forms,

$$\frac{z}{L} = C_1\mathrm{Ri}_b \qquad \text{and} \tag{6}$$

$$\frac{z}{L} = \frac{C_1\mathrm{Ri}_b}{1 - C_2\mathrm{Ri}_b} \tag{7}$$

for positive and negative Ri_b values, respectively, were suggested in Grachev and Fairall (1996). Applying the values $C_1 = 10$ and $C_2 = 5$, these forms are used in **Paper III** to determine the value of L from Eq. (5) that is compared to L directly estimated from Eq. (2) from observations over the sea at Horns Rev in 2004. This comparison is needed, because there are not observations of the turbulent fluxes at the same site in 2006, which corresponds to the period where the study is concentrated, showing the usefulness of the Richardson number.

Monin-Obukhov Similarity Theory

Using similarity theory, Monin and Obukhov (1954) argued that atmospheric parameters such as gradients, variances, and covariances become universal functions of the dimensionless stability, z/L, when normalized in the surface layer by a scaling velocity–the friction velocity–and a scaling temperature, u_{*o} and Θ_{*o}, respectively. The latter is given by:

$$\Theta_{*o} = -\frac{\overline{w'\Theta_v{}'}_o}{u_{*o}}. \tag{8}$$

Here, the surface fluxes are already used, because Monin-Obukhov similarity theory (MOST) is valid in the surface layer only and within a specific range of z/L values

(Foken 2006). Two dimensionless forms appear (Stull 1988; Kaimal and Finnigan 1994):

$$\phi_m = \frac{\kappa z}{u_{*o}} \frac{\partial U}{\partial z}, \tag{9}$$

$$\phi_h = \frac{z}{\Theta_{*o}} \frac{\partial \Theta}{\partial z} \tag{10}$$

where ϕ_m and ϕ_h are the so-called dimensionless wind shear and temperature gradients, respectively. The forms of these functions cannot be predicted, but they have been determined from field experiments and are commonly known as the flux-profile relationships:

$$\phi_m = \left(1 - a_1 \frac{z}{L}\right)^{p_1}, \qquad -2 < \frac{z}{L} < 0, \tag{11}$$

$$\phi_m = 1 + b_1 \frac{z}{L}, \qquad 0 < \frac{z}{L} < 1, \tag{12}$$

$$\phi_h = c\left(1 - a_2 \frac{z}{L}\right)^{p_2}, \qquad -2 < \frac{z}{L} < 0, \tag{13}$$

$$\phi_h = c + b_2 \frac{z}{L}, \qquad 0 < \frac{z}{L} < 1 \tag{14}$$

where $a_1 = 15$, $a_2 = 9$, $b_1 = b_2 = 4.7$, $c = 0.74$, $p_1 = -1/4$, and $p_2 = -1/2$ were estimated by Businger et al. (1971) from the analysis of the Kansas experiment, whereas Högström (1988) found $a_1 = 19.3$, $a_2 = 11.6$, $b_1 = 6$, $b_2 = 7.8$, $c = 0.95$, $p_1 = -1/4$, and $p_2 = -1/2$ from observations over flat terrain in Sweden. In Figure 6 the behavior of Eqs. (11) and (12) according to Businger et al. (1971) and Högström (1988) is illustrated where the largest differences are observed under stable conditions, i.e. $0 < z/L < 1$.[3] Observations of the dimensionless wind shear, performed over flat and homogeneous terrain at Høvsøre, Denmark, are also shown in the figure. In order to estimate the wind shear, $\partial U/\partial z$, to compute Eq. (9) from the measurements, the method proposed in Högström (1988) is applied, not only for these observations at Høvsøre, but systematically in **Paper III** and **IV** (see Appendix C). The observations at Høvsøre in Figure 6, performed during three years, agree well with Eq. (11) for unstable conditions, whereas the scatter is larger for stable conditions where the findings of Businger et al. (1971) agree slightly better with the observations.

It has been argued that the differences between both experimental findings are due to flow distortion from the tower on the wind speed observations in the Kansas experiment and to the value for the von Kármán constant applied by Businger et al. (1971) ($\kappa = 0.35$), which is lower than the actual trend, $\kappa = 0.4$, derived by Högström (1988). A clear consequence of the use of a lower κ by Businger et al. (1971) is a lower dimensionless wind shear within the stable stability range, compared to the curve by Högström (1988), although Businger et al. (1971) pointed out the possibility of an overestimation of the wind shear and, thus, a slightly overestimation of the ϕ_m function in the Kansas experiment.

The variation of the ϕ_m function with stability is also shown in **Paper III** from observations over the North Sea at Horns Rev. For unstable conditions, the observations compare well with Eq. (11) using $p_1 = -1/3$ and $a_1 = 12$, which are in accordance with the theoretical limit for convective conditions (Carl et al. 1973). For stable conditions, a good agreement is established with the findings of Businger et al. (1971) as well.

The Surface-Layer Wind Profile

The wind profile in the surface layer can be derived from similarity theory using the findings of MOST. The horizontal wind shear is derived from Eq. (9):

$$\frac{\partial U}{\partial z} = \frac{u_{*o}}{\kappa z} \phi_m. \tag{15}$$

[3]Some authors prefer the limit $-1 < z/L < 0$ for the unstable ϕ_m and ϕ_h functions, which is in agreement with Figure 5.

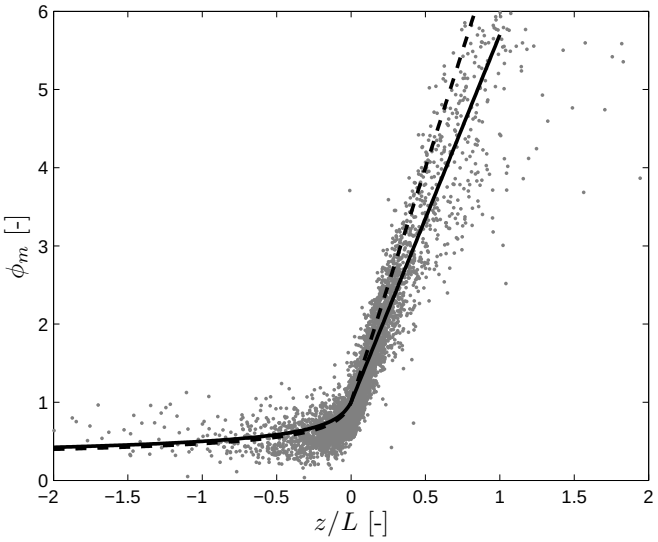

Figure 6. The dimensionless wind shear, ϕ_m, as function of the dimensionless stability, z/L. The solid lines correspond to the suggestions by Businger et al. (1971) and the dashed lines to the fit by Högström (1988) to Eqs. (11) and (12). Observations over flat land at Høvsøre, Denmark, are shown in gray markers.

As found by Businger et al. (1971), Högström (1988), and as shown in **Paper III** for flow over the sea, the ϕ_m function is close to unity in near-neutral conditions. Therefore, when integrating Eq. (15) with z for $\phi_m = 1$, the result is the traditional logarithmic wind profile:

$$U = \frac{u_{*o}}{\kappa} \ln\left(\frac{z}{z_o}\right) \tag{16}$$

where z_o is the roughness length that corresponds to the height at which the wind speed becomes zero when extrapolated downwards. For unstable and stable conditions, the wind profile is given by:

$$U = \frac{u_{*o}}{\kappa} \left[\ln\left(\frac{z}{z_o}\right) - \psi_m\right] \tag{17}$$

where ψ_m is the diabatic correction of the logarithmic wind profile and its form depends on the flux-profile relationship used for the integration of Eq. (15) (see Appendix D).

z_o has been related with the roughness elements and their geometry (Lettau 1969), but it should be estimated from the wind profile itself. In **Paper I** this is performed using wind speed observations at different heights and a least-squares curve fitting of Eq. (16). In **Paper II** and **III**, z_o is derived from friction velocity observations from a sonic anemometer and assuming the stress-wave dependence by Charnock (1955) (see Section 5.3). In **Paper IV** and **V**, wind speed and friction velocity observations at 10 m are used in combination with Eq. (17) to derive z_o. The resulting z_o values found in the different papers are in agreement with the range of values estimated over different types of terrain in Stull (1988).

In Figure 7 the typical behavior of the wind profile in the surface layer from Eq. (17) is illustrated. By plotting the wind profiles on a semi-log graph, the neutral wind profile appears as a straight line, whereas in unstable and stable conditions the wind profile deviates as convex and concave curves, respectively. When using the scaling U/u_{*o}, the wind profile is function of z/L and z/z_o only. The latter is fixed in Figure 7 to 0.1 m for the three stability conditions.

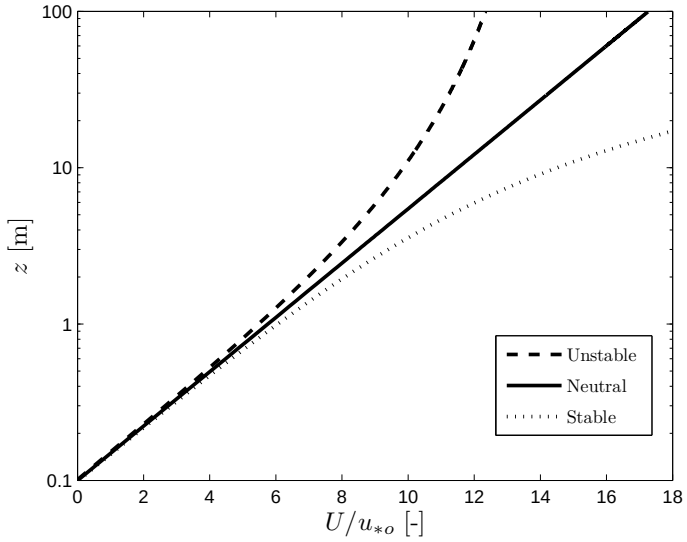

Figure 7. The typical behavior of the wind profile in the surface layer for the three basic stability conditions from Eq. (17) with $z_o = 0.1$ m.

Mixing-Length and K-Theory

The logarithmic wind profile, Eq. (16), can also be derived by analogy to molecular diffusion, due to the strong vertical gradients of wind and temperature in the surface layer. The surface-layer momentum flux–or surface Reynolds stress–can be expressed as:

$$-\overline{u'w'}_o = K_m \frac{\partial U}{\partial z} \tag{18}$$

where K_m is the turbulent exchange coefficient for momentum or eddy viscosity. In a similar form, the fluxes of heat and moisture can be related with the gradients of temperature and humidity by equivalent turbulent exchange coefficients–the so-called K-theory–(Stull 1988; Kaimal and Finnigan 1994). K_m can be represented within the surface layer as the product of a velocity and a length scale,

$$K_m = \kappa u_{*o} z \tag{19}$$

where κ is used as a constant of proportionality. Replacing K_m in Eq. (18) by (19) and using the definition of u_{*o} in Eq. (3) to replace $-\overline{u'w'}_o$ in Eq. (18), it is not difficult to obtain

$$\frac{\partial U}{\partial z} = \frac{u_{*o}}{\kappa z}, \tag{20}$$

which is equal to Eq. (15), but with $\phi_m = 1$, resulting in the logarithmic wind profile as shown above. K-theory is interesting for studying the atmospheric flow. It has been extended to cover the entire ABL (Yordanov et al. 1983), modified to account for different atmospheric conditions (Bhumralkar 1975), and used for the modeling of different exchange processes, e.g. dispersion models (Gryning et al. 1983; Smith 2008) and wind turbine wakes (Ainslie 1988).

Similar to K-theory and connected to it, the mixing-length theory can be used to study the behavior of the gradients of wind speed, temperature, and humidity in the ABL. Prandtl (1932) suggested a K_m coefficient proportional to the horizontal wind shear for atmospheric flow:

$$K_m = \ell^2 \frac{\partial U}{\partial z} \tag{21}$$

where ℓ represents the mixing length introduced by Prandtl (1925) from laboratory mea-

surements.[4] Replacing K_m in Eq. (18) by (21) and using the definition of u_{*o} in Eq. (3), the horizontal wind shear is given by

$$\frac{\partial U}{\partial z} = \frac{u_{*o}}{\ell}. \tag{22}$$

By comparing Eq. (20) to (22), it is directly inferred that the mixing-length scale in the neutral surface layer, $(\ell_{SL})_N$, is proportional to the height,

$$(\ell_{SL})_N = \kappa z \tag{23}$$

and that MOST can be used to extend it to account for diabatic conditions:

$$\ell_{SL} = (\ell_{SL})_N \, {\phi_m}^{-1} \tag{24}$$

where ℓ_{SL} is the surface-layer length scale. The simplicity of the mixing-length theory makes it useful for practical applications in particular for the modeling of the wind profile, as shown in **Paper III** for flow over the sea and in **Paper IV** and **V** for flow over flat terrain. It should be also mentioned that the mixing-length concept, as the K-theory, is theoretically preferable in neutral conditions, because it is derived from the assumption of linear gradients of wind and humidity, which are observed within small eddies (Stull 1988). Nevertheless, as shown in Blackadar (1962), Lettau (1962), Ohmstede and Appleby (1964), Estoque (1973), Hess (2004), and Gryning et al. (2007), it has been successfully used over the last 50 years for the modeling of the wind profile in the entire ABL and in different atmospheric stability conditions. Figure 8 illustrates the variation of ℓ and K_m resulting from flow simulations of the neutral-barotropic ABL based on the numerical solution by Estoque and Bhumralkar (1970) (see Appendix E). The simulation is performed assuming that the geostrophic wind is reached at 1000 m, thus, the surface layer extends to about 50–100 m where the K_m reaches a maximum. It is interesting to note that the ℓ profile used for the simulation is in agreement with $(\ell_{SL})_N$ for the first meters only.

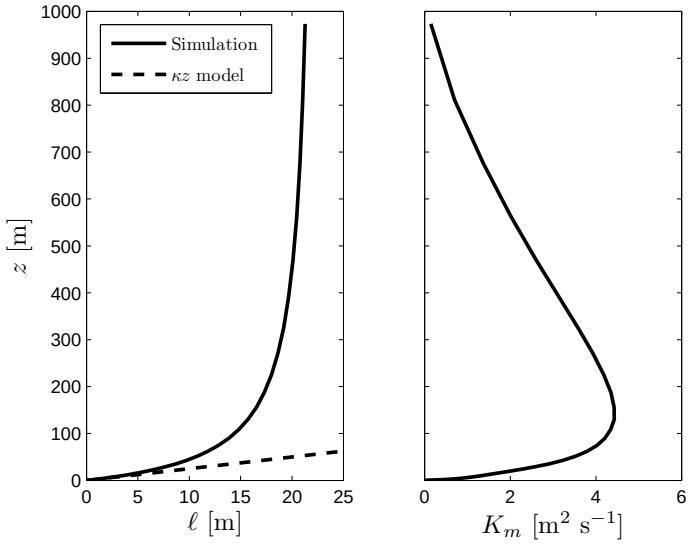

Figure 8. The typical behavior of the mixing length, ℓ, and the eddy viscosity, K_m, in the left and right panels, respectively, from the simulation of the neutral ABL based on Estoque and Bhumralkar (1970). The traditional surface-layer mixing length for neutral conditions, $(\ell_{SL})_N = \kappa z$, is also plotted in the left panel.

[4] In reality the suggestion was to relate the so-called *Austaush* coefficient, A_c, with the wind shear through the mixing length, but nowadays K_m is preferable and related to A_c as $K_m = A_c/\rho$.

3 Sites

The measurements and analysis were performed at two sites in Denmark: The Horns Rev offshore wind farm in the North Sea and the National Test Station of Wind Turbines at Høvsøre. The location of both sites is illustrated in Figure 9. Here they are described briefly. For more details about the instrumentation, specifications about the mast structures, coordinates of the locations, etc., see **Paper I**, **II**, **III**, **VI**, **VII**, and Sørensen (2005) for the Horns Rev site and **Paper IV**, **V**, **VII**, and Jørgensen et al. (2008) for the Høvsøre site.

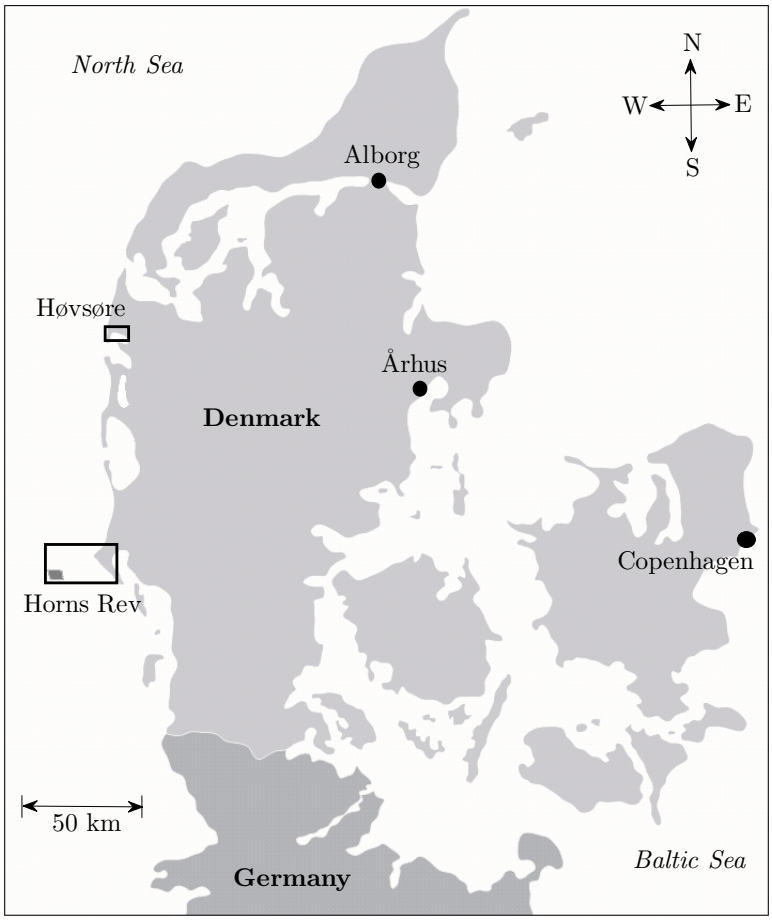

Figure 9. Location in Denmark of the National Test Station of Wind Turbines at Høvsøre and the Horns Rev wind farm in the North Sea. The dark colors indicate land surfaces and white water areas.

3.1 Horns Rev

Horns Rev is an offshore wind farm located in the North Sea near the West coast of Jutland, Denmark. There is a distance of approximately 12 km from the wind farm's transformer/platform to the nearest coast line (see Figure 10). Two meteorological masts, M2 and M7, were installed to the north-west and east of the wind farm, respectively, but dismantled recently. East and north-east of the wind farm a third meteorological mast, M6, and the wind farm's transformer/platform, respectively, are installed and in operation.

1. M2. The mast faces the predominant free upwind sector (as illustrated in the left plot

of Figure 12, which is based on measurements during the whole year 2006). The mast was instrumented with cup anemometers at different heights up to 62 m above mean sea level (AMSL), wind vanes, temperature sensors in the air and in the water, and other meteorological sensing instruments. For a shorter period, a sonic anemometer was installed at 50 m AMSL, which was used to measure turbulent fluxes examined in **Paper II** and **III**.

2. M6 and M7. Due to their location, they continuously observe the wake of the wind farm when the wind blows from the westerly sectors. Both masts were identical, with instrumentation similar to M2, but the wind speed measurements were available up to 70 m AMSL. No turbulent fluxes were measured on either of them.

3. Transformer/Platform. During the 12 MW project, a lidar and a sodar were installed for a six month period on the platform at 20 m AMSL. A first analysis from the lidar and sodar data is given in Peña et al. (2007) and in **Paper I** for lidar data only. Wind profile modeling and observation using the lidar measurements are treated in **Paper III**.

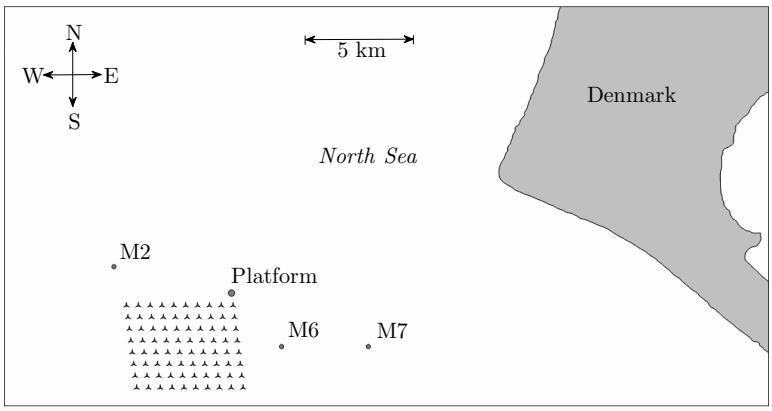

Figure 10. Horns Rev wind farm in the Danish North Sea. The position of the wind turbines is indicated with the symbol ⅄. The position of three meteorological masts, M2, M6, and M7, and the transformer/platform is also indicated.

3.2 Høvsøre

The National Test Station for Wind Turbines is located at Høvsøre, a rural area close to the West coast of Jutland, Denmark (see Figure 11). The terrain at Høvsøre is rather flat and the upwind flow, observed from the view of the meteorological mast, is influenced by the wakes of the wind turbines at the north and by the changes in roughness from the sea/land sectors at the west and south. At the north-easterly and easterly upwind sectors, the flow is fairly homogeneous, which allows the study of the wind profile for quasi-ideal conditions as performed in **Paper IV** and **V**. The influence of the village of Bøvlingbjerg on the wind profile observed at the meteorological mast is negligible as is shown in Section 5.1.

The meteorological mast is heavily instrumented with cup and sonic anemometers, wind vanes, temperature sensors and other meteorological sensors at different levels up to 100 m. A cup anemometer is also installed on a pole at 116 m, which is not affected by the wake of the mast on any upwind sector. At the light tower, cup and sonic anemometers are available at 60, 100, and 160 m. The latter height has been continuously used in combination with the mast measurements along this study.

As illustrated in Figure 12 (right plot) from measurements during the whole year 2006, the predominant winds at Høvsøre, as at Horns Rev, come from the westerly sectors,

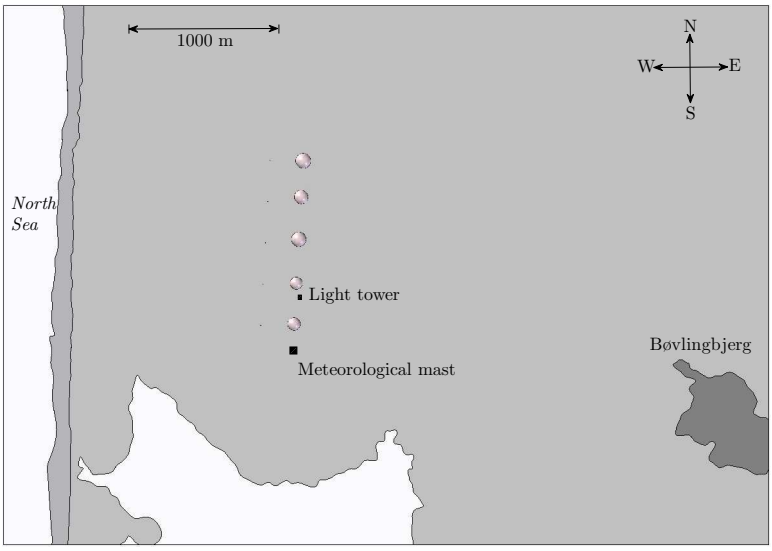

Figure 11. National Test Station for Wind Turbines at Høvsøre, Denmark. The location of the meteorological mast and light tower in rectangles, and five wind turbines in circles is indicated. The closest village, Bøvlingbjerg, is also shown.

thus, they are influenced by the sea/land interaction. Although the terrain within this upwind sector is also fairly flat, analysis of the wind profile requires the study of the internal boundary layer developed from the change of roughness, which is clearly observed from wind speed measurements at the mast as shown in Nissen (2008). On the other hand, winds from the homogeneous north-easterly sector are rather scarce, therefore, the analysis is limited to intermittent short periods.

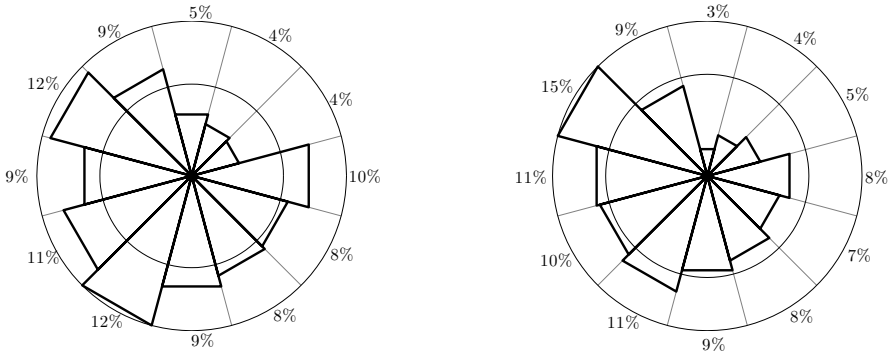

Figure 12. Wind roses observed at 60 m during the year 2006 for 30° wide upwind sectors at the meteorological mast M2 at Horns Rev (left plot) and at the meteorological mast at Høvsøre (right plot). The percentage of winds on each sector is also given.

4 Remote Sensing of the Atmosphere

4.1 Lidar

All lidars that measure the wind speed in the ABL basically operate under the same principle: A beam of light from a laser source illuminates a target and a small fraction of the backscatter radiation is received by a detector. When the target moves relative to the beam direction, the frequency of the light, w_o, experiences a Doppler shift, Δf. The radial velocity, also known as line-of-sight or along-beam velocity, v_r, of the target is related to the Doppler shift as:

$$v_r = \frac{\lambda_l \Delta f}{2} \tag{25}$$

where λ_l is the laser wavelength. Figure 13 illustrates the lidar principle where the laser is focused on a target (aerosols in the ABL) at a distance d.

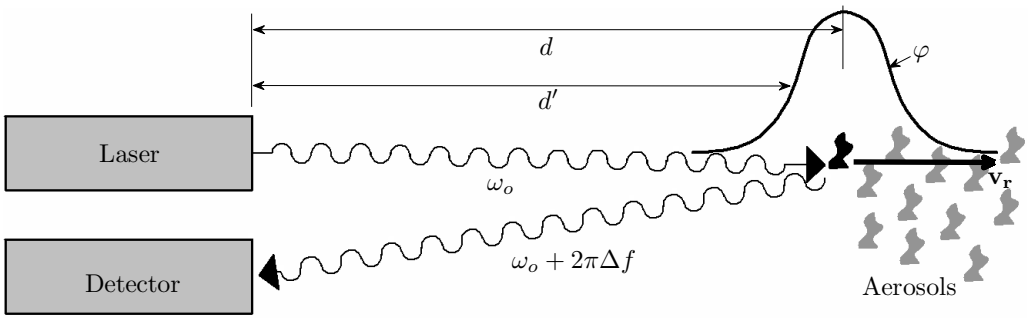

Figure 13. The principle of measurement of the wind lidars. Light is emitted at a frequency, w_o, from a source (laser), which illuminates a target at a distance d. The backscatter light experiences a Doppler shift, Δf, which is received by a detector. The contributions of the targets at distances d' are weighted in the beam direction by a function φ.

Due to the optics of the laser beam, scattering from any moving target at a distance d' of the illuminated region contributes to the returned signal. These contributions are commonly assumed to be weighted in the along-beam direction by a function φ with a peak in the beam's waist and falling symmetrically on either side.

Two wind lidars were used during this study:

1. QinetiQ ZephIR®. This is a continuous-wave (CW) coherent monostatic system operating at $\lambda_l = 1.55$ μm, which achieves operation at a given range by beam focusing. The along-beam weighting function, φ, is approximated by a Lorentzian distribution function,

$$\varphi = \frac{1}{\pi} \frac{l_z}{{l_z}^2 + (d' - d)^2} \tag{26}$$

   where l_z is the so-called Rayleigh length and corresponds to the ZephIR's half width at half maximum (HWHM) of the Lorentzian function. l_z is a function of the focused distance and the aperture diameter of the ZephIR's transmitter/receiver, d_t,

$$l_z = \frac{16\lambda_l}{\pi {d_t}^2} d^2 = 0.0012 d^2. \tag{27}$$

2. Leosphere WindCube®. This is a pulsed coherent monostatic system operating at $\lambda_l = 1.54$ μm, which uses the time of flight to discriminate between returns from different ranges or heights. The along-beam weighting function is approximated by

$$\varphi = \begin{cases} \frac{l_w - |d' - d|}{{l_w}^2} & \text{for } |d' - d| < l_w \\ 0 & \text{elsewhere} \end{cases} \tag{28}$$

where l_w is the WindCube's full width at half maximum (FWHM) length, which depends on the system's pulse length, $\tau = 200$ ns, and the speed of light, c_l,

$$l_w = \frac{c_l \tau}{2}. \tag{29}$$

The corresponding weighting functions for the ZephIR and WindCube systems, Eqs. (26) and (28), are illustrated in Figure 14 for three different focal distances. It is shown that for the ZephIR the FWHM length is equal to 2, 24, and 70 m at $d = 30$, 100, and 170 m, respectively, whereas for the WindCube the FWHM length is constant and equal to 30 m. Thus, the ZephIR is expected to have a much higher contribution of particles "out of focus" at distances above 100 m. The probe length of the WindCube is, on the other hand, much larger at shorter distances compared to the ZephIR.

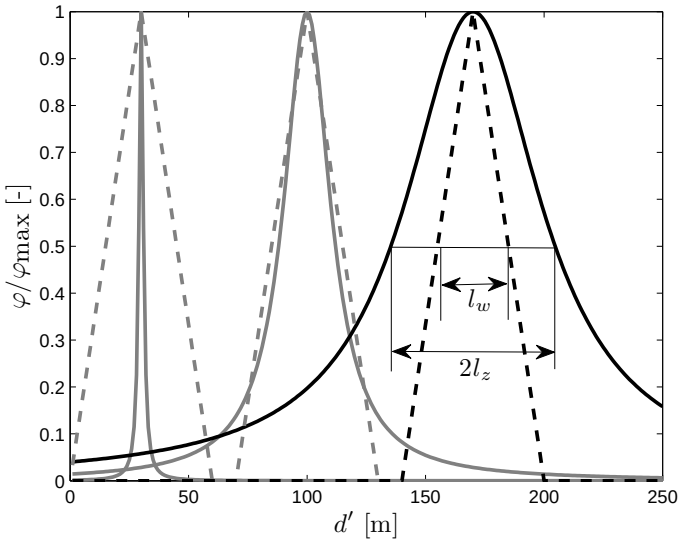

Figure 14. Normalized along-beam space-weighting function, φ/φ_{max}, for three focal distances, $d = 30$, 100, and 170 m, for the ZephIR (solid lines) and WindCube (dash lines) lidars. The "full width at half maximum" for both ZephIR and WindCube lidars, $2l_z$ and l_w, respectively, is also shown.

In the ZephIR system, the power of the backscattered light, mixed with the baseband light, is measured in the detector, sampled at 100 MHz, and converted to power spectra using a 256-point fast Fourier transform (FFT) (0–50 MHz). Thus, each spectrum has a bin width of 195 kHz that corresponds to radial velocity bins of ≈ 0.15 m s^{-1}. 4000 of these spectra are averaged to give an acceptable spectrum every 20 ms, which can be stored in the system. One of these average spectra is illustrated in Figure 15 for measurements performed at a focal distance of 43 m from the platform at Horns Rev. The contributions of the different radial velocities, or Doppler-shifted frequencies of the aerosols, within the measurement volume to the spectrum are shown.[5] The shape of the spectrum depends on the weighting function, the distribution of aerosols within the measurement volume, the turbulence, and the wind shear. Figure 15 shows the radial velocity corresponding to the peak and the centroid of the spectrum. The centroid radial velocity is commonly preferred for wind speed estimation, because it represents the weighted average of contributions of radial velocity along the laser beam.

In the WindCube system, a stream of pulses (5000–10000) is sent and the detector records the backscattered light in a number of range gates for fixed time delays. For each range gate, the time series of each pulse is Fourier transformed to a block-average

[5]When the Doppler-shifted frequencies are converted to radial velocities, the spectrum becomes a distribution of radial velocities, but for simplicity such distribution is also called spectrum.

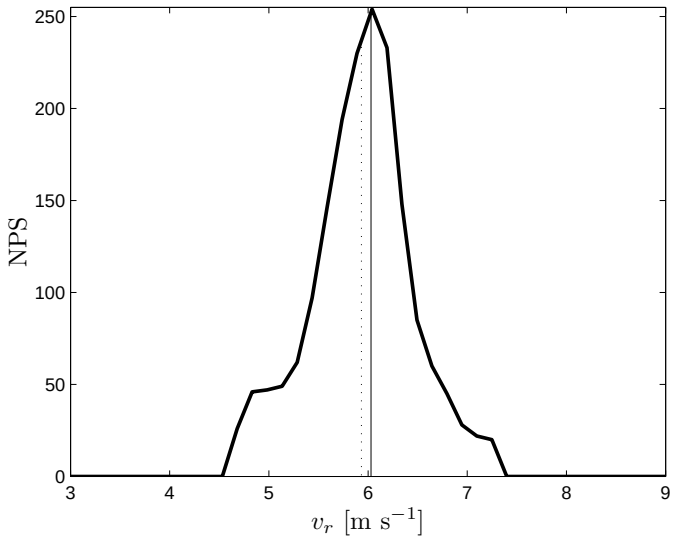

Figure 15. Normalized average power spectrum (NPS) of the Doppler shifted frequencies, converted to radial velocities using Eq. (25), for a focal distance of 43 m from ZephIR observations at Horns Rev. The two vertical lines represent the spectral peak (solid line) and the spectral centroid (dotted line).

power spectrum. Leosphere developed a mathematical model to fit each average power spectrum, from which the centroid Doppler-shifted frequency is estimated. The WindCube, in contrast with the ZephIR, does not store the power spectra, therefore, only the weighted radial velocities can be extracted.

Conical scanning

In order to measure the three wind velocity components in the ABL, both ZephIR and WindCube are arranged to scan the atmosphere conically from the ground. For both lidars, the laser beam is tilted at an angle ϕ from the zenith, thus, they are able to measure the radial velocity vector, $\mathbf{v_r}$, as a function of the wind velocity vector, $\mathbf{u}$. The components of $\mathbf{u}$, i.e. u, v, and w, can be derived by measuring at different azimuth angles, θ. The conical scanning configuration of the lidars is illustrated in Figure 16.

As illustrated in Figure 16, the WindCube measures the radial velocity at four points separated by 90°, whereas the ZephIR measures at 50 points around the circle formed by the conical scanning. The radial velocity is then a function of the wind speed components and the geometrical angles:

$$v_r = v\cos\theta\sin\phi + u\sin\theta\sin\phi + w\cos\phi, \tag{30}$$

$$= U\cos(\theta-\theta_d)\sin\phi + w\cos\phi \tag{31}$$

where θ_d is the wind direction. A least-squares fitting function is commonly used to determine U, w, and θ_d from a set of radial velocities measured at different azimuth angles. Figure 17 illustrates radial velocities measured during a simultaneous 10-min period for both types of lidars at Høvsøre, as well as the fitted curves using Eq. (31).

Figure 17 shows that the range of observations of v_r from the WindCube is larger compared to the ZephIR's range for the same azimuth angle. This is mainly due to attenuation of the radial velocity from the sampling volume. This is explained in detail in **Paper VII** where it is assumed that the radial velocity can be written as the weighted average along the lidar beam,

$$\widetilde{v_r} = \int_{-\infty}^{\infty} \varphi\mathbf{n}\cdot\mathbf{u}(s_d\mathbf{n}+\mathbf{x})ds_d = \int_{-\infty}^{\infty} \varphi v_r ds_d \tag{32}$$

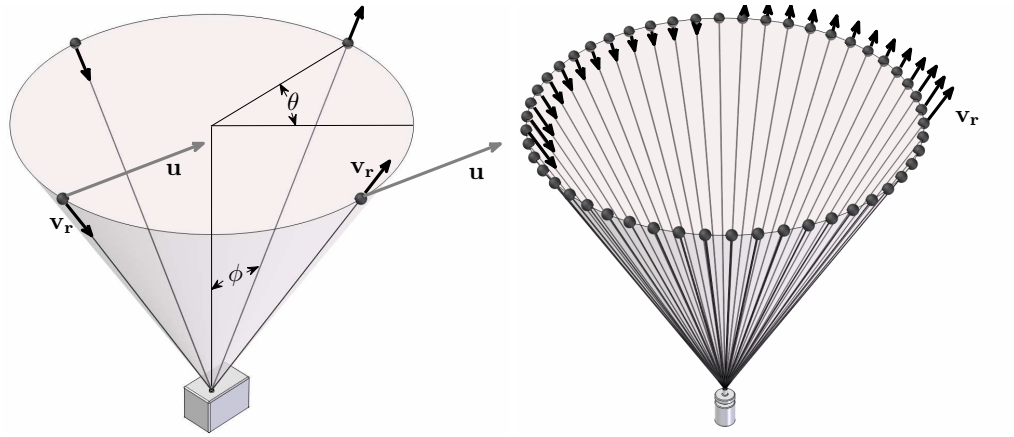

Figure 16. Scanning configuration for both WindCube (left frame) and ZephIR (right frame) lidars. The radial and wind velocity vectors, and the azimuth and zenith angles, $\mathbf{v_r}$, $\mathbf{u}$, θ, and ϕ, respectively, are also illustrated.

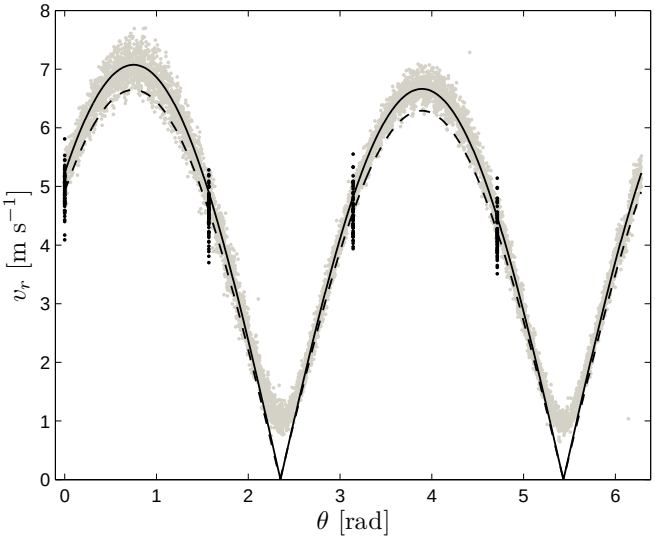

Figure 17. Radial velocity, v_r, measured at different azimuth angles, θ, for a 10-min period from lidar scanning at 116 m height at Høvsøre. The observations from the ZephIR are shown in light grey dots and from the WindCube in black dots. The fitted curves for v_r from Eq. (31) are also shown for the ZephIR (solid line) and WindCube (dashed line).

where $\mathbf{n}$ is a unit vector in the direction of the laser beam, $\mathbf{u}(\mathbf{x})$ is the wind velocity field, and $s_d = d' - d$. Using spectral definitions and the normalization of the Fourier transforms as shown in Mann (1994), it can be demonstrated that the variance of v_r in Eq. (32) is given as

$$\sigma_{\widetilde{v_r}}{}^2 = \int n_i n_j \mathbf{\Phi}_{ij} |C(\mathbf{k}\cdot\mathbf{n})|^2 d\mathbf{k} \tag{33}$$

where $\mathbf{\Phi}_{ij}$ is the spectral tensor (Panofsky and Dutton 1984), $\mathbf{k}$ is the wavenumber vector, and $C(\mathbf{k}\cdot\mathbf{n})$ is the Fourier transform of the weighting function φ, Eqs. (26) and (28). The latter is given as

$$C(\mathbf{k}\cdot\mathbf{n}) = \begin{cases} \exp(-|\mathbf{k}\cdot\mathbf{n}|l_z) & \text{for the ZephIR and} \\ [\sin(\mathbf{k}l_w/2)/(\mathbf{k}l_w/2)]^2 & \text{for the WindCube,} \end{cases} \tag{34}$$

i.e. the weighting function can be treated as a turbulence filter.

Figure 18 illustrates the 10-min time series of the horizontal wind speed fluctuation, U', for the same lidar data as in Figure 17 together with the simultaneous cup anemometer observations at 116 m. A major difference in the standard deviation estimated from the ZephIR compared to the cup anemometer and WindCube measurements is shown. Although both the ZephIR and WindCube observations are taken at a similar frequency, ≈ 0.1 Hz, rather lower than the cup anemometer frequency, 10 Hz, the turbulence observed by the ZephIR is more attenuated than that observed by the WindCube, which is mainly due to the large weighting function in the ZephIR's measurement volume. Figure 18 also shows that it is the large measurement volume and not the frequency rate at which the measurements are performed, which is the major contributor to the filtering of turbulence.

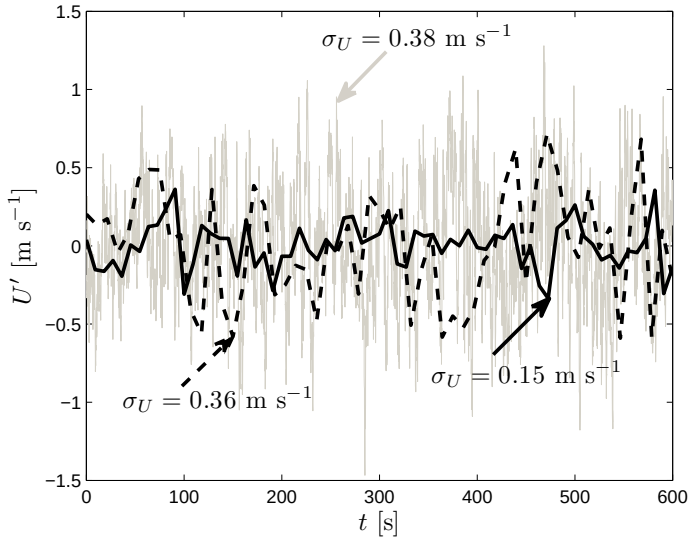

Figure 18. 10-min time series of horizontal wind speed fluctuations, U', from simultaneous ZephIR (solid black line), WindCube (dashed black line), and cup anemometer (solid gray line) measurements at 116 m at Høvsøre. The standard deviation of the time series is also given for each instrument.

As shown in **Paper I** and **VI**, direct comparisons of U show good agreement and high correlations[6] between the 10-min ZephIR lidar and mast cup anemometers marine observations within the free upwind sectors at Horns Rev, although the lidar was placed on the platform, which is $\approx$ 3–6 km away from the masts of the wind farm. Similar agreement and correlations for 10-min observation of U are found within the flat and homogeneous upwind sector at Høvsøre for two different WindCube lidar units, the first placed during winter months in 2007–2008 (**Paper IV**) and the second during summer months in 2008 (**Paper V**).

In **Paper I**, comparisons of the so-called turbulence intensity, $I_U = \sigma_U/U$, are shown for 10-min measurements performed with cup anemometers at the different masts at Horns Rev and the lidar on the platform.[7] The measurements are well correlated, but I_U from the lidar is attenuated compared to the cup anemometer observations, because of the filtering on the variance and, thus, on σ_U. This is also shown in Figure 19, but on the variation of I_U with wind speed for the cup anemometer and lidar observations

[6]The agreement and correlation is referred to the parameters found from a linear regression between the observations of the two instruments, namely the slope and the correlation coefficient.

[7]I_U is an important parameter for the estimation of the dynamical loading and the wind farm power production, although for meteorological studies it is less relevant, because $\sigma_{u,v,w}$ are scaled with u_* rather than U.

for a common mast-platform free upwind sector. Although I_U is attenuated from the lidar observations, it agrees well with the behavior observed with the cup anemometers, i.e. it follows a convex curvature; for the first range of wind speeds, I_U decreases due to stability effects, whereas it increases at about 10 m s^{-1} due to the increase of sea surface roughness with wind speed. I_U also decreases with height, due to the increase of wind speed at higher levels.

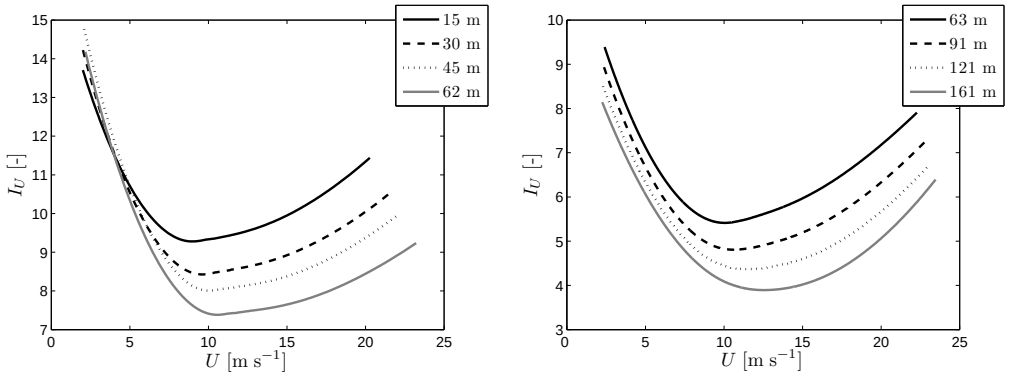

Figure 19. Turbulence intensity, I_U, variation with wind speed, U, for different heights on the common M2-platform free upwind sector, $270° - 360° \wedge 0° - 10°$, at Horns Rev. The observations of the cup anemometers at M2 are shown in the left panel and the lidar observations in the right panel. The lines result from a lest-squares fit of the scatter data.

Eq. (33) also shows that in order to estimate theoretically the filtering effect of the lidar's measurement volume, three-dimensional spatial statistics, i.e. the spectral tensor, are needed. In **Paper VII**, the spectral model in Mann (1994) is used to numerically compute this filtering effect on the radial velocity variances of the upstream and downstream directions resulting from the conical scanning configuration of the lidars, ${\sigma_{\rm up}}^2$ and ${\sigma_{\rm down}}^2$, respectively. These are related to the orthogonal velocity variances, because σ_{v_r} is a function of θ as shown in Eberhard et al. (1989):

$$\begin{aligned} {\sigma_{v_r}}^2 &= {\sigma_u}^2 \sin^2\phi\cos^2\theta + {\sigma_v}^2 \sin^2\phi\sin^2\theta + {\sigma_w}^2\cos^2\phi + \\ &\quad 2\overline{u'v'}\sin^2\phi\cos\theta\sin\theta + 2\overline{u'w'}\cos\phi\sin\phi\cos\theta + 2\overline{v'w'}\cos\phi\sin\phi\sin\theta. \quad (35) \end{aligned}$$

The filtering effect on the radial velocity is important, because this is the velocity observed directly by the lidars, which can be related to other meteorological parameters, e.g. to the momentum flux, $\overline{u'w'}$. Thus, evaluating Eq. (35) for the upstream and downstream directions, i.e. σ_{v_r} at $\theta = 180°$ and $\theta = 0°$, respectively, and taking their difference, it can be demonstrated that the momentum flux is given by:

$$\overline{u'w'} = \frac{{\sigma_{\rm down}}^2 - {\sigma_{\rm up}}^2}{4\sin\phi\cos\phi}. \quad (36)$$

Thus, the filtering on $\overline{u'w'}$ can be estimated and compared with eddy-correlation measurements of momentum flux from sonic anemometers. This is shown in **Paper VII** from measurements performed at Høvsøre within a wide sea-influenced wind sector at three lidar/sonic anemometer overlapping heights (40, 80, and 100 m) using the ZephIR lidar and at five overlapping heights (40, 60, 80, 100, and 160 m) using the WindCube lidar. The comparison shows a high degree of correlation and the effect of the filtering, not only for the momentum flux, but also for the downstream and upstream radial velocity variances (Figure 20 illustrates the measurements of the momentum flux for the 40 m height at Høvsøre using a ZephIR lidar and a sonic anemometer). The filtering effect is well-predicted when computing Eq. (33) using the Fourier transforms of the weighting functions of the lidars, Eq. (34), and the spectral model of Mann (1994). Due to the large measurement volume of the lidar, it is also shown that the lidar momentum flux

correlates with the sonic anemometer measurements better in unstable than in stable or neutral conditions where the size of the eddies is normally small. Thus, the lidar might be measuring within the same turbulent eddy under convective conditions.

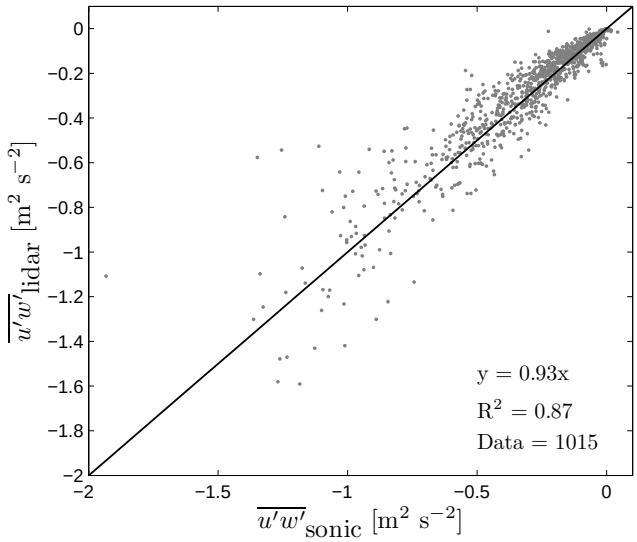

Figure 20. Comparison of ZephIR lidar and sonic anemometer measurements of momentum flux at 40 m at Høvsøre.

Also in **Paper VII**, lidar measurements of momentum flux performed with the ZephIR at 63 m AMSL within the free-upwind sector at Horns Rev are compared to the momentum flux derived from the wind speed measurements of the cup anemometers on M2, i.e. by combining the traditional surface-layer wind profile, Eq. (17), with the model of Charnock (1955) for the sea roughness length (see Section 5.3) for near-neutral stability conditions. The result of the comparison shows nearly the same agreement and correlation as found at Høvsøre at 40 m, a height comparable to the observations at Horns Rev, when the size of the platform (where the lidar was installed) is taken into account.

Errors and weaknesses in lidar measurements

Measurement volume The major implications, found thus far, of a larger measurement volume in the lidar observations, compared to, e.g. that of a cup anemometer, which has a spatial resolution close to 2 m, are related to:

1. Range. The increasing measurement volume in the ZephIR lidar limits the measurement range to about 150 m. On the other hand, the backscatter observed for heights below 40–60 m in the WindCube can be erroneously contaminated with backscatter leaving the lidar's lens, due to the relatively long length of the pulse ($\approx$ 30 m).

2. Clouds. Enhanced backscatter from low clouds can contribute to a strong reduction in the accuracy of the ZephIR measurements from the prolonged tails of the weighting function. The ZephIR unit installed on the Horns Rev platform had an algorithm to correct cloud-affected measurements. The system used to measure at 300 m, an observation assumed to hit the low clouds and used to correct the spectra observed at lower heights. The algorithm, nevertheless, affected all types of measurements, including non-cloud affected. Therefore, a strategy was implemented during the Horns Rev experiment, which is described in **Paper I**, to identify clouds by comparing the ratio between the lower and the 300 m backscatter measurements. A new cloud algorithm was developed by QinetiQ based on this strategy. The WindCube collects

backscatter, in contrast with the ZephIR, within finite range gates, thus, only clouds within the measurement range affect the observations.

3. Wind shear. The measured radial velocity by the lidar results from the contribution of different radial velocities within the measurement volume. Such contribution depends on the wind shear that in most of the cases is not linear and induce an error in the measurement. Typical wind profiles, illustrated in Figure 21 (left), can be used to estimate the deficit of wind speed, $U_{def} = (U_l - U)/U_l$ where U_l is the lidar wind speed observation, when the lidar performs measurements at a height where different wind profiles show the same wind speed. Due to the curvature of the profiles, the weighted radial velocity, Eq. (32), becomes a function of a non-linear radial velocity profile and the lidar weighting function. Figure 21 (right) shows the wind speed deficit estimated with a ZephIR lidar by simulating wind profiles with the same wind speed at 20 up to 120 m. The results in Figure 21 (right) show that the error by measuring a linear wind profile (solid line), typical from very stable conditions, is considerably lower compared to the error by measuring a profile typical from LLJ conditions (dashed line). The error increases with height, because of the increasing measurement volume in the ZephIR lidar and it will also depend on wind speed. Lindelöw et al. (2008) studied the wind shear effects on WindCube wind speed observations at Høvsøre and proposed a regression based on two parameters, taking into account wind speed and wind shear, to calibrate such wind lidars.

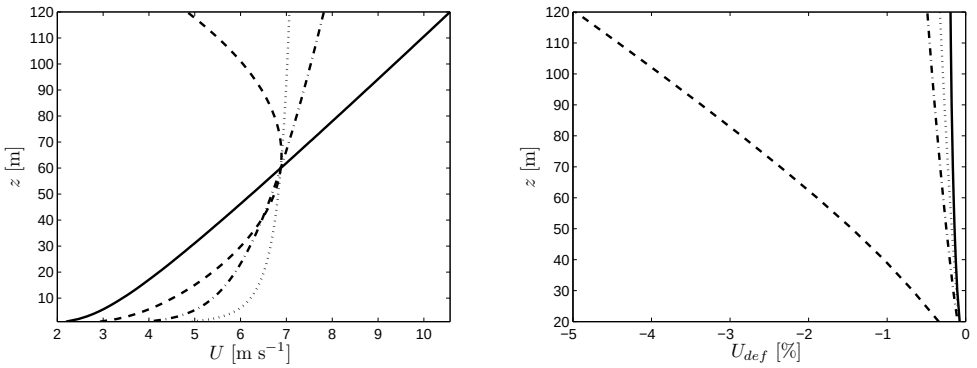

Figure 21. Left panel: Typical wind profiles showing the same wind speed at the lidar observation height. Right panel: Wind speed deficit, U_{def}, estimated with a ZephIR lidar by simulating the wind profiles in the left panel with same wind speed at the lidar observation height.

4. Aerosol profile. Inherent in the lidar measurements is the assumption of a vertical constant aerosol profile, i.e. a constant concentration of aerosols along the measurement volume. This assumption can be far from reality as observed in particular in stable conditions (see Section 4.2 and **Paper V**). The errors due to non-uniformity of the aerosol profile are larger for the ZephIR, but they can be reduced using a similar strategy as explained previously for cloud-related errors and in **Paper I**.

5. Flow homogeneity. Probably the major contributor to errors from lidar wind speed observations is the assumption of wind homogeneity within the measurement volume. For both sites, Horns Rev and Høvsøre, at least for most of the upwind sectors analyzed, flow homogeneity can be fairly assumed, due to the terrain characteristics. Nevertheless, as shown in **Paper VII**, when the observations at Høvsøre are classified in stability conditions, the correlation between observations of the momentum flux from the lidar compared to sonic anemometer is significantly reduced for stable conditions. This is because the size of the turbulent eddies is smaller compared to

unstable conditions, in which the lidar measurements might be performed within the same eddy.

Complex terrain The two sites analyzed in this study, Høvsøre and Horns Rev, correspond to rather flat and homogeneous terrain. However, the conical scanning configuration of the lidars can lead to large wind speed deficits when the instruments are installed over complex terrain. In Appendix F, a simple analysis is done by simulating a lidar over a cylindrical hill. An interesting result from the analysis, illustrated in Figure 36, is that the wind speed deficit of the lidar measurements has a weak dependence on the conical or zenith angle. In order to avoid such effects over complex terrain, a 3D lidar solution, i.e. three staring lidars, can be employed (Mann et al. 2008).

Other Errors in lidar measurements can be related to inaccuracy of the hardware of the instrument. Lindelöw-Marsden (2007) found that an average error of 5 m in the sensing height lead to a bias of ≈ 0.2 m s^{-1}, depending on the wind shear. For a ZephIR lidar this error might appear when controlling the optical settings and for a WindCube lidar when looking at the range gates, because the start and end of the pulse can be difficult to define. An error in the zenith or cone angle, ϕ, introduces an error in the estimation of the wind velocity, Eq. (31), and an error in the sensing range. A cone angle difference of 0.5°, leads to an error of 0.125 m s^{-1} at 10 m s^{-1} and a wind shear of 0.05 m s^{-1}/m (Lindelöw-Marsden 2007). Other sources of hardware errors, such as tilted mounting and relative intensity noise that might introduce a bias at low wind speeds in the ZephIR lidar observations, are well documented in Lindelöw-Marsden (2007).

Rain has an influence on the estimation of the vertical velocity of the lidar, due to the downward motion of the raindrops. U might be also slightly overestimated, but according to Lindelöw-Marsden (2007) a comparison between lidar and cup anemometer observations at Høvsøre, during raining periods, showed small biases ($\pm$0.01–0.04 m s^{-1}). Turbulence, however, did show a large bias, due probably to its high dependence on v_r, highly influenced by the vertical velocity. Wind veer, i.e. changes in wind direction with height, can also induce errors in the lidar measurements, but this can be estimated in the same form as the wind shear errors commented above.

4.2 Ceilometer

A ceilometer, a traditional application of the lidar technique commonly used to measure cloud heights, also operates based on the transmission of light through the atmosphere. It sends a short pulse of light that is backscattered by all kind of particles and aerosols distributed along the ABL. The ceilometer measures the time delay, t_d, of the light returned back to the instrument's receiver, and using the relation

$$z = \frac{c_l t_d}{2}, \tag{37}$$

the height of the aerosols in the atmosphere can be determined. The instrument also measures the strength of the returned signal, namely the instantaneous power P, which is given by the so-called lidar equation:

$$\mathrm{P} = E_o \frac{c_l}{2} \frac{A_t}{z^2} \beta \exp\left(-2 \int_0^z \Gamma dz\right) \tag{38}$$

where E_o is the effective pulse energy, i.e. taking into account all the optical attenuation, A_t is the receiver aperture area, β is the volume backscatter coefficient at a distance z, the term involving the exponential is the two-way atmospheric transmittance that accounts for the attenuation of transmitted and backscattered power by extinction at the heights between the instrument and the height of observation and equals one in a clear atmosphere, and Γ is the extinction coefficient. β, which is actually the reported measurement from the ceilometer, represents the amount of light reflected back to the

ceilometer from a determined height, thus, the denser the layer of aerosols, the stronger the returned signal. It is proportional to Γ, which is related to the visibility, defined according to contrast thresholds.

Ceilometers are originally designed to measure the height and width of the clouds, because these exhibit high reflectivity, scattering light efficiently. Thus, β strongly increases by approx. 100–1000 times its value in a clear sky situation, when the light is returned from a height where a cloud is located. However, some ceilometers are fairly sensitive and under some atmospheric conditions can retrieve the profile of backscatter coefficient, i.e. they can give information about the amount of aerosols along the ABL.

During this study, the ceilometer CL31 from Vaisala has been used to analyze the aerosol profile that is related with the structure of the ABL. The CL31 transmits light pulses at 5.57 kHz with a wavelength of 0.91 μm and a 50% width of 100 ns. It digitally samples the signal every 33 or 67 ms from 0 to 50 μs, providing a spatial resolution of 5–10 m up to a distance of 7700 m. The laser power is significantly low, therefore, the ambient light noise exceeds the backscatter signal. To overcome this problem, the returned signals of a large number of pulses are summed and the noise is partially cancelled. With a resolution of 15 s, which is programable as the spatial resolution, each backscatter profile results from the sum of 65 536 pulses.

In Figure 4 the evolution of aerosols for two consecutive clear-sky summer days is illustrated. The spatial resolution used for the measurements is 20 m, and the backscatter profiles are averaged every 30 min from the reported 2 s observations. Similar plots are illustrated in Figure 22 for ceilometer observations performed at Høvsøre on 24 September 2008. The spatial resolution is also 20 m and the profiles are averaged every 10 min. Although it is a rather convective day, it is observed in Figure 22 (left) that the presence of clouds at 500–600 m between 1000 and 1200 LST with high β values, $(\approx 6000\text{–}7000)\times 10^{-5}$ m^{-1} srad^{-1}, slightly complicates the study of the ABL structure. Under the presence of fog or clouds, a threshold can be applied on an interval of β values that are normally measured in clear-sky conditions, as illustrated in Figure 22 (right), in order to observe the less dense distributions of aerosols in the atmosphere.

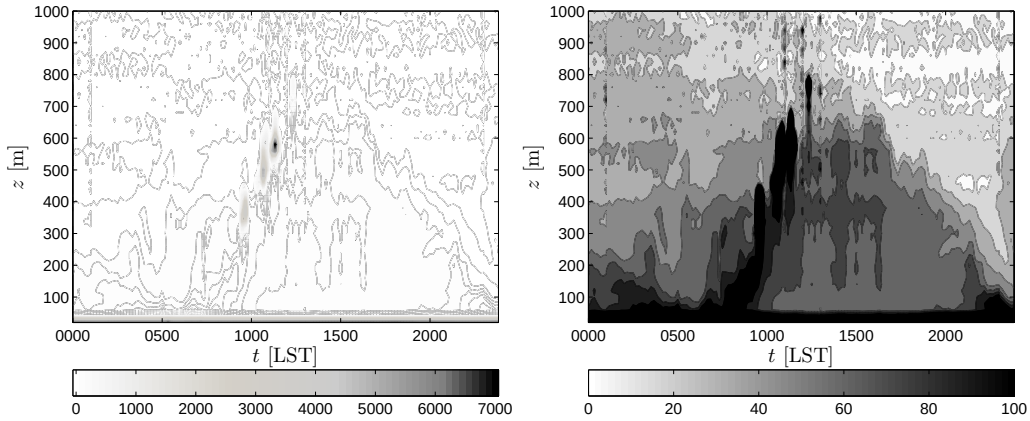

Figure 22. Aerosol backscatter coefficient in the atmosphere during a fall day (24 September 2008) from ceilometer observations at Høvsøre, Denmark. The 10-min raw measurements are shown in the left panel, whereas a threshold on the colormap is used to analyzed a smaller range of β values in the right panel.

In Section 2, the height of the boundary layer is defined as the portion of the atmosphere influenced by the surface. The pollutants in the atmosphere, such as aerosols, gases, and particles, can be emitted from the surface and are diluted through the ABL. Therefore, the profile of aerosol backscatter might give information about the size of z_i. Intuitively from Figure 22 (left), z_i can be estimated from the cloud-base height, i.e. $z_i \approx 550$

m at 1100 LST, and it seems to fluctuate between 500 and 700 m in the afternoon, by observing the darker contour lines in Figure 22 (right). Many attempts have been done in order to determine z_i from ceilometer observations of the aerosol backscatter. In Emeis et al. 2004, estimates of z_i were compared between SODAR, RASS, and ceilometer measurements and the ceilometer showed its usefulness and complementarity to the RASS and SODAR techniques, which are traditionally used for z_i evaluation. In Eresmaa et al. 2006, a direct comparison between ceilometer and radio sounding measurements showed good agreement for convective situations, whereas for stable conditions the comparison did not agree well, due probably to the low backscatter coefficient in the low layers of the atmosphere.

Some of the differences between such comparisons might be due to a possible time delay between the dispersion of pollutants and the thermal distribution of the ABL (Emeis and Schäfer 2006), the presence of clouds or fog, the high noise of the ceilometer measurements, the lack of knowledge of the aerosol profile, and the technique applied for the evaluation of z_i. Concerning the last two, Eresmaa et al. 2006 already showed some limitations under stable conditions and in **Paper V** the difficulties to determine the stable z_i, due to the shape of the aerosol profile are shown. In Emeis et al. (2008) the minimum gradient technique is used to derive z_i from the aerosol profile, but from the continuous measurements of ceilometer backscatter profiles at Høvsøre in the last two years, it has been observed that this technique results in different estimations of z_i along the aerosol profile. It therefore requires some postprocessing tools in order to average the profiles in time and space to avoid the noise of the measurements.

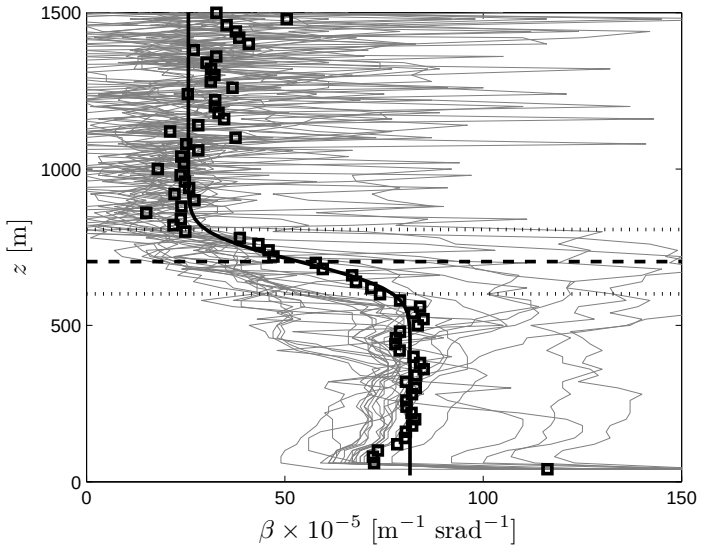

Figure 23. Ceilometer observations of the backscatter coefficient, β, for 23 unstable conditions, $-100 \leq L \leq -10$, from July–October 2008 at Høvsøre, Denmark. The 10-min profiles are shown in gray color and the mean of the observations in rectangles. The idealized profile fit, Eq. (39), is shown in a black solid line, the fitted z_i in a dashed line, and the thickness of the entrainment layer is between the dotted lines.

In **Paper V**, the technique by Steyn et al. (1999) is successfully used to determine z_i for unstable and near-neutral conditions. For stable conditions, turbulence parameterizations are used instead, due to the shape of the profile. Steyn et al. (1999) fitted an idealized aerosol profile to the measurements. This has the form,

$$\beta = \frac{B_u + B_o}{2} - \frac{B_u - B_o}{2} \mathrm{erf}\left(\frac{z - z_i}{ez}\right) \tag{39}$$

where B_o is the mean backscatter coefficient above the entrainment layer of thickness

ez and B_u is the mean backscatter coefficient below the entrainment zone. Figure 23 illustrates this technique by fitting Eq. (39) to a mean aerosol profile measured in unstable conditions. It is observed that the mean aerosol profile has a similar form to that of the idealized profile, whereas the individual 10-min profiles are too noisy. **Paper V** shows, how the stable profiles do not follow the idealized profile and demonstrates the difficulties in determining the parameters B_o and B_u.

Another issue observed from the ceilometer measurements, which makes the evaluation of z_i difficult, especially for stable conditions where this can be rather shallow, is that for the first 80–120 m, the returned signal seems to be contaminated by optical noise and the slight misalignment of the light source and the detector, resulting in large β values. Therefore, it is not recommended to evaluate z_i from ceilometer observations for very stable conditions where z_i can be found at around 100 m, as shown in **Paper V**.

5 Modeling of the wind profile

5.1 The Wind Profile over Land

Over flat land and homogeneous terrain, and assuming zero displacement height, the observations of the surface-layer wind profile agree with Eq. (17) illustrated in Figure 7, as shown, e.g. in Holtslag (1984), Gryning et al. (2007), and **Paper V** for several stability conditions, and in **Paper IV** for near-neutral conditions. Although the terrain can be certainly much more complex, the wind profile over homogeneous and flat terrain constitutes the basis for wind profile analysis. Furthermore, the research on this topic does not seem to end in the near future.

The wind profile can be studied in numerous ways. The observations are normally based on 10- or 30-min periods, where statistical moments like means and variances are derived. Therefore, the wind profile can be analyzed, e.g. dividing the mean wind speed into different ranges. However, it is shown in Figure 7 that in stable or unstable conditions, the wind profile deviates from logarithmic. Thus, by "ranging" mean wind speeds only, different atmospheric conditions with similar wind speeds might be mixed together, resulting in an average wind profile[8] which can be close, e.g. to the logarithmic wind profile, although the conditions might be far from neutral.

Due to its dependence on z/L, the wind profile can be easily analyzed under quasi-ideal conditions,[9] by computing L at a height close to the ground for each 10/30-min mean wind profile and, then, the mean wind profiles lying within a specific interval of stabilities are averaged together. In Table 1 a definition of different stability intervals is shown, which have been successfully used for land (Gryning et al. 2007 and **Paper V**) and for offshore observations (**Paper II** and **III**).

Table 1. Stability classes according to Obukhov length intervals.

Stability class	Interval of Obukhov length L [m]
Very stable (vs)	$10 \leqslant L \leqslant 50$
Stable (s)	$50 \leqslant L \leqslant 200$
Near neutral/stable (ns)	$200 \leqslant L \leqslant 500$
Neutral (n)	$\lvert L\rvert \geqslant 500$
Near neutral/unstable (nu)	$-500 \leqslant L \leqslant -200$
Unstable (u)	$-200 \leqslant L \leqslant -100$
Very unstable (vu)	$-100 \leqslant L \leqslant -50$

Thus, the average wind profile is a function of z/L and of an average z_o value computed within each stability interval. The average of the observations determines the value for z_o in each stability class from the location of the profile relative to the graph where the scaling U/u_{*o} is used. This is illustrated in Figure 24 for wind speed observations at Høvsøre, Denmark. Here, the observations are selected within the flat and homogeneous upwind sector, 30–125°, observed at the 116 m meteorological mast and only profiles with mean wind speeds above 2 m s^{-1} at all heights are used for the analysis. The data corresponds to the period between September 2004 and January 2008. The average surface parameters observed at 10 m in each stability class are given in Table 2. In Figure 24 the predictions of the wind profile for each stability class using Eq. (17) are also shown in combination with the values in Table 2 and applying the values $b_1 = 4.7$, $p_1 = -1/3$, and $a_1 = 12$ for the ψ_m function as done in Gryning et al. (2007).

[8] Here average corresponds to the ensemble of the 10- or 30-min means.

[9] Very calm or strong winds should be also excluded, due to limitations of MOST.

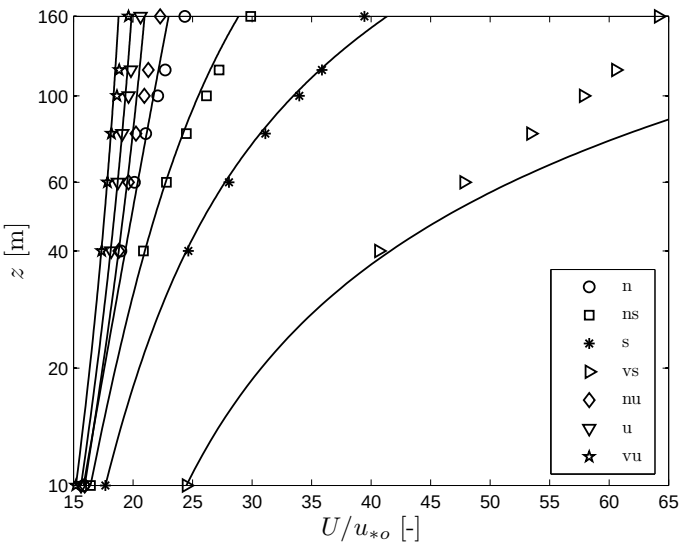

Figure 24. The Høvsøre wind profile for different stability classes. The markers indicate the observations and the solid lines the predictions using Eq. (17) in combination with the surface parameters in Table 2. The explanation of the legend is given in Table 1.

Table 2. Average surface parameters observed at 10 m at Høvsøre, Denmark, in each stability class.

Stability class	No. of profiles	z_o [m]	u_{*o} [m s^{-1}]	U_{10} [m s^{-1}]	L [m]	$\overline{w'\Theta_v{}'}_o$ [K m s^{-1}]
vs	5004	0.0035	0.14	3.31	21	−0.0088
s	4769	0.0133	0.25	4.42	90	−0.0143
ns	2300	0.0162	0.34	5.61	298	−0.0118
n	4614	0.0164	0.47	7.55	8117	−0.0008
nu	1492	0.0152	0.42	6.64	−295	0.0250
u	1799	0.0154	0.40	6.18	−137	0.0430
vu	1492	0.0157	0.33	5.06	−71	0.0474

5.2 Summary of the Wind Profile over Land

Based on the results of Figure 24 and Table 2, some interesting features can be pointed out for the wind profile over land:

- Up to about 100 m, the wind speed observations behave as expected in the surface layer, i.e. they follow a convex or concave shape in agreement with the stability condition or a straight line in the case of neutral conditions, as shown in **Paper II** and **III** for flow over the sea and in **Paper IV**, **V**, and Gryning et al. (2007) for flow over land.
- The predicted wind profiles using Eq. (17) agree well with the observations within the first 100 m, except for the very stable wind profile, which starts to deviate at about 40–60 m, as shown in **Paper II**, **III**, **IV**, **V** and Gryning et al. (2007).
- All predicted profiles are matched with the observation at 10 m, because z_o is determined from Eq. (17) using the observations at this height only.
- The computed values for z_o do not vary strongly for the stability classes where the wind speed observations are well predicted by Eq. (17) and are in agreement with the

findings in Gryning et al. (2007) who analyzed the measurements for a shorter period (March 2004–November 2005). As it is expected to observe more unstable conditions during summer and more stable conditions during winter time, the relatively constant and low z_o indicates not only no strong seasonal variability within this sector at Høvsøre (a stronger seasonal dependence was observed by Hasager et al. 2003 over flat terrain in Denmark), but also that the terrain is fairly flat and homogenous, which allows basic studies on wind profiles. Furthermore, the computed z_o in neutral conditions is only slightly lower than z_o found during a two month meteorological campaign at Høvsøre (**Paper IV**).

- The similarities in the values of z_o with the findings in Gryning et al. (2007) who analyzed the measurements for a narrower upwind sector, 30–90°, confirm that the influence on the wind profile at Høvsøre of the village Bøvlingbjerg is negligible (Figure 11).

- In Table 2 a slightly higher mean roughness length for neutral conditions compared to the other stability classes is listed. z_o is estimated from a fit of the observations at 10 m to Eq. (17) and, although there is a tendency of assuming higher z_o values for unstable compared to neutral conditions, slightly higher values for z_o are found for all stability conditions when the observations at Høvsøre are performed during summer periods only, as observed in **Paper V**. The unstable wind profiles in Figure 24 show an almost identical U/u_{*o} ratio at 10 m compared to the neutral wind profile, thus, by adding the diabatic correction function, ψ_m, the estimated z_o from Eq. (17) for the unstable classes becomes lower compared to neutral classes. In Gryning et al. (2007), this phenomenon was also observed in near unstable and unstable conditions at Høvsøre, but in very unstable conditions, the observed wind profile laid far left from the unstable and neutral profiles, i.e. with a low U/u_{*o} ratio, thus, showing a higher very unstable mean z_o value compared to neutral. Also from the analysis in Gryning et al. (2007) of wind speed observations at Hamburg, Germany, within an urban wind sector, the unstable profiles showed even higher U/u_{*o} ratios compared to the neutral profile, thus, the estimated z_o values for unstable classes were comparably much lower than that for the neutral class. In all these studies, the stable wind profiles always show higher U/u_{*o} ratios, resulting in lower estimations for z_o compared to the neutral classes.

- The average surface friction velocity and wind speed increase as the conditions approach neutral stability in agreement with the results in **Paper II**, **III**, **IV**, **V**, and Gryning et al. (2007).

- Sorting by Obukhov length intervals, it can be seen that convection is suppressed under neutral conditions, whereas the heat flux becomes more positive or negative in unstable and stable conditions, respectively, as expected.

5.3 The Wind Profile over the Sea

In analogy to the observations over land, the wind profiles can be also analyzed in numerous forms for the flow over the sea. In **Paper I**, for example, a problem related to wind profile analysis when the atmospheric conditions are not known is shown. In that case, 10-min mean wind profiles are averaged for different upwind sectors, and the result is a set of average wind profiles that are well predicted by the logarithmic wind profile, at least within the first 100 m AMSL, disregarding that during the campaign period, there can be observed unstable and stable conditions, as shown after a stability analysis in **Paper III**. The observations are performed at the meteorological masts located around the Horns Rev wind farm.

The problem is also illustrated in Figure 25 where wind speeds are analyzed within a free upwind sector at Horns Rev (the same used in **Paper III** for the observations in

2006). Here, intervals of wind speed based on the first measurement height are used to average the mean wind profiles and the result is also a good match with the logarithmic wind profile. z_o and u_{*o} are derived using the first two wind speed measurements and a least-squares fit of the logarithmic wind profile.

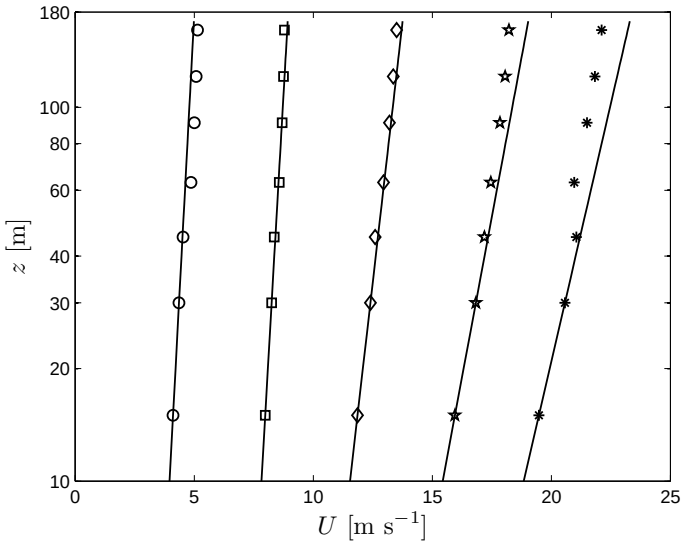

Figure 25. Average wind profiles observed within a free upwind sector at M2 at Horns Rev for different wind speed intervals based on the 15 m AMSL measurement. The markers indicate the observations and the solid lines the predictions using the logarithmic wind profile. The intervals have ±2 m s^{-1} of span and center values at 4 (circles), 8 (rectangles), 12 (diamonds), 16 (pentagrams), and 20 m s^{-1} (asterisks).

The same problem was observed from the analysis of wind speeds at M6 as shown in Peña et al. (2007). Therefore, the characteristics of the marine wind profile should be observable by analyzing the measurements in the same fashion as performed over land in Section 5.1. Nevertheless, the roughness length over the sea depends on, e.g. wind stress (Charnock 1955), wave age and fetch (Lange et al. 2004b), and wave height (Smedman et al. 2003) and it can fluctuate strongly ranging between 1×10^{-5}–1 m for the same stability condition as shown in **Paper I** and in Peña et al. (2007).

This is the background for the analysis tool developed in **Paper II**. This tool makes use of the empirical relation between the wind stress and the roughness length over the sea given in Charnock (1955):

$$z_o = \alpha_c \frac{{u_{*o}}^2}{g} \tag{40}$$

where α_c is the so-called Charnock's parameter. Charnock's relation can be used under sea states where it is appropriate and has been extensively implemented in numerous studies and applications, i.e. for atmospheric general circulation and regional climate models (Weisse and Schneggenburger 2002) and wind power meteorology (Petersen et al. 1998). It has been also extended to account for, e.g. wave age and fetch (Lange et al. 2004a) and smooth flow at low winds (Smith 1980).

In **Paper II** and **III**, it is assumed that Charnock's relation estimates well z_o when predicting the wind profile with Eq. (17). The assumption is fairly good for the open sea, which corresponds to the upwind flow conditions analyzed in both papers. Nevertheless, a wind-dependant parametrization of z_o, such as Charnock's relation, implies that the marine wind profiles predicted by Eq. (17) do not converge onto a straight line using the scaling U/u_{*o} when they are analyzed within a specific stability range, as they do over land on flat terrain for a constant roughness length. This 'phenomenon' is illustrated in

Figure 26, where 10 neutral wind profiles with friction velocities of 0.1, 0.2, ..., 1.0 m s^{-1} are plotted using the logarithmic wind profile, Eq. (16), and Charnock's relation, Eq. (40), for z_o.

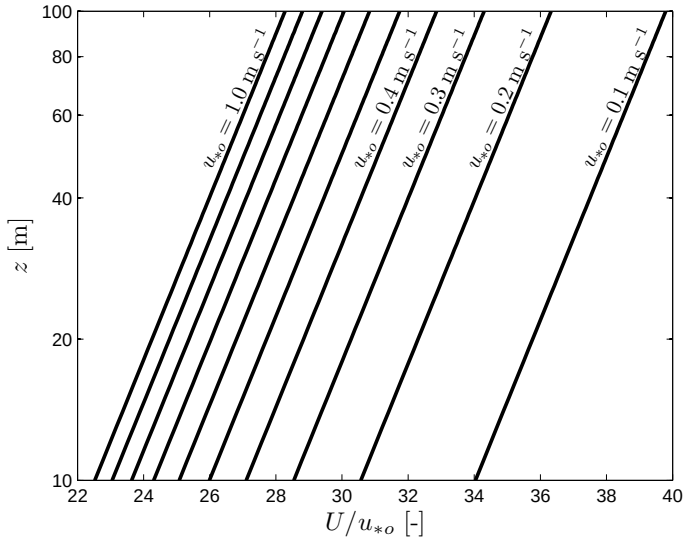

Figure 26. Marine wind profiles predicted by the logarithmic wind profile and Charnock's relation. The different profiles result for the computation of Eq. (16) using 10 different values for u_{*o}.

Paper II focuses on this problem and shows a strategy to solve it. There, the idea is to make the marine wind profiles for the same stability condition collapse. After a mathematical handling of Eqs. (17) and (40), it is demonstrated and illustrated that the wind profiles collapse, but using a new scaling:

$$\underbrace{\frac{U}{u_{*o}} + \frac{1}{\kappa}\ln\left[1 + 2\frac{\Delta u_{*o}}{\overline{u_{*o}}} + \left(\frac{\Delta u_{*o}}{\overline{u_{*o}}}\right)^2\right]}_{\dagger} + \frac{1}{\kappa}\psi_m = \underbrace{\frac{1}{\kappa}\ln\left(\frac{z}{\overline{z_o}}\right)}_{\ddagger} \tag{41}$$

where Δu_{*o} is the surface friction velocity deviation of each wind profile from the ensemble average, $\overline{u_{*o}}$, computed in each stability class, and $\overline{z_o}$ is the average roughness length defined in the same form as z_o in Eq. (40), but replacing u_{*o} with $\overline{u_{*o}}$. Eq. (41) differs from the surface-layer wind profile, Eq. (17), in the addition of the term †–a dimensionless wind speed–, to the normal scaling, U/u_{*o}. When plotting the marine wind profiles adding the term † to U/u_{*o} in the x-axis and using the term ‡–a dimensionless height–on the y-axis, the profiles become a function of ψ_m only. Due to the use of an average roughness length in the y-axis, ψ_m becomes function of $\overline{z_o}/L$. Eq. (41) corresponds to the so-called Charnock's non-dimensional wind profile, which is successfully used on observations within the free upwind sector at Horns Rev from cup anemometer wind speeds in 2004 (**Paper II**) and combined lidar/cup anemometer data in 2006 (**Paper III**).

One important criterion for the selection of marine wind profiles, which can be studied using the Charnock's non-dimensional wind profile, and applied in **Paper II** and **III** was on the drag coefficient, C_D, defined as:

$$C_D = \left(\frac{u_*}{U}\right)^2. \tag{42}$$

C_D is normally measured close to the land or sea surface. Therefore, u_* can be replaced by u_{*o} and U by Eq. (17). This results in:

$$C_D = \left(\frac{\kappa}{\ln\left(z/z_o\right) - \psi_m}\right)^2. \tag{43}$$

Thus, C_D decreases for lower z_o values and viceversa. A criterion on C_D will then determine a range on estimated sea roughness lengths. Therefore, it can be used to avoid sea states that could indicate long waves, swells, storms, fetch effects, and non-stationarity, which might be ignored by using Charnock's relation. The range is based on a weighted mean of 10 m AMSL observations, $C_{D10} = 1.3 \times 10^{-3}$, collected by Kraus (1972) from open sea conditions in the Atlantic ocean, shallow waters in the Pacific ocean and in the Baltic Sea. After applying the drag criterion and estimating the stability condition in the surface layer, it is observed that within the near-neutral stability range for the Horns Rev measurements at 15 m AMSL–indicated by the subindex N_{15}, $C_{DN15} = 1.39 \times 10^{-3}$ for the 2004 data (**Paper II**) and $C_{DN15} = 1.30 \times 10^{-3}$ for the 2006 data (**Paper III**). Garratt (1977) gave a power law relation,

$$C_{DN10} \times 10^3 = 0.51 {U_{10}}^{0.46} \tag{44}$$

from a wide review of C_D values over different seas. Applying Eq. (44) in combination with U_{10} from the neutral observations in 2004 given in **Paper II** and in 2006 in **Paper III**[10] gives $C_{DN10} = 1.60 \times 10^{-3}$ and $C_{DN10} = 1.52 \times 10^{-3}$, respectively. Thus, for both datasets, $C_{DN15} < C_{DN10}$, as expected, both being in agreement with the observations in Kraus (1972) and Garratt (1977).

5.4 Summary of the Wind Profile over the Sea

From the analysis of the marine wind profiles, the following highlights can be pointed out:

- The Charnock's non-dimensional wind profile, Eq. (41), agrees well with the observations within the first 45 m AMSL for the 2004 dataset (**Paper II**) and within the first 160 m AMSL for the 2006 dataset (**Paper III**), except for stable conditions where the observations deviate at about 40–60 m AMSL for both datasets. This is in agreement with the findings at Høvsøre in Section 5.1.

- The value for the Charnock's parameter, α_c, can be easily estimated by applying the Charnock's non-dimensional wind profiles as shown in **Paper II** for neutral conditions. This is important, because as Garratt (1977) mentioned, α_c has been observed to vary for different seas, therefore, using Eq. (41) α_c can be estimated at different sites and wind conditions, e.g. at upwind-fetch influenced sectors.

- In agreement with the observations for flow over land in Section 5.1, the values estimated in **Paper II** and **III** for the mean surface parameters, u_{*o} and U_{15}, incremented as the conditions approach neutral.

- Due to the wind speed dependence of Charnock's relation, the average z_o also increases the closer the conditions are to neutral, as expected, due to the higher wind speeds. This feature places the average wind profiles in different ranges of dimensionless heights, term ‡ in Eq. (41), and because this corresponds to the new y-axis when analyzing marine data, the wind profiles close to neutral will lie in the lowest levels, distinguishing them from the diabatic wind profiles.

- Although the mean roughness length found over the North Sea at Horns Rev in **Paper II** and **III** is between two and three orders of magnitude lower than the mean values found over flat and homogenous terrain at Høvsøre (Table 2) for equivalent atmospheric conditions, the stability has an analogous effect on z_o at both sites, i.e. it increases as the conditions approach neutral. The mean values for z_o estimated in neutral conditions over the sea are in agreement with the constant value used in the European Wind Atlas (Troen and Petersen 1989), i.e. $z_o = 0.0002$ m. Also, the

[10] For both 2004 and 2006 datasets, it is actually U_{15} the value observed, but U_{10} is derived from extrapolation of the observation at 15 m AMSL using Eq. (17) with the average z_o found in neutral conditions.

terrain corresponding to roughness class 1 in the European Wind Atlas, i.e. a typical flat land with very open areas and few windbreaks, is modeled with $z_o = 0.03$ m, which agrees with the values observed at Høvsøre for z_o in Table 2 and **Paper V**.

- C_D in Eq. (42) is used routinely in the calculation of the surface-layer momentum flux,

$$-\overline{u'w'}_o = C_{D_z} {U_z}^2 \tag{45}$$

where z is the reference height at which the observation is performed. Similarly, the surface-layer sensible heat flux, $\overline{w'\theta'}_o$ is related with the potential temperature difference over the sea as,

$$\overline{w'\Theta'}_o = C_{H_z} U_z \left(\Theta_s - \Theta_z\right) \tag{46}$$

where C_H is the bulk transfer coefficient for sensible heat and Θ_s is the sea potential temperature. Under neutral conditions C_D has been found to be close to C_H (Grachev and Fairall 1996). Thus, a value of $C_H = 1.2 \times 10^{-3}$ is assumed in **Paper I** for the 2006 dataset, in order to investigate the accuracy of Charnock's relation in neutral stability and different upwind conditions where the average wind profiles are well predicted by the logarithmic wind profile. It is found that z_o, derived from the sector-average wind profile, is close to Charnock's relation (in **Paper I** with $\alpha_c = 0.012$), although the scatter of z_o values derived from the individual 10-min wind profiles is fairly large. This is interesting, because Charnock's relation is useful when working with the average of observations.

- In **Paper III** it is found that for all the marine unstable wind profiles, the observations in 2006 agree better with the predicted profiles, Eq. (17), when the ϕ_m function, Eq. (11), is integrated using $a_1 = 19$ and $p_1 = -1/3$ that results in steeper profiles compared to those found over land at Høvsøre using $a_1 = 12$ in Section 5.1. Although the stability of the atmosphere is difficult to determine for the 2006 dataset, due to the lack of sonic anemometer measurements, the unstable observations systematically show an underestimation of the wind speed. These differences might have a strong influence on the estimation of the wind speed as illustrated in Figure 27, where several unstable flux-relationships are compared.[11] Thus, e.g. at 100 m and for $u_{*o} = 0.35$ m s^{-1}, $U = 11.5$ m s^{-1} using ϕ_m as given in Dyer (1974), whereas $U = 11.0$ m s^{-1} using ϕ_m as given in **Paper III**, i.e. a wind speed decrease of around 5%.

- By Sorting the observations according to Obukhov length intervals, the marine wind profiles show similar characteristics compared to the land wind profiles. Furthermore, two methodologies are applied to analyze the stability conditions, namely to estimate L: in **Paper II** using direct measurements of the turbulent fluxes to compute Eq. (2) and in **Paper III** using the bulk Richardson number. The wind profiles exhibit similar properties with both methodologies in the surface layer.

5.5 Extension of the Wind Profile

Until this point, the study has been concentrated on the behavior of the wind profile and the parameters that control it within the surface layer. There, the flow–for example, under neutral and steady-state conditions, is function of z and the external parameter z_o only. Under the same atmospheric conditions, but within the entire ABL, two other external parameters can be intuitively added, f_c and G, which represent the Coriolis parameter and the geostrophic wind, respectively. A dimensionless combination of these external parameters is known as the Rossby number, $\mathrm{Ro} = G/(f_c z_o)$. Other parameters related to those, like a scale height h of the boundary layer and u_{*o} probably suit better for the scaling of the flow (Blackadar and Tennekes 1968).

[11] All wind profiles are estimated using $\kappa = 0.4$, which is the actual trend, although $\kappa = 0.35$ in Businger et al. (1971)

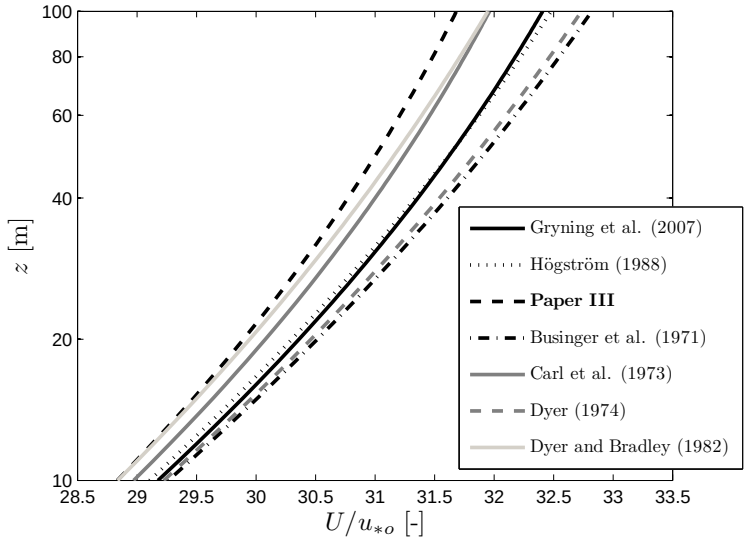

*Figure 27. Influence of the flux-profile relationships for ϕ_m on the unstable wind profile. Eq. (11) is integrated using $a_1 = 12$ and $p_1 = -1/3$ in Gryning et al. (2007), $a_1 = 19.3$ and $p_1 = -1/4$ in Högström (1988), $a_1 = 19$ and $p_1 = -1/3$ in **Paper III**, $a_1 = 15$ and $p_1 = -1/4$ in Businger et al. (1971), $a_1 = 16$ and $p_1 = -1/3$ in Carl et al. (1973), $a_1 = 16$ and $p_1 = -1/4$ in Dyer (1974), and $a_1 = 28$ and $p_1 = -1/4$ in Dyer and Bradley (1982). $\kappa = 0.4$, $L = -80$ m, and $z_o = 6 \times 10^{-5}$ m for all predictions.*

Asymptotic Similarity

In asymptotic similarity, the ABL is firstly studied for barotropic flow under neutral conditions and over homogeneous terrain. The ABL is divided in three parts:

1. A surface layer where the logarithmic wind profile is valid. By aligning u with the mean wind, both horizontal components of the velocity, u and v, are given by:

$$\frac{u}{u_{*o}} = \frac{1}{\kappa} \ln\left(\frac{z}{z_o}\right), \qquad \frac{v}{u_{*o}} = 0. \tag{47}$$

   The second part in Eq. (47) is designed to meet the conditions of velocity and stress at the surface (Blackadar and Tennekes 1968).

2. An outer layer, from the top of the ABL to a height where z_o becomes important. The equations of the flow in this layer are given by (Tennekes 1973):

$$f_c\,(v - v_g) = \frac{\partial \overline{u'w'}}{\partial z} \tag{48}$$

$$-f_c\,(u - u_g) = \frac{\partial \overline{v'w'}}{\partial z} \tag{49}$$

   where u_g and v_g are the x and y components of the geostrophic wind, $\left(G^2 = u_g^2 + v_g^2\right)$, and $\overline{u'w'}$ and $\overline{v'w'}$ are the same for the Reynolds stress, which define the friction velocity along the entire ABL:

$${u_*}^4 = \left(\overline{u'w'}\right)^2 + \left(\overline{v'w'}\right)^2 \tag{50}$$

3. A "matched" layer between the surface and the outer layer where the velocity profiles for u and v in Eqs. (47)–(49) are asymptotically matched. The assumptions and the mathematics behind the matching procedure are well described in Blackadar and Tennekes (1968) and the result is the resistance laws:

$$\frac{u_g}{u_{*o}} = \frac{1}{\kappa}\left[\ln\left(\frac{u_{*o}}{f_c z_o}\right) - A\right] \tag{51}$$

$$\frac{v_g}{u_{*o}} = -\frac{B}{\kappa} \tag{52}$$

where A and B are integration constants resulting from the matching. An interesting similarity can be found by comparing the left part of Eq. (47) and Eq. (51), i.e. replacing u_{*o}/f_c by h, the latter being the scale height of the ABL. The matching is actually allowed, because the normalized velocity deficits in Eqs. (48) and (49), $(u-u_g)/u_{*o}$ and $(v-u_g)/u_{*o}$, can be written as function of z/h only. Eqs. (51) and (52) are commonly used in the implicit forms,

$$\ln(\mathrm{Ro}) = A - \ln\left(\frac{u_{*o}}{G}\right) + \left(\frac{\kappa^2 G^2}{{u_{*o}}^2} - B^2\right)^{\frac{1}{2}}, \tag{53}$$

$$\sin\alpha = \frac{B}{\kappa}\frac{u_{*o}}{G} \tag{54}$$

where α is the angle between the surface stress and the geostrophic wind. It is not difficult to demonstrate that Eq. (53) can be rewritten into the so-called geostrophic drag law,

$$\frac{G}{u_{*o}} = \frac{1}{\kappa}\left(\left[\ln\left(\frac{u_{*o}}{f_c z_o}\right) - A\right]^2 + B^2\right)^{1/2}, \tag{55}$$

being the inverse of the left part of Eq. (55) the geostrophic drag coefficient, $C_g = u_{*o}/G$.

Diabatic conditions are included using L combined with h into the stability parameter $\mu = h/L$, resulting in A and B functions of μ (Zilitinkevich 1989).

Boundary-Layer Height

The resistance laws do not give an expression for the boundary-layer height, but it can be estimated as proportional to the scaling height h, i.e. to the ratio u_{*o}/f_c. This was already found by Rossby and Montgomery (1935) analyzing eddy-viscosity profiles in the frictional layer in adiabatic conditions. Their analysis derived the so-called Rossby-Montgomery formula for the height of the boundary layer, z_i:

$$z_i = C\frac{u_{*o}}{f_c} \tag{56}$$

where Rossby and Montgomery (1935) gave an estimate for the constant of proportionality, $C = 0.195$. Eq. (56) has been used in numerous studies of the neutral ABL, even for the SBL as shown in **Paper III** and **V**, with different values for the coefficient C ranging between 0.1 (Seibert et al. 2000) and 0.5 (Zilitinkevich and Mironov 1996). The differences are mainly related to the definition of neutral conditions used for z_i and the methods applied to derive it. Rossby and Montgomery (1935) defined it as the height where the wind becomes identical to the geostrophic value, but this might be different compared to z_i determined from profiles of momentum or heat flux, or using the inversion height from temperature profiles. In **Paper IV**, z_i was derived for neutral conditions using a linear estimation of u_* given in Panofsky (1973):

$$u_* = u_{*o} + \left(\frac{f_c v_g}{2u_{*o}}\right) z. \tag{57}$$

Defining z_i as the height where $u_* = 0$, the friction velocity can be then written in terms of z_i:

$$u_* = u_{*o}\left(1 - \frac{z}{z_i}\right) \qquad \text{where} \qquad z_i = \left(\frac{-2u_{*o}}{v_g}\right)\frac{u_{*o}}{f_c}. \tag{58}$$

z_i in Eq. (58) is equal to Eq. (56) for $C = -2u_{*o}/v_g$. Thus, by using Eq. (52), $C = 2\kappa/B$. The latter relation might partly explain the large range of C values, due to the wide

scatter found from estimations of the integration constants A and B (Zilitinkevich 1989; Hess and Garratt 2002; Hess 2004).

In stable conditions, parameterizations similar to Eq. (56) are widely found in the literature (Arya 1981; Koracin and Berkowicz 1988), some accounting for stability conditions, e.g. using L or Ri (Zilitinkevich 1989; Holtslag et al. 1990). In **Paper III**, Eq. (56) is directly used and works successfully for $C = 0.10$ when is applied in combination with the wind profile found for stable conditions over the sea. In **Paper V**, Eq. (56) also works with $C = 0.15$ for neutral and near stable, $C = 0.12$ for stable, and $C = 0.10$ for very stable conditions over land at Høvsøre. Prognostic equations for the growth of z_i in the CBL should be used. As with the SBL, there are many parameterizations in the literature and they are not as simple as Eq. (56). A broad summary of the different parameterizations is given in Seibert et al. (1998).

Mixing Length for the ABL

Based on the resistance laws, wind profile parameterizations of both horizontal wind components have been derived for the entire ABL, resulting in expressions that normally involve a set of polynomials, which are rather complicated (Long 1974; Zilitinkevich 1989; Zilitinkevich et al. 1998). An obvious alternative is the use of the mixing-length concept together with K-theory, described in Section 2.1 for the surface layer, as is shown in **Paper IV** and **V** for the entire neutral ABL. There, the Reynolds stresses in Eqs. (48) and (49), $\overline{u'w'}$ and $\overline{v'w'}$, are approximated by:

$$-\overline{u'w'} = K_m \frac{\partial u}{\partial z}, \tag{59}$$

$$-\overline{v'w'} = K_m \frac{\partial v}{\partial z}. \tag{60}$$

Defining s as the magnitude of the wind shear,

$$s = \left[\left(\frac{\partial u}{\partial z} \right)^2 + \left(\frac{\partial v}{\partial z} \right)^2 \right]^{1/2}, \tag{61}$$

and taking into account the suggestion in Prandtl (1932) for K_m close to the ground, Eq. (21), but for the entire ABL as given in Blackadar (1962),

$$K_m = \ell^2 s, \tag{62}$$

it is demonstrated that the combination of Eq. (50) with Eqs. (59)–(62) results in

$$s = \frac{u_*}{\ell}. \tag{63}$$

This equation basically states that for any given friction velocity and mixing-length parametrization, the wind shear can be derived in the ABL, but for simplicity and assuming that the wind does not turn significantly with height, s is approximated by the mean wind shear, $\partial U/\partial z$, thus,

$$\frac{\partial U}{\partial z} = \frac{u_*}{\ell}. \tag{64}$$

The Gryning's mixing-length model In Gryning et al. (2007), ℓ was modeled by inverse summation of three different length scales:

$$\frac{1}{\ell} = \underbrace{\frac{1}{\ell_{SL}}}_{\text{I}} + \underbrace{\frac{1}{\kappa \ell_{MBL}}}_{\text{II}} + \underbrace{\frac{1}{\ell_{UBL}}}_{\text{III}} \tag{65}$$

where ℓ_{SL} is the surface-layer length scale given by Eq. (24), and ℓ_{MBL} and ℓ_{UBL} are the length scales in the middle and the upper part of the ABL, respectively. ℓ_{MBL} was found

to vary with stability (Gryning et al. 2007) and ℓ_{UBL} was assumed to be proportional to the distance to z_i:

$$\ell_{UBL} = \kappa\,(z_i - z)\,. \tag{66}$$

This implies that the ϕ_m function from MOST can be used to modify the surface-layer length scale in Eq. (65).

Gryning et al. (2007) derived wind profiles for neutral, unstable, and stable conditions, based on the combination of Eq. (24) and Eqs. (65)–(66) for the mixing-length scale, the left part of Eq. (58) for the friction velocity, and then integrating the mean wind shear, Eq. (64). The parameterizations (see Appendix G) were compared to wind speed observations up to 160 m at Høvsøre, Denmark, and up to 250 m at Hamburg, Germany, showing better agreement than compared to the surface-layer wind profile, Eq. (17). The neutral wind profile was given as:

$$U = \frac{u_{*o}}{\kappa}\left[\ln\left(\frac{z}{z_o}\right) + \frac{z}{\ell_{MBL}} - \frac{z}{z_i}\left(\frac{z}{2\ell_{MBL}}\right)\right], \qquad z \gg z_o. \tag{67}$$

Thus, taking Eq. (67) at $z = z_i$ where $U = G$:

$$G = \frac{u_{*o}}{\kappa}\left[\ln\left(\frac{z_i}{z_o}\right) + \frac{z_i}{2\ell_{MBL}}\right], \tag{68}$$

and replacing G in the geostrophic drag law, Eq. (55), with the result in Eq. (68):

$$\ell_{MBL} = \frac{z_i}{2}\left[\left(\left[\ln\left(\frac{u_{*o}}{f_c z_o}\right) - A\right]^2 + B^2\right)^{1/2} - \ln\left(\frac{z_i}{z_o}\right)\right]^{-1}. \tag{69}$$

By replacing u_{*o}/f_c with z_i/C from the Rossby-Montgomery formula, ℓ_{MBL} becomes function of z_o, z_i, and the integral constants A and B in neutral conditions only.[12] Thus, the behavior of ℓ_{MBL} can be studied for different roughnesses as illustrated in Figure 28 assuming $z_i = 1000$ m, $A = 1.9$ and $B = 4.9$.

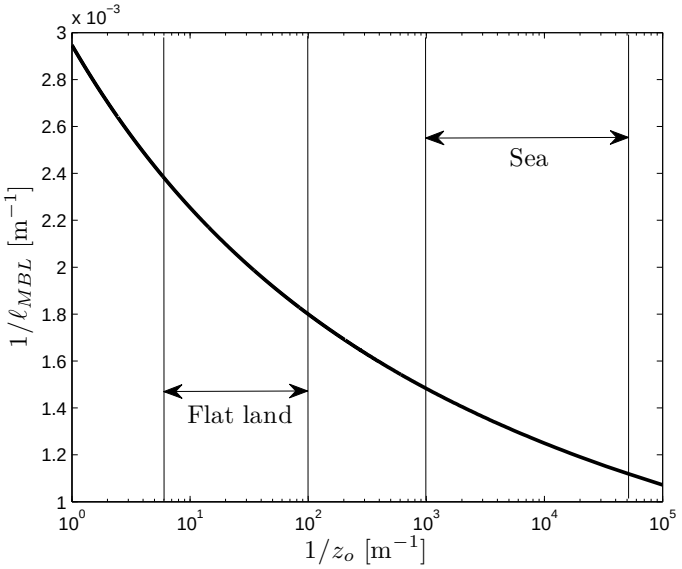

Figure 28. Middle boundary-layer length scale, ℓ_{MBL}, as a function of z_o. The relation is given by Eq. (69) with $z_i = 1000$ m, $A = 1.9$, and $B = 4.9$. The range of roughness lengths covered by flat terrain grass and sea is also shown.

Figure 28 shows that ℓ_{MBL} increases the lower the roughness of the ground, e.g. it is approximately double for flat short grass compared to sea roughnesses. Then, it is

[12] Recall that C is related with B from Eq. (58).

expected that the term II in Eq. (65) has a lower influence on ℓ over the sea than compared to land surfaces. Figure 29 illustrates the effect of each term on ℓ in Eq. (65) (left frame) and on the resulting wind profile (right frame). It is observed that by neglecting ℓ_{MBL}, curve I+III, the length scale approaches the surface-layer κz model, curve I. It is also shown that by using the friction velocity profile, Eq. (58), with the κz model only, the result is an underestimation of the wind profile compared to the straight line found by combining curve I+III with the friction velocity profile.

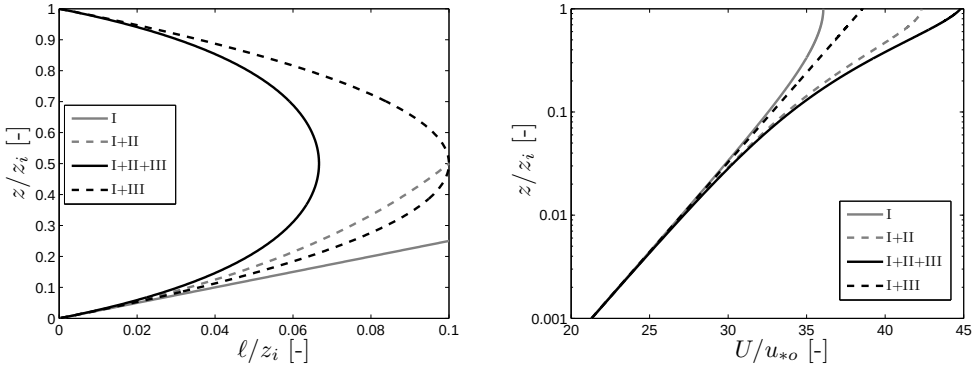

Figure 29. Profiles of length scale (left) and wind speed (right) for neutral atmospheric conditions with $z_i = 1000$ m, $z_o = 20 \times 10^{-5}$ m, and $\ell_{MBL} = 500$ m. The different lines result from the combination of the terms I ($1/\ell_{SL}$), II ($1/\ell_{MBL}$) and III ($1/\ell_{UBL}$) in Eq. (65).

Furthermore, Gryning et al. (2007) showed that ℓ_{MBL} becomes larger under stable and unstable conditions, therefore, the influence of term II should be even lower over the sea in diabatic conditions. Based on these arguments, expressions for the marine wind profile are developed in **Paper III**, i.e. neglecting the term II in Eq. (65) and integrating the mean wind shear, Eq. (64), using the friction velocity profile, Eq. (58). These are, for neutral, stable, and unstable conditions, respectively:

$$U = \frac{u_{*o}}{\kappa} \ln\left(\frac{z}{z_o}\right), \tag{70}$$

$$U = \frac{u_{*o}}{\kappa} \left[\ln\left(\frac{z}{z_o}\right) - \psi_m\left(1 - \frac{z}{2z_i}\right)\right], \tag{71}$$

$$U = \frac{u_{*o}}{\kappa} \left[\ln\left(\frac{z}{z_o}\right) - \psi_m\right]. \tag{72}$$

Eqs. (70)–(72) are equal to the surface-layer wind profile, Eq. (17) in Section 2.1, except that the stable wind profile accounts for the effect of z_i, although the arguments used for their derivation are different. Charnock's non-dimensional wind profile derived in **Paper II** and given in Eq. (41) can be easily adapted to Eq. (71) to account for z_i. In fact, it can be adapted to any formulation where the scaling U/u_{*o} is allowed. Therefore, Eqs. (70)–(72) are compared to combined lidar/cup anemometer observations up to 160 m AMSL at Horns Rev for a free stream upwind sector in **Paper III** using Charnock's non-dimensional wind profile for all stability conditions. The observations agree well with the predictions for unstable and neutral conditions. Accounting for z_i in the stable wind profiles, the agreement is better using Eq. (71) than compared to the surface-layer wind profile, Eq. (17). As mentioned before, the Rossby-Montgomery formula with $C = 0.10$ is used to estimate z_i for all stable wind profiles.

Mixing-length profile in the ABL The wind profile parameterizations in Gryning et al. (2007) were found to perform well compared to wind speed observations over land

and by analyzing the behavior of ℓ_{MBL} with z_o, another set of wind profile parameterizations are devised for flow over the open sea in **Paper III**, which also compare well to the observations. Nevertheless, no evidence of a mixing-length scale that varies as shown in the profiles of Figure 29 (left frame) has yet been shown.

Lettau (1950) reanalyzed the well-known "Leipzig wind profile", which corresponds to wind speed observations from 28 pitot-balloons on a 20 October near Leipzig, Germany (Mildner 1932). The description of the Leipzig wind profile, as well as an historical review of the authors that have analyzed it, is given in **Paper IV**. Here, it should be mentioned that the analysis of Lettau (1950) is based on ideal considerations of the relation between wind and stress within an uniform and adiabatic frictional layer. The result of his analysis is the profile of both horizontal wind components, u and v, and of *Austausch* coefficient, A_c, up to 950 m. The mixing length for the Leipzig wind profile can be derived from Eq. (62) replacing K_m by A_c/ρ:

$$\ell = \left(\frac{A_c}{\rho s} \right)^{1/2} . \tag{73}$$

The eddy viscosity and mixing-length profiles derived from Lettau's analysis are illustrated in Figure 30 as well as their surface-layer forms in neutral conditions, Eqs. (19) and (23). The differences between the derived profiles and the surface-layer forms for both K_m and ℓ are remarkable above the surface layer. The latter extends to the first 50–100 m assuming $z_i = 880$ m, which corresponds to the peak of wind speed in Lettau (1950). The mixing length is observed to reach a value $\ell \approx 32$ m at 650 m and, then, decreases with height.

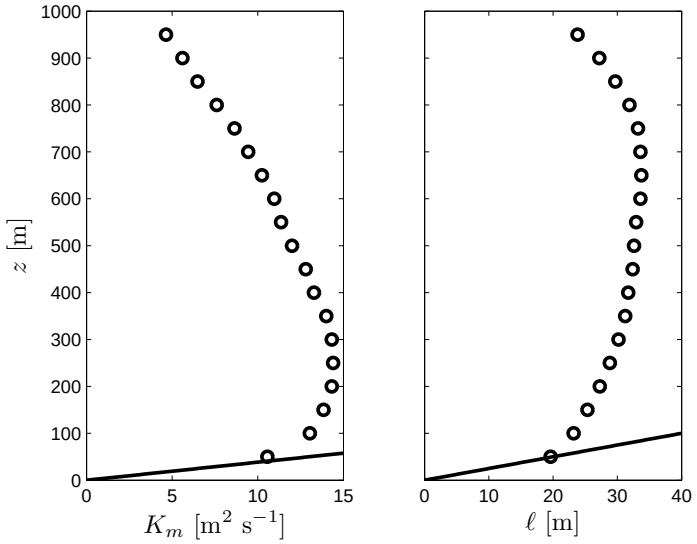

Figure 30. Profiles of eddy viscosity, K_m, (left frame) and mixing length, ℓ, (right frame) derived from the re-analysis of the Leipzig wind profile by Lettau (1950) (circles). The solid lines correspond to the surface-layer profiles, $K_m = \kappa u_{*o} z$ and $\ell = \kappa z$, assuming $u_{*o} = 0.65$ m s^{-1} from Lettau (1950).

During the last 50 years, several mixing-length models have been implemented to numerically solve the equations of the flow, Eqs. (48) and (49), with relatively little computational effort, easily, and showing good results, e.g. compared to the Leipzig wind profile (Appendix E). Some of the most well-known models, Blackadar (1962) and Lettau

(1962), Panofsky (1973),[13] and Ohmstede and Appleby (1964), respectively, are:

$$\text{I}: \quad \ell = \frac{\kappa z}{1 + \left(\frac{\kappa z}{\eta}\right)^p}, \tag{74}$$

$$\text{II}: \quad \ell = \eta \tanh\left(\frac{\kappa z}{\eta}\right), \tag{75}$$

$$\text{III}: \quad \ell = \eta\left[1 - \exp\left(-\frac{\kappa z}{\eta}\right)\right] \tag{76}$$

where Blackadar (1962) suggested $\eta = 0.00027G/f_c$ and $p = 1$ for Eq. (74), later rewritten by Panofsky (1973) as $\eta = 0.0063u_{*o}/f_c$ to use with Eqs. (74) and (75), i.e. the geostrophic drag coefficient is assumed to be constant, $C_g = 4.28 \times 10^{-2}$. Lettau (1962) also proposed a mixing-length parametrization as Eq. (74), but with $p = 5/4$, and later Estoque (1973) suggested $\eta = 0.0294u_{*o}/f_c$ for Lettau's model. Ohmstede and Appleby (1964) fitted $\eta = 32$ m in Eq. (76) to the Leipzig's mixing-length profile in Figure 30 (right frame). The parameter η acts as a limiting value for the mixing length above the surface layer, therefore, η in Eq. (76) can be also related to the ratio u_{*o}/f_c. In fact, assuming $\eta = 0.0063u_{*o}/f_c$ and the values in Lettau (1950), $\eta = 36$ m.

Neutral wind profile for homogeneous terrain

In numerical solutions as shown in Appendix E, mixing-length models as functions of the ratio G/f_c are preferable, because Eqs. (48) and (49) are functions of u_g and v_g. For practical applications, where surface parameters are measured, ℓ is preferable as a function of u_{*o}/f_c. Furthermore, under neutral conditions, the ratio u_{*o}/f_c can be replaced by z_i/C from the Rossby-Montgomery formula, Eq. (56), i.e. it is assumed,

$$\eta = D\frac{u_{*o}}{f_c} = D\frac{z_i}{C} \tag{77}$$

where D is close to 63×10^{-4} according to Blackadar (1962). In **Paper IV**, a collection of mixing-length models, Eqs. (23), (65), (74), and (75), are used to derive parameterizations of the neutral wind profile by integration of the mean wind shear, Eq. (64). As done in **Paper III**, the model used for the friction velocity profile is given by Eq. (58). The resulting new neutral wind profiles, from the I (with $p = 1$ and $p = 5/4$) and II mixing-length models using Eq. (77) for η, respectively, are:

$$U = \frac{u_{*o}}{\kappa}\left[\ln\left(\frac{z}{z_o}\right) - \left(\frac{z}{z_i}\right)^2 \frac{\kappa C}{2D} - \frac{z}{z_i}\left(1 - \frac{\kappa C}{D}\right)\right] \tag{78}$$

$$U = \frac{u_{*o}}{\kappa}\left[\ln\left(\frac{z}{z_o}\right) - \frac{z}{z_i}\left(1 - \frac{4\kappa C}{5D}\left(\frac{C\kappa z}{z_i D}\right)^{\frac{1}{4}}\right) - \frac{4\kappa C}{9D}\left(\frac{z}{z_i}\right)^2\left(\frac{C\kappa z}{z_i D}\right)^{\frac{1}{4}}\right] \tag{79}$$

$$U = \frac{u_{*o}}{\kappa}\left[\ln\left(\frac{\sinh\left(\frac{Cz\kappa}{z_i D}\right)}{\sinh\left(\frac{Cz_o\kappa}{z_i D}\right)}\right) - \left(\frac{z}{z_i}\right)^2 \frac{C\kappa}{2D}\right] \tag{80}$$

where the values $D = 73 \times 10^{-4}$, 58×10^{-4}, and 100×10^{-4} are found in **Paper IV** by fitting the mixing-length parameterizations, Eq. (74) for $p = 1$ and $p = 5/4$ and Eq. (75), to the Leipzig wind profile data.[14] C is found from analyzing the behavior of the integral constants A and B with the ratio $u_{*o}/f_c z_o$ when different estimations for z_o, z_i, and u_{*o} used for the Leipzig wind profile are compared from the literature (Lettau 1962;

[13] In Panofsky (1973) the model is referred to a previous work by Blackadar et al. (1969), but such model cannot be found in the original manuscript.

[14] The length scale model III, by Ohmstede and Appleby (1964), gives an unpractical solution for the wind profile, therefore, it is not presented, whereas some small terms are neglected in the solution using the II length-scale model, i.e. Eq. (80).

Ohmstede and Appleby 1964; Hess 2004; Bergmann 2006). By fixing a value $A = 1.7$ and defining $z_i = 880$ m, which is the wind speed maximum in Lettau (1950), $C = 0.15$ and $z_o = 0.11$ m. Thus, the wind profile models, Eqs. (78)–(80), are compared with the Leipzig wind profile in **Paper IV** (illustrated here in Figure 31) together with the logarithmic wind profile, Eq. (16), and the neutral wind profile by Gryning et al. (2007), Eq. (67). For the latter, the suggested parametrization for ℓ_{MBL} in Gryning et al. (2007) is used, but also in terms of the ratio z_i/C:

$$\ell_{MBL} = \frac{z_i/C}{-2\ln\left(\frac{z_i}{Cz_o}\right) + 55}. \tag{81}$$

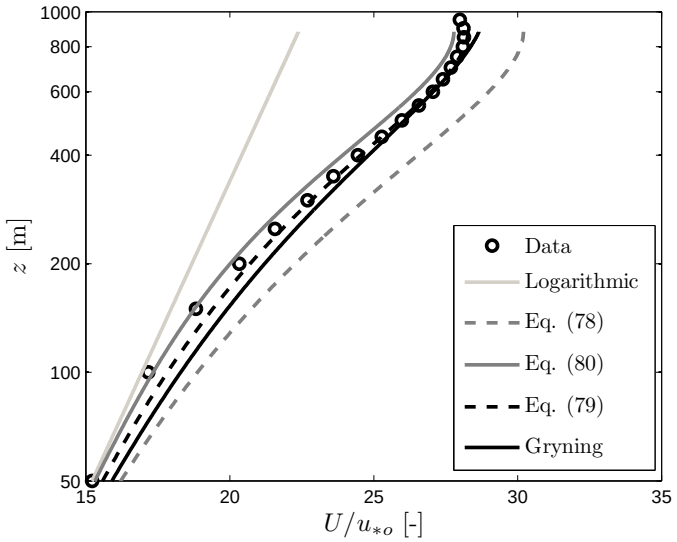

Figure 31. Wind speed profiles for the Leipzig wind profile (Data). The models are evaluated using $\kappa = 0.4$, $z_o = 0.11$ m, $z_i = 880$ m, and $C = 0.15$. $D = 73 \times 10^{-4}$, $D = 100 \times 10^{-4}$, and $D = 58 \times 10^{-4}$, for Eqs. (78), (79), and (80), respectively.

The agreement of the models and the Leipzig wind profile is fairly good. The highest deviations are found for the logarithmic wind profile, which is a good fit to the observations within the surface layer only, and for the model in Eq. (78) that systematically overestimates the wind speed at all heights. Although the Leipzig wind profile has been traditionally considered a near-neutral, near-barotropic experiment, there is an ongoing discussion about the surface conditions of the experiment (Bergmann 2006; Hess 2006). Therefore, the wind profile models are also compared to the observations at Høvsøre in **Paper IV**, which can be used for the study of the neutral wind profile over flat and homogenous terrain, as shown in Section 5.1 and in Gryning et al. (2007). At Høvsøre, the wind profile observed with the cup anemometers up to 160 m can be extended up to 300 m using measurements from a WindCube lidar placed at the meteorological mast during two winter months. The mean surface parameters measured during this relatively short campaign do not differ from the climatological values given in Table 2 for neutral conditions. The average z_o for the winter campaign is 1 mm lower than the climatological z_o, thus, it is assumed that the neutral wind profile is representative of the climatological conditions at Høvsøre.

The mixing-length profile at Høvsøre is found using Eq. (64) and the friction velocity profile from Eq. (58). The mixing-length models, Eq. (65) and models I–II in terms of the ratio z_i/C, agree well with the observations using the same values for C and D as with the Leipzig wind profile. The comparison of the wind profile parameterizations with the Høvsøre observations up to 300 m also shows good agreement for the models in Eqs.

(67), (79), and (80), and higher deviations when compared to the logarithmic wind profile beyond the surface layer and to the model in Eq. (78) at all heights.

Diabatic wind profile for homogeneous terrain

As done above for neutral conditions, the diabatic wind profile over homogeneous and flat terrain can be derived combining the approximation for the mean wind shear, Eq. (64), the friction velocity model, Eq. (58), and a mixing-length parametrization. This is shown in **Paper V** for the mixing-length form in Eq. (74), which is here rewritten as the inverse summation of two length scales:

$$\frac{1}{\ell} = \frac{1}{\kappa z}\phi_m + \frac{(\kappa z)^{p-1}}{\eta^p}. \tag{82}$$

In Eq. (82), the ϕ_m function is already added to account for stability conditions, which extends the surface-layer length scale κz. In **Paper V**, it is demonstrated that the wind profiles for neutral, unstable, and stable conditions, respectively, are then given as:

$$U = \frac{u_{*o}}{\kappa}\left[\ln\left(\frac{z}{z_o}\right) + \frac{1}{p}\left(\frac{\kappa z}{\eta}\right)^p - \left(\frac{1}{1+p}\right)\frac{z}{z_i}\left(\frac{\kappa z}{\eta}\right)^p - \frac{z}{z_i}\right], \tag{83}$$

$$U = \frac{u_{*o}}{\kappa}\left[\ln\left(\frac{z}{z_o}\right) - \psi_m + \frac{1}{p}\left(\frac{\kappa z}{\eta}\right)^p - \left(\frac{1}{1+p}\right)\frac{z}{z_i}\left(\frac{\kappa z}{\eta}\right)^p - \frac{z}{z_i}\right], \tag{84}$$

$$U = \frac{u_{*o}}{\kappa}\left[\ln\left(\frac{z}{z_o}\right) + b_1\frac{z}{L}\left(1 - \frac{z}{2z_i}\right) + \frac{1}{p}\left(\frac{\kappa z}{\eta}\right)^p - \left(\frac{1}{1+p}\right)\frac{z}{z_i}\left(\frac{\kappa z}{\eta}\right)^p - \frac{z}{z_i}\right] \tag{85}$$

Evaluating Eq. (83) for $p = 1$ and $p = 5/4$ and replacing η with Eq. (77), the neutral wind profiles in Eqs. (78) and (79) are obtained.

The comparison of the wind profile parameterizations in Eqs. (83)–(85) for $p = 1$ and $p = 5/4$ with wind speed measurements up to 300 m from combined lidar/cup anemometer observations within the flat and homogeneous upwind sector at Høvsøre in **Paper V** is notably better than compared to the surface-layer wind profile, Eq. (17), for near-neutral and stable conditions. For unstable conditions, the comparison is not as precise in the first meters, because the measurements showed a pronounced wind speed over-speeding at about 130 m which the wind profile model, Eq. (84), corrected.

Following the same procedure as done before when the behavior of ℓ_{MBL} was observed for different roughness lengths, the neutral wind profile in Eq. (83) can be evaluated at $z = z_i$, i.e. when $U = G$, and the result can be combined with the geostrophic drag law, Eq. (55), in order to estimate the value of η. This gives

$$\eta = \frac{\kappa z_i}{[p(1+p)]^{1/p}}\left[\left(\left[\ln\left(\frac{u_{*o}}{f_c z_o}\right) - A\right]^2 + B^2\right)^{1/2} + 1 - \ln\left(\frac{z_i}{z_o}\right)\right]^{-1/p}. \tag{86}$$

In **Paper V**, Eq. (86) is found to agree well with a least-squares fitting of η from Eqs. (83)–(85) of the wind speed measurements using both $p = 1$ and $p = 5/4$, not only for neutral conditions, but also for stable and unstable conditions. This is achieved by selecting values for A and B, in accordance to the behavior of these parameters illustrated by Zilitinkevich (1975), when evaluated as functions of the dimensionless stability $\kappa u_{*o}/f_c L$. Therefore, the behavior of η for different roughness lengths can be observed not only for neutral conditions, but for diabatic conditions, as illustrated in Figure 32. For three stability conditions, it is observed that η increases the lower the roughness of the ground, as found for ℓ_{MBL} in neutral conditions. For low roughness lengths, found over water surfaces, η increases as well as the length scale ℓ. This results in length scales closer to their values in the surface layer, thus, to wind profiles closer to the surface-layer wind profile, Eq. (17) in the surface layer, a behavior shown previously in Figure 29 (right) when the term $1/\kappa\ell_{MBL}$ in Eq. (65) is neglected. Figure 32 also shows that the influence of z_o on η is lower for $p = 5/4$ compared to $p = 1$ for the three stability conditions. Thus,

from the comparison of the models with the wind speed measurements in **Paper V** and from the results in Figure 32, a slightly more conservative result is found when using the models with $p = 5/4$.

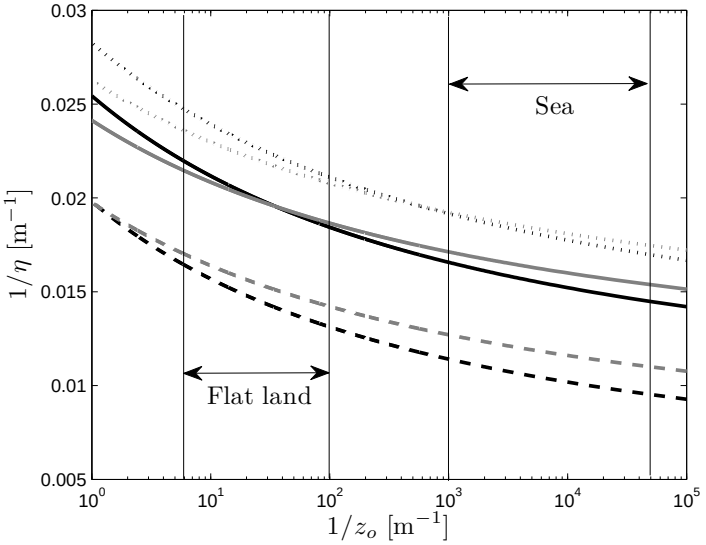

Figure 32. The limiting length scale, η, as a function of z_o. The relation is given by Eq. (86) with $z_i = 500$ m, $u_{*o} = 0.25$ m s^{-1}, and $f_c = 1.21 \times 10^{-4}$ s^{-1}. The solid lines represent neutral conditions ($A = 1.7$ and $B = 5$), dashed lines unstable conditions ($A = 2.1$ and $B = 4.6$), and dotted lines stable conditions ($A = 1.5$ and $B = 5.2$). The evaluation for $p = 1$ is shown in black lines and for $p = 5/4$ in gray lines. The range of roughness lengths covered by flat terrain grass and sea is also shown.

5.6 Summary of the Extension of the Wind Profile

The basic ideas and results from the extension of the wind profile are shortly mentioned:

- Under neutral conditions and within the surface layer, there are two external parameters, z and z_o, for the atmospheric flow. For the entire neutral ABL, the parameters f_c and G are added, which can be related to the boundary-layer height, z_i.
- The resistance laws are the relationships between the rather constant momentum fluxes in the neutral surface layer and the varying momentum fluxes in the ABL far beyond surface layer. These fluxes are functions of f_c and G.
- The boundary-layer height is proportional to the scaling height $h = u_{*o}/f_c$, as shown in **Paper IV** for near-neutral conditions and **Paper V** for near-neutral and stable conditions. It is also shown that the proportionality constant between h and z_i depends on the integral constants A and B of the resistance laws, thus, the wide range of values of A and B, even for ideal neutral conditions (Zilitinkevich 1989), might be related to the wide range of diagnostic equations for z_i found in the literature (Seibert et al. 1998; Seibert et al. 2000).
- The mean wind shear in the ABL, $\partial U/\partial z$, has been modeled as the ratio of the local friction velocity and the local length scale or mixing length (**Paper III**, **IV**, and **V**), in order to derive parameterizations of the wind profile for a wide range of stability conditions. The wind shear model results from the approximation of the local momentum fluxes as functions of the local wind gradients, which is also used for the surface layer applying K-theory, and from the assumption that the wind does not turn significantly with height.

- The neutral mixing length is measured beyond surface layer in **Paper IV** and compared to different models of length scale for the entire ABL. The models, based on the mixing-length concept (Blackadar 1962; Lettau 1962; Gryning et al. 2007), correct the constant increasing length scale of the surface layer, κz, fitting well the length scale measurements of the Leipzig wind profile up to 950 m and of the Høvsøre wind profile up to 300 m. The wind profile parameterizations, based on such mixing-length models, agree better with the wind speed measurements at Leipzig and at Høvsøre than compared to the logarithmic wind profile.

- The mixing-length model in Gryning et al. (2007) is analyzed for flow over the sea in **Paper III** where the term related to limiting length scale, $1/\kappa\ell_{MBL}$, is neglected, due to the high value of ℓ_{MBL} over the smooth water surface. The wind profile parameterizations derived from this analysis conform to the traditional surface-layer wind profile when the effect of z_i is neglected, although the physical assumptions for their derivation are different. These parameterizations agree well with the wind speed measurements within the free upwind sector at Horns Rev up to 160 m AMSL and are particularly better for the stable wind profile than compared to the surface-layer wind profile.

- In **Paper V** wind profile parameterizations are compared to wind speed measurements up to 300 m and for a wide range of stability classes observed at the flat and homogeneous upwind sector at Høvsøre. They are derived from the mixing length models in Blackadar (1962), Lettau (1962), and Gryning et al. (2007), and are extended to account for diabatic conditions using MOST. The comparison shows better agreement for all the models for near-neutral and stable conditions than compared to the traditional surface-layer wind profile. The latter gives better results for unstable conditions within the first tens of meters, but does not correct for the wind speed over-speeding in the measurements, which is followed by the derived wind profile models. It is also shown that the limiting value for the length scale, η, of the models in Blackadar (1962) and Lettau (1950), follows the behavior for different roughness lengths found for the length scale ℓ_{MBL} in the model of Gryning et al. (2007), i.e. η becomes higher the smoother the surface, approaching the surface-layer length scale κz in the surface layer. Thus, for water surfaces the wind profile models, Eqs. (83)–(85), are expected to be close to the predictions from the traditional surface-layer wind profile in the surface layer.

5.7 Turbulence and Spectra

The mixing-length scale in Eq. (64), here rewritten as,

$$\ell = \frac{u_*}{\partial U/\partial z}, \tag{87}$$

is nothing else than the length scale of the wind profile, which by definition, depends on the wind shear, $\partial U/\partial z$, shear stress, u_*, and buoyancy that was accounted for using MOST as shown in Section 2.1. Another length scale, which also depends on the buoyancy and shear, is related to the size of the turbulent eddies that represent the scale of turbulence in the ABL. Therefore, a relation is expected between both length scales.

The Fourier analysis of boundary-layer fluctuations is a useful tool to study the different scales of atmospheric turbulent motion. A typical energy spectrum of turbulence, properly Fourier transformed, shows a peak in the so-called energy-containing range that, as cited by Kaimal and Finnigan (1994), 'contains the bulk of the turbulent energy and where energy is produced by buoyancy and shear'. As also mentioned by Kaimal and Finnigan (1994) the peak within the energy-containing range 'represents the size of the eddies with most energy'. The size of such eddies corresponds to the turbulent length scale that is investigated and compared to the length scale derived from Eq. (87) in **Paper IV**. There,

the u- and w-spectra and uw-co-spectra are analyzed using the frequency-weighted forms, normalized by u_* as established for MOST, i.e. $fS_{u,w}/{u_*}^2$ and $fC_{uw}/{u_*}^2$, respectively, in the dimensionless frequency scale, $n = fz/U$, where f is the frequency in Hz. This is because as Kaimal et al. (1972) and Højstrup (1982) showed, the spectral representations also follow similarity laws.

In **Paper IV**, 617 10-min time series are found simultaneously at the different heights where the sonic anemometers are installed at Høvsøre, i.e. at 10, 20, 40, 60, 80, 100, and 160 m, within the flat upwind sector, 30°–125°, and under near-neutral conditions, $|L| \geq 500$. The Fourier transformed time series are averaged at each height on the dimensionless frequency and two spectral models, those of Mann (1994) and Kaimal et al. (1972), are fitted to the average u- and v-spectra and uw-co-spectra, in order to determine the wavelength of their spectral peaks, λ_m. In the CBL, the spectral peak was studied by Kaimal et al. (1976) and found no dependency on height for the u- and v-components even at heights very close to the ground,

$$(\lambda_m)_{u,v} = 1.5 z_i, \tag{88}$$

but a dependency on height for the w-component in the surface layer, $z \leq 0.1 z_i$, correspondent to the free-convection limit,

$$(\lambda_m)_w = 5.9 z, \tag{89}$$

which was improved by Caughey and Palmer (1979) above surface layer, $0.1 z_i \leq z \leq z_i$,

$$(\lambda_m)_w = 1.8 z_i \left[1 - \exp(-4z/z_i) - 0.0003 \exp(8z/z_i)\right]. \tag{90}$$

A dependency on height is also found in **Paper IV** for the peaks of the average w-spectra and uw-co-spectra in near-neutral conditions. From the model of Mann (1994), a length scale, L_M, also related to the size of the eddies, is numerically computed for the spectra at all sonic anemometer heights and it is found a constant proportionality between the length scale of the profile, Eq. (87), and L_M, namely $\ell = \beta_M L_M$. With $\beta_M = 0.438$, both profiles of length scale, i.e. from Eq. (87) and $\beta_M L_M$, agree well from 10 up to 160 m and with the mixing-length models, Eqs. (65), (74), and (75), using the same values for C and D as with the Leipzig wind profile. The value $\beta_M = 0.438$ is derived from the findings of Mann (1994) for L_M from measurements at a flat-bottomed fjord on Zealand, Denmark.

The wavelengths of the spectra and co-spectra peaks, $(\lambda_m)_{u,w,uw}$, are also determined using the spectral forms in Kaimal and Finnigan (1994):

$$\frac{fS_u(f)}{{u_*}^2} = \frac{102 m_u n}{(1 + 33 m_u n)^{\frac{5}{3}}} \tag{91}$$

$$\frac{fS_w(f)}{{u_*}^2} = \frac{2.1 m_w n}{1 + 5.3 (m_w n)^{\frac{5}{3}}} \tag{92}$$

$$\frac{-fC_{uw}(f)}{{u_*}^2} = \frac{12 m_{uw} n}{(1 + 9.6 m_{uw} n)^{\frac{7}{3}}} \tag{93}$$

where $m_{u,w,uw}$ are constants introduced to fit the forms to the measurements. From Mann (1994), the relation between the wavelength peaks and L_M can be derived, e.g. $L_M = (\lambda_m)_w/(2\pi 0.5)$ and $L_M = (\lambda_m)_{uw}/(2\pi 2.3)$, thus, these are also related to a length scale and their behavior with height also compare well with the measurements of length scale from Eq. (87) and with the models, Eqs. (65), (74), (75), and κz, using the same values for C and D derived before. This is here illustrated in Figure 33.

The findings described above are of great importance, because a relationship between the turbulence spectral peaks and the length scale of the wind profile is shown, at least for near-neutral conditions. In fact, under diabatic conditions similar relationships seem to work as well. Under very unstable conditions in Figure 6, $\phi_m \approx 0.5$ for $z/L = -2$, thus, the unstable length scale in the surface layer, ℓ_{SL}, is given from Eq. (24),

$$\ell_{SL} = (\ell_{SL})_N \, {\phi_m}^{-1} \approx 2 \, (\ell_{SL}) = 2\kappa z. \tag{94}$$

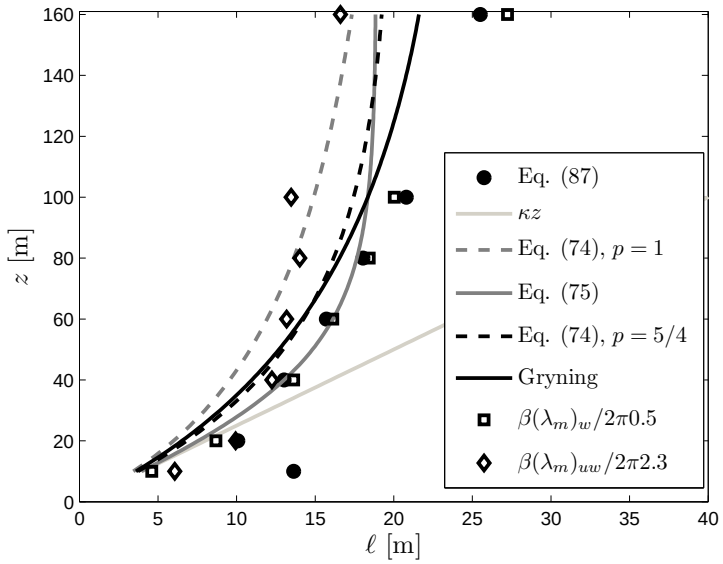

Figure 33. Length-scale profiles from the wind speed observations at Høvsøre, Eq. (87), compared to the models and to the w and uw spectral peaks using $\beta = 0.438$. The models are evaluated using $\kappa = 0.4$, $z_i = 880$ m, and $C = 0.15$. $D = 73 \times 10^{-4}$, $D = 100 \times 10^{-4}$, and $D = 58 \times 10^{-4}$, for the estimation of η in Eq. (77) and used for Eq. (74) with $p = 1$ and $p = 5/4$, and Eq. (75), respectively.

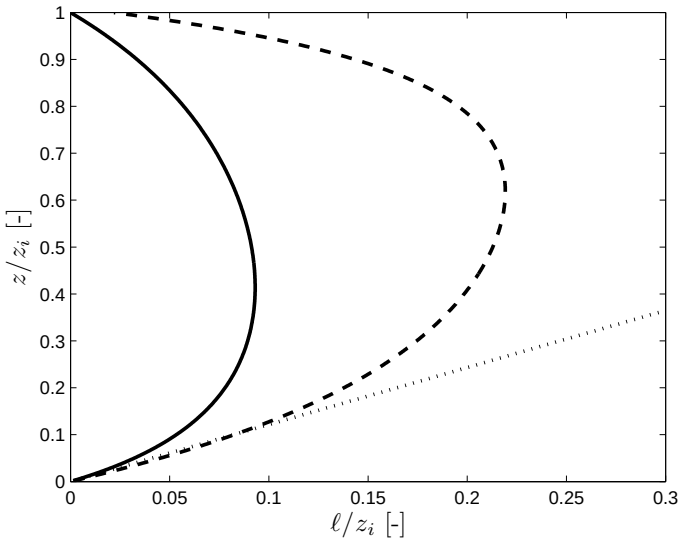

Figure 34. Profiles of length scale for the unstable ABL. The solid line corresponds to the model of Gryning et al. (2007), Eq. (65), correcting ℓ_{SL} with ϕ_m as shown in Eq. (24) and applying $z_i = 560$ m and $\ell_{MBL} = 405$ m, the dashed line to Eq. (95) replacing $(\lambda_m)_w$ with Eq. (90), and the dotted line to Eq. (95) replacing $(\lambda_m)_w$ with Eq. (89).

The length scale is related to $(\lambda_m)_w$ in **Paper IV** as

$$\ell = \frac{\beta_M \, (\lambda_m)_w}{2\pi 0.5} \tag{95}$$

applying the relationships between ℓ and L_M given above. Replacing $(\lambda_m)_w$ in Eq. (95) with Eq. (89) gives $\ell = (\beta_M 5.9/\pi)z \approx 2\kappa z$ that is equal to the approximation in Eq. (94). In the same fashion, the behavior of the length scale above the surface layer in unstable

conditions can be compared between the findings of Caughey and Palmer (1979), i.e. replacing $(\lambda_m)_w$ in Eq. (95) with Eq. (90), and a length scale model used for wind profile parametrization in Section 5.5. Figure 34 illustrates such comparison for the length scale of Gryning et al. (2007), Eq. (65), using the values for z_i and ℓ_{MBL} found in **Paper V** for very unstable conditions and assuming $\phi_m = 0.5$ for the correction of the surface-layer length scale. Although the profile derived from the findings in Caughey and Palmer (1979) doubles the values of the length scale derived from Gryning et al. (2007), due probably to a different relationship between ℓ and $(\lambda_m)_w$ for unstable conditions above the surface layer than that given in Eq. (95), both show a decreasing length scale at $z \gtrsim 0.5 z_i$.

6 Conclusions

The wind profile in and beyond the surface layer has been measured by combining traditional wind speed measurements from cup anemometers with lidar observations. Such combination is possible, due to the high correlation and agreement between the traditional instruments and the lidar sensing technique found at all the possible lidar/cup overlapping heights at two different sites: over water at the Horns Rev wind farm in the Danish North Sea and over land at the National Test Station of Wind Turbines located at Høvsøre, Denmark.

The wind speed measurements performed within a flat and homogeneous upwind sector at Høvsøre and within a fetch- and wake-free upwind sector at Horns Rev show a good agreement compared to the traditional surface-layer wind profile in the layer of the atmosphere where the surface layer is extended and for a wide range of atmospheric stability conditions. The comparison is accomplished by averaging the 10-min wind profile measurements for similar stability conditions, based on intervals of Obukhov lengths observed from either turbulent fluxes from sonic anemometer measurements or bulk formulations close to the zero reference height, and by scaling the mean horizontal wind speed with the surface-layer friction velocity, U/u_{*o}.

It is found that the scaling U/u_{*o} is not sufficient for the analysis of the wind profile over the sea, due to the variant roughness length of the water. By assuming that the sea roughness length depends on the wind stress as proposed by Charnock (1955), a dimensionless wind speed should be added to the scaling U/u_{*o} in order to make the wind profiles for similar stability conditions collapse.

The mixing-length proposed by Gryning et al. (2007) is revisited for the modeling of the wind profile over the sea. For smooth surfaces such as water, the results conform to the traditional-surface wind profile, except for stable conditions where the boundary-layer height, z_i, appears as a scaling parameter. For the stable stability classes, the models agree better with wind speed measurements up to 160 m AMSL at Horns Rev than compared to the surface-layer wind profile. The boundary-layer height, z_i, is estimated using the Rossby-Montgomery formula, which accounts for the contribution of mechanical turbulence only.

At Høvsøre, wind speed measurements performed up to 300 m in near-neutral stability conditions show a wind speed over-speeding when compared to the logarithmic wind profile, as observed from the reanalysis of the Leipzig wind profile up to 950 m. The length scale of the wind profile, derived from wind speed measurements, is compared to several mixing-length models showing a notably better agreement than compared to the indefinitely increasing surface-layer length scale κz. Wind profile models, derived from those mixing-length models, which also take z_i into account, compare better to the wind speed measurements from Leipzig and Høvsøre than the logarithmic wind profile.

The neutral length scale derived from a spectral analysis of turbulence measurements at Høvsøre up to 160 m, further beyond the surface layer, is proportional to the length scale derived from the wind speed profiles, in agreement with the findings within the surface layer of Mann (1994) at a flat-bottomed fjord on Zealand, Denmark.

Two mixing-length parameterizations are extended to account for a wide range of stability conditions, as MOST corrects the surface-layer length scale κz, and used to derive wind profile models for flow over flat land and homogeneous terrain where z_i is included as a scaling parameter for the whole range of stability conditions, as shown in the models of Gryning et al. (2007). The derived wind profile models and those of Gryning et al. (2007) are particularly better when compared to the surface-layer wind profile, by analyzing wind speed measurements up to 300 m at Høvsøre for near-neutral and stable conditions. For unstable conditions, an over-speeding is not predicted by the traditional wind profile, but followed by the other models.

Ceilometer measurements also averaged within intervals of Obukhov lengths, show a

characteristic aerosol backscatter profile, which is useful to estimate z_i in near-neutral and unstable conditions. The estimations of z_i from ceilometer observations in near-neutral conditions compare well with z_i estimated from the Rossby-Montgomery formula.

Lidar observations are not only useful for wind profiling, but also for the estimation of turbulence characteristics such as the momentum flux in and above the surface layer. Although the current conical lidar filters turbulence, due to the its large measurement volume, the observations are in good agreement with sonic anemometer measurements at Høvsøre and with bulk-derived turbulence observations at Horns Rev.

The findings of this PhD study help in the understanding and modeling of the physical processes of the atmosphere, the global and regional climate, and in particular, they have a direct impact and a practical application in the growing wind power industry, in which there is a need for an accurate and detailed description of the wind profile in the first 100–200 m above the ground where the modern wind turbines operate, due to power and load optimization.

Appendices

Appendix A: Derivation of the Obukhov length

The Obukhov length, L, can be derived from the budget of turbulent kinetic energy assuming horizontal homogeneous conditions (Stull 1988):

$$\frac{\partial e}{\partial t} = \underbrace{\frac{g}{T}\overline{w'\Theta'}}_{\text{I}} \underbrace{- \overline{u'w'}\frac{\partial U}{\partial z}}_{\text{II}} - \frac{1}{\rho}\frac{\partial}{\partial z}\left(\overline{P'w'}\right) - \frac{\partial}{\partial z}\left(\overline{e'w'}\right) - \epsilon \tag{A-1}$$

where e is the turbulent kinetic energy, $\overline{w'\Theta'}$ the kinematic heat flux, $\overline{u'w'}$ the momentum flux, $\overline{P'w'}$ the pressure-vertical velocity covariance, $\overline{e'w'}$ the vertical flux of turbulent kinetic energy, ϵ the viscous dissipation, and Θ the potential temperature. Taking into account the buoyant and mechanical production of turbulence only, i.e. terms I and II, respectively, Eq. (A-1) gives,

$$\frac{\partial e}{\partial t} = \frac{g}{T}\overline{w'\Theta'} - \overline{u'w'}\frac{\partial U}{\partial z}. \tag{A-2}$$

Assuming steady state, i.e. $\partial e/\partial t = 0$, and replacing $-\overline{u'w'}$ by ${u_*}^2$ and $\partial U/\partial z$ by $u_*/\kappa z$, Eq. (A-2) gives,

$$\frac{g}{T}\overline{w'\Theta'} = -{u_*}^2\frac{u_*}{\kappa z}, \tag{A-3}$$

and taking L in Eq. (A-3) as the height where the terms I and II equal gives,

$$L = -\frac{{u_*}^3 T}{\kappa g \overline{w'\Theta'}}. \tag{A-4}$$

Appendix B: Conversion of temperatures into potential and virtual temperatures

The following set of formulas are used to convert the temperature into potential and virtual temperatures:

$$\Theta = T\left(\frac{P_o}{P}\right)^{0.286}, \tag{B-1}$$

$$\Theta_v = \Theta\left(1 + 0.61r\right) \tag{B-2}$$

where P is the air pressure, P_o is a reference pressure–or the surface pressure–usually set to 100 kPa, and r is the mixing ratio of unsaturated air. To the first order,

$$\Theta = T + \left(g/c_p\right) z_{ref} \tag{B-3}$$

where z_{ref} is the height difference from the 100 kPa level. Eq. (B-3) is commonly used instead of Eq. (B-1). The ratio g/c_p is the adiabatic lapse rate, $\approx 1°\text{C}/100$ m. However, the relative humidity, RH, is usually measured instead of r. Therefore, the following set of equations can be used to convert RH into r (Tetens 1930; Stull 1988):

$$r = \frac{0.622 e_p}{P - e_p}, \tag{B-4}$$

$$e_p = e_s\frac{RH}{100}, \tag{B-5}$$

$$e_s = 6.1078 \times 10^{7.5T/(237.3+T)} \tag{B-6}$$

where e_p is the partial pressure of water vapor and e_s the saturated vapor pressure. The specific humidity, q, is then easily estimated as,

$$q = \frac{r}{1+r}. \tag{B-7}$$

Appendix C: Estimation of the dimensionless wind shear from measurements

The wind shear, $\partial U/\partial z$, can be approximated as U_d/Z_d. However, a better estimate is done when wind speed measurements are available at several heights. Högström (1988) approximated the wind profile using a second-order polynomial in $\ln z$,

$$U = U_o + A_b \ln z + B_a \ln z^2 \tag{C-1}$$

where U_o, A_b, and B_a are fitted parameters determined by a least-squares method. The wind shear results from the differentiation of Eq. (C-1),

$$\frac{\partial U}{\partial z} = \frac{A_b + 2B_a \ln z}{z}. \tag{C-2}$$

Introducing Eq. (C-2) into Eq. (9), the dimensionless wind shear, ϕ_m, can be estimated as,

$$\phi_m = \frac{\kappa}{u_{*o}} \left(A_b + 2B_a \ln z\right). \tag{C-3}$$

Appendix D: Diabatic correction of the surface-layer wind profile

The diabatic correction function, ψ_m, in Eq. (17) is derived from the integration of the ϕ_m function:

$$\psi_m = \int_0^{z/L} \frac{1 - \phi_m(\xi)}{\xi} d\xi. \tag{D-1}$$

Thus, for neutral conditions where $\phi_m = 1$, $\psi_m = 0$. For stable conditions it gives:

$$\psi_m = -b_1 \frac{z}{L}. \tag{D-2}$$

Under unstable conditions the expression depends on the value of p_1 (Stull 1988; Gryning et al. 2007):

$$\psi_m = 2\ln\left(\frac{1+x}{2}\right) + \ln\left(\frac{1+x^2}{2}\right) - 2\arctan(x) + \frac{\pi}{2}, \qquad p_1 = -1/4, \tag{D-3}$$

$$\psi_m = \frac{3}{2}\ln\left(\frac{1+x+x^2}{3}\right) - \sqrt{3}\arctan\left(\frac{2x+1}{\sqrt{3}}\right) + \frac{\pi}{\sqrt{3}}, \qquad p_1 = -1/3 \tag{D-4}$$

where $x = \left(1 - a_1 \frac{z}{L}\right)^{-p_1}$.

Appendix E: Numerical solution of the flow in the ABL using mixing-length/K-theory

Based on Estoque and Bhumralkar (1970), the equations of the ABL flow over homogeneous terrain are:

$$-f_c v = -f_c v_g + \frac{\partial}{\partial z}\left(K_m \frac{\partial u}{\partial z}\right), \tag{E-1}$$

$$f_c u = f_c u_g + \frac{\partial}{\partial z}\left(K_m \frac{\partial v}{\partial z}\right), \tag{E-2}$$

which are equal to Eqs. (48) and (49), but the Reynolds stresses, $\overline{u'w'}$ and $\overline{v'w'}$, are already replaced using K-theory. For temperature and moisture are given by:

$$0 = \frac{\partial}{\partial z}\left(K_m \frac{\partial \Theta}{\partial z}\right), \tag{E-3}$$

$$0 = \frac{\partial}{\partial z}\left(K_m \frac{\partial q}{\partial z}\right). \tag{E-4}$$

For any given mixing-length model, ℓ, the K_m profile is derived as shown from Eqs. (61) and (62):

$$K_m = \ell^2 \left[\left(\frac{\partial u}{\partial z} \right)^2 + \left(\frac{\partial v}{\partial z} \right)^2 \right]^{1/2}. \tag{E-5}$$

The unknowns, u, v, Θ, and q are computed between the ground, $z = 0$ where $u = 0$, $v = 0$, $\Theta = \Theta_o$, and $q = q_o$, up to the top of the boundary layer, $z = h$ where $u = u_g$, $v = v_g$, $\Theta = \Theta_h$, and $q = q_h$. Finite difference equations are obtained by applying Eqs. (E-1) and (E-2) to the interior points, $z(2)$, $z(3)$,..., $z(k)$,..., $z(N-1)$:

$$\begin{aligned} -f_c v(k) &= -f_c v_g + \frac{2\widehat{K_m}\left(k+\frac{1}{2}\right)[u(k+1)-u(k)]}{[z(k+1)-z(k)][z(k+1)-z(k-1)]} \\ &\quad - \frac{2\widehat{K_m}\left(k-\frac{1}{2}\right)[u(k)-u(k-1)]}{[z(k)-z(k-1)][z(k+1)-z(k-1)]}, \end{aligned} \tag{E-6}$$

$$\begin{aligned} f_c u(k) &= f_c u_g + \frac{2\widehat{K_m}\left(k+\frac{1}{2}\right)[v(k+1)-v(k)]}{[z(k+1)-z(k)][z(k+1)-z(k-1)]} \\ &\quad - \frac{2\widehat{K_m}\left(k-\frac{1}{2}\right)[v(k)-v(k-1)]}{[z(k)-z(k-1)][z(k+1)-z(k-1)]}. \end{aligned} \tag{E-7}$$

And for Eqs. (E-3) and (E-4),

$$\frac{\widehat{K_m}\left(k+\frac{1}{2}\right)[\Theta(k+1)-\Theta(k)]}{[z(k+1)-z(k)]} - \frac{\widehat{K_m}\left(k-\frac{1}{2}\right)[\Theta(k)-\Theta(k-1)]}{[z(k)-z(k-1)]} = 0, \tag{E-8}$$

$$\frac{\widehat{K_m}\left(k+\frac{1}{2}\right)[q(k+1)-q(k)]}{[z(k+1)-z(k)]} - \frac{\widehat{K_m}\left(k-\frac{1}{2}\right)[q(k)-q(k-1)]}{[z(k)-z(k-1)]} = 0. \tag{E-9}$$

The eddy viscosity is approximated by centered differences,

$$\widehat{K_m}\left(k+\frac{1}{2}\right) = \widehat{\ell}^2\left(k+\frac{1}{2}\right)\left[\left(\frac{\widehat{u}(k+1)-\widehat{u}(k)}{z(k+1)-z(k)} \right)^2 + \left(\frac{\widehat{v}(k+1)-\widehat{v}(k)}{z(k+1)-z(k)} \right)^2 \right]^{1/2} \tag{E-10}$$

By replacing k by $k-1$ in Eq. (E-10), $\widehat{K_m}\left(k-\frac{1}{2}\right)$ is obtained. The $\wedge$ symbol indicates the latest computational step. The unknowns are calculated iterating until they reach the accuracy needed. First approximations of the unknowns are computed with a constant K_m for the entire ABL. Figure 35 illustrates the results of the numerical modeling of the Leipzig wind profile using four different mixing-length models, Eq. (74) for $p = 1$ and $p = 5/4$ and Eqs. (75) and (76). Both modeled u and v wind speed components show well agreement with the data.

Appendix F: Lidar conical scanning over complex terrain

The analytical solution for the potential flow around a cylinder is well known in the literature:

$$u_r = U_\infty \left[1 - (R/r_o)^2 \right] \cos\delta, \tag{F-1}$$

$$u_\delta = -U_\infty \left[1 + (R/r_o)^2 \right] \sin\delta \tag{F-2}$$

where u_r and u_δ are the radial and tangential velocities for a point at an angle δ separated from the center of the cylinder a distance r_o, R is the radius of the cylinder, and U_∞ is the undisturbed velocity (see Figure 36). The velocity to be measured is at a height h_o above the lidar, which following Eq. (F-2) is:

$$U = U_\infty \left[1 + (R/(h_o + R))^2 \right]. \tag{F-3}$$

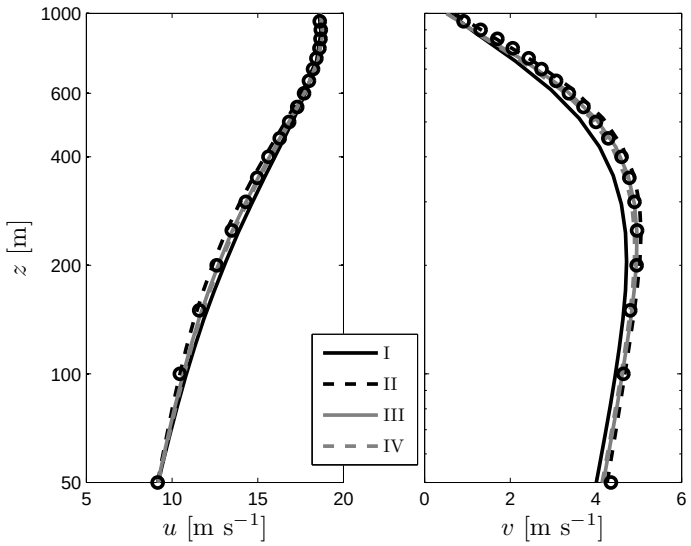

Figure 35. Numerical modeling of the u and v components of the velocity of the Leipzig wind profile. The data from Lettau (1950) is shown in circles. The results using the I, II, and III mixing-length models, Eq. (74) for $p = 1$ and $p = 5/4$ and Eqs. (75) and (76), are shown with different line types.

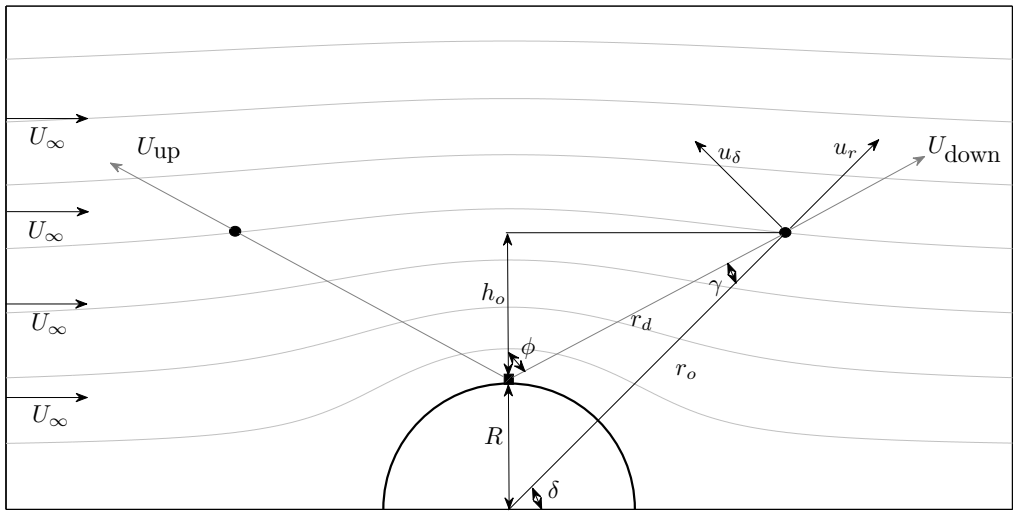

Figure 36. Simulation of potential flow over a cylindrical hill with a lidar (square) over it.

The lidar measures radial velocities at an angle ϕ from the zenith. Therefore, the lidar observation, U_{l}, is a function of the radial upstream and downstream velocities:

$$U_{\text{l}} = \frac{U_{\text{down}} - U_{\text{up}}}{2 \sin \phi}. \tag{F-4}$$

Following the geometry in Figure 36, U_{down} and U_{up} can be written in terms of the radial and tangential velocities:

$$U_{\text{down}} = u_r \cos\gamma - u_\delta \sin\gamma, \tag{F-5}$$

$$U_{\text{up}} = -u_r \cos\gamma + u_\delta \sin\gamma \tag{F-6}$$

where γ is the angle between r_o and the lidar distance to the target point, r_d. Replacing Eqs. (F-1) and (F-2) in Eqs. (F-5) and (F-6) and the result in Eq. (F-4), the velocity

deficit observed by the lidar, U_l/U, will be given by:

$$\frac{U_\mathrm{l}}{U} = \frac{\left[1-(R/r_o)^2\right]\cos\delta\cos\gamma + \left[1+(R/r_o)^2\right]\sin\delta\sin\gamma}{\left[1+(R/(h_o+R))^2\right]\sin\phi}. \tag{F-7}$$

The velocity deficit is not a function of the undisturbed velocity, but of the geometry of the lidar scanning configuration and the cylinder only. The angles δ and γ and the distance r_o in Eq. (F-7) can be derived sequentially using the scanning geometry:

$$\cot\delta = \frac{h_o\tan\phi}{h_o+R}, \tag{F-8}$$

$$r_o = \frac{h_o+R}{\sin\delta}, \tag{F-9}$$

$$\sin\gamma = \frac{R\cos\delta}{(h_o^2+r_o^2\cos^2\delta)}. \tag{F-10}$$

Figure 37 shows the deficit of horizontal wind speed observed by the lidar, Eq. (F-7), as a function of a dimensionless height, h_o/R, for different scanning angles ϕ.

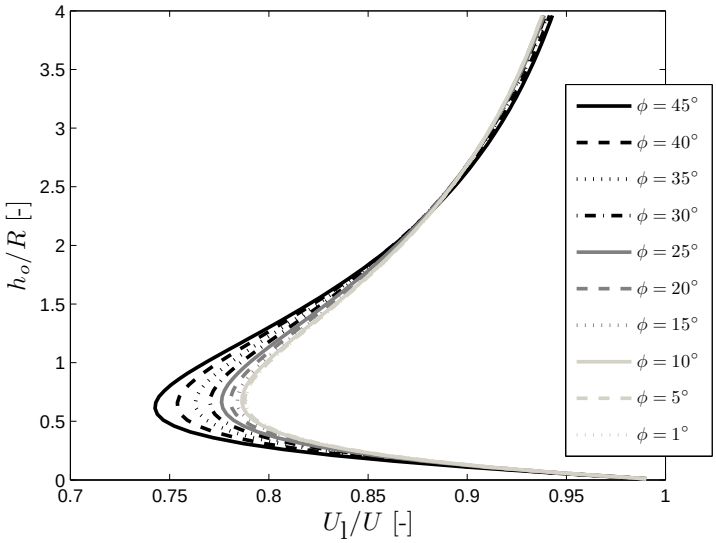

Figure 37. Deficit of horizontal wind speed, U_l/U, from lidar at different relative heights, h_o/R, and zenith angles, ϕ.

Appendix G: Gryning et al. (2007) models for the diabatic wind profile

To account for diabatic atmospheric conditions, the mixing-length parametrization in Gryning et al. (2007), Eq. (65), was corrected using the ϕ_m function on the surface-layer length scale κz:

$$\frac{1}{\ell} = \frac{1}{\kappa z}\phi_m + \frac{1}{\kappa\ell_{MBL}} + \frac{1}{\kappa\,(z-z_i)} \tag{G-1}$$

Using Eq. (G-1) for neutral conditions, i.e. $\phi_m = 1$, in combination with the friction velocity profile, Eq. (58), and the mean wind shear, Eq. (64), the neutral wind profile is given as:

$$U = \frac{u_{*o}}{\kappa}\left[\ln\left(\frac{z}{z_o}\right) + \frac{z}{\ell_{MBL}} - \frac{z}{z_i}\left(\frac{z}{2\ell_{MBL}}\right)\right]. \tag{G-2}$$

Gryning et al. (2007) showed that the diabatic wind profile for unstable and stable conditions, respectively, is given as:

$$U = \frac{u_{*o}}{\kappa}\left[\ln\left(\frac{z}{z_o}\right) - \psi_m + \frac{z}{\ell_{MBL}} - \frac{z}{z_i}\left(\frac{z}{2\ell_{MBL}}\right)\right], \quad \text{(G-3)}$$

$$U = \frac{u_{*o}}{\kappa}\left[\ln\left(\frac{z}{z_o}\right) + b_1\frac{z}{L}\left(1 - \frac{z}{2z_i}\right) + \frac{z}{\ell_{MBL}} - \frac{z}{z_i}\left(\frac{z}{2\ell_{MBL}}\right)\right]. \quad \text{(G-4)}$$

Notation

a_1	parameter for the convective dimensionless wind shear
a_2	parameter for the convective dimensionless temperature gradient
A	integration constant from the asymptotic matching
A_b	fitted parameter for the wind profile
A_c	*Austausch* coefficient
A_t	receiver aperture area
ABL	atmospheric boundary layer
AMSL	above mean sea level
b_1	parameter for the stable dimensionless wind shear
b_2	parameter for the stable and convective dimensionless temperature gradient
B	integration constant from the asymptotic matching
B_a	fitted parameter for the wind profile
B_o	mean backscatter coefficient above the entrainment layer
B_u	mean backscatter coefficient below the entrainment layer
c	parameter for the convective dimensionless wind shear
c_l	speed of light
c_p	specific heat of the air
C	proportionality constant for the height of the boundary layer
C_{AB}	power spectral density of the covariance of variables A and B
C_D	drag coefficient
C_{DN}	neutral drag coefficient
C_g	geostrophic drag coefficient
C_H	bulk transfer coefficient for sensible heat
C_1	parameter for the relationship between L and Ri_b
C_2	parameter for the relationship between L and Ri_b
CBL	convective boundary layer
CW	continuous wave
d	focused distance
d_t	transmitter/receiver aperture diameter
d'	distance from the laser source to targets in the air
D	parameter for the limiting length scale
e	turbulent kinetic energy
e_p	partial pressure of water vapor
e_s	saturated vapor pressure
ez	entrainment layer thickness
E_o	effective pulse energy
$\overline{e'w'}$	vertical flux of turbulent kinetic energy
f	frequency
f_c	Coriolis parameter
FFT	fast Fourier transform
FWHM	full width at half maximum
g	gravitational acceleration
G	geostrophic wind
h	scaling height of the boundary layer
h_o	measurement height above the lidar
H	kinematic heat flux
HWHM	half width at half maximum
I	turbulence intenstity
k	number for indexing
$\mathbf{k}$	wavenumber vector
K_m	turbulent exchange coefficient for momentum or eddy viscosity

l_w	WindCube's length for the full width at half maximum weighting function
l_z	Rayleigh length
L	Obukhov length
L_M	length scale from the Mann (1994) spectral model
LLJ	low-level jet
LST	local standard time
m_A	fit constant for the A-spectra using the Kaimal and Finnigan (1994) model
min	minute
MOST	Monin-Obukhov similarity theory
n	dimensionless frequency
$\mathbf{n}$	unit vector in the beam direction
N	number of grid points
NPS	normalized power spectrum
p	parameter for the growth of the length scale
p_1	parameter for the convective dimensionless wind shear
p_2	parameter for the convective dimensionless temperature gradient
P	instantaneous power
P	air pressure
P_o	reference air pressure or surface air pressure
$\overline{P'w'}$	pressure-vertical velocity covariance
q	specific humidity
q_h	specific humidity at the top of the boundary layer
q_o	specific humidity at the ground
r	mixing-ratio of unsaturated air
r_d	radial distance from the lidar to the target
r_o	radial distance from the center of a hill to the target
R	radius of a cylinder
Ri	gradient Richardson number
Ri_b	bulk Richardson number
Ro	Rossby number
s	magnitude of the wind shear
S_A	power spectral density of the variable A
SBL	stable boundary layer
t	time
t_d	time delay
T	temperature
T_o	surface-layer temperature
u	longitudinal component of the wind velocity
$\mathbf{u}$	wind velocity vector
u_g	longitudinal component of the geostrophic wind
u_r	radial velocity
u_δ	tangential velocity
u_*	friction velocity
u_{*o}	surface-layer friction velocity
$\overline{u'w'}$	momentum flux or kinematic flux of u-momentum in the vertical
U	horizontal wind speed magnitude
U_d	wind speed difference
U_{def}	wind speed deficit from lidar measurements
U_{down}	downstream lidar wind speed
U_l	lidar wind speed observation
U_o	fitted parameter for the wind profile
U_{up}	upstream lidar wind speed
U_∞	undisturbed velocity
v	latitudinal component of the wind velocity

v_g	latitudinal component of the geostrophic wind
v_r	radial, along-beam, or line-of-sight lidar velocity
$\mathbf{v_r}$	radial velocity vector
$\overline{v'w'}$	kinematic flux of v-momentum in the vertical
w	vertical component of the wind velocity
$\overline{w'\Theta'}$	kinematic heat flux
$\overline{w'\Theta_v{}'}$	vertical flux of virtual potential temperature
$\overline{w'\Theta_v{}'}_o$	surface-layer vertical flux of virtual potential temperature
$\mathbf{x}$	coordinate field
z	height above the surface or reference height
z_d	height difference
z_i	height of the boundary layer
z_o	roughness length
z_{ref}	height difference from the 100 kPa level

Greek characters

α	angle between the surface and geostrophic wind
α_c	Charnock's parameter
β	volume backscatter coefficient
β_M	proportionality parameter for the length scale
γ	angle between r_d and r_o
Γ	extinction coefficient
δ	cylindrical angle
ϵ	viscous dissipation
η	limiting value for the length scale
θ	azimuth angle
θ_d	wind direction
Θ	potential temperature
Θ_o	potential temperature at the ground
Θ_h	potential temperature at the top of the boundary layer
Θ_s	sea potential temperature
Θ_v	virtual potential temperature
Θ_{vd}	virtual potential temperature difference
Θ_{*o}	surface-layer scaling temperature
κ	von Kármán constant
λ_l	wavelength of the laser beam
λ_m	wavelength of the spectral peak
μ	stability parameter for the boundary layer
ξ	variable of integration
π	3.14159
ρ	air density
σ	standard deviation
σ^2	variance
τ	pulse length
ϕ	zenith or inclination angle
ϕ_m	dimensionless wind shear
ϕ_h	dimensionless temperature gradient
$\mathbf{\Phi}_{ij}$	spectral tensor
φ	along-beam weighting function
ψ_m	diabatic correction of the logarithmic wind profile
ω_o	angular frequency of light

Special symbols

$\overline{()}$	average operator or ensemble average
$()'$	fluctuation from the mean value
$\widehat{()}$	last computational step
$\widetilde{()}$	weighted value
$\cdot$	vector product
ℓ	mixing length
ℓ_{MBL}	middle boundary-later length scale
ℓ_{SL}	surface-layer mixing length
ℓ_{UBL}	upper boundary-layer length scale
$(\ell_{SL})_N$	neutral surface-layer mixing length
∂	partial derivative
$\wedge$	logical conjunction
∞	infinity
$\triangle$	deviation from the mean value
$\triangle f$	Doppler-shifted frequency

References

Ainslie, J. F., 1988: Calculating the flowfield in the wake of wind turbines. *J. Wind Eng. Ind. Aerodyn.*, **27**, 213–224.

Antoniou, I., H. E. Jørgensen, T. Mikkelsen, S. Frandsen, R. Barthelmie, C. Perstrup, and M. Hurtig, 2006: Offshore wind profile measurements from remote sensing instruments. *Proc. of the European Wind Energy Association Conf. & Exhibition*, Athens.

Arya, S. P. S., 1981: Parameterizing the height of the stable atmospheric boundary layer. *J. Appl. Meteor.*, **20**, 1192–1202.

Bergmann, J. C., 2006: Comments on: 'The neutral, barotropic planetary boundary layer, capped by a low-level jet inversion'. *Bound.-Layer Meteor.*, **119**, 171–179.

Bhumralkar, C. M., 1975: A survey of parameterization techniques for the planetary boundary layer in atmospheric circulation models. Defense Advanced Research Projects Agency R-1653-ARPA. ARPA order No. 189-1, 84 pp.

Blackadar, A. K., 1962: The vertical distribution of wind and turbulent exchange in a neutral atmosphere. *J. Geophys. Res.*, **67**, 3095–3102.

Blackadar, A. K., J. A. Dutton, H. A. Panofsky, and A. Chaplin, 1969: Investigation of the turbulent wind field below 150 m altitude at the eastern test range. NASA Tech. Rep. NASA CR-1410, 92 pp.

Blackadar, A. K. and H. Tennekes, 1968: Asymptotic similarity in neutral barotropic planetary boundary layers. *J. Atmos. Sci.*, **25**, 1015–1020.

Businger, J. A., J. C. Wyngaard, Y. Izumi, and E. F. Bradley, 1971: Flux-profile relationships in the atmospheric surface layer. *J. Atmos. Sci.*, **28**, 181–189.

Carl, D. M., T. C. Tarbell, and H. A. Panofsky, 1973: Profiles of wind and temperature from towers over homogeneous terrain. *J. Atmos. Sci.*, **30**, 788–794.

Caughey, S. J. and S. G. Palmer, 1979: Some aspects of turbulence structure through the depth of the convective boundary layer. *Quart. J. Roy. Meteor. Soc.*, **105**, 811–827.

Charnock, H., 1955: Wind stress over a water surface. *Quart. J. Roy. Meteor. Soc.*, **81**, 639–640.

Deardorff, J. W., 1968: Dependence of air–sea transfer coefficients on bulk stability. *J. Geophys. Res.*, **73**, 2549–2557.

Dyer, A. J., 1974: A review of flux-profile relatioships. *Bound.-Layer Meteor.*, **7**, 363–372.

Dyer, A. J. and E. F. Bradley, 1982: An alternative analysis of flux-gradient relationships at the 1976 ITCE. *Bound.-Layer Meteor.*, **22**, 3–19.

Eberhard, W. L., R. E. Cupp, and K. R. Healy, 1989: Doppler lidar measurement of profiles of turbulence and momentum flux. *J. Atmos. Ocean. Tech.*, **6**, 809–819.

Emeis, S., C. Münkel, S. Vogt, W. J. Müller, and K. Schäfer, 2004: Atmospheric boundary-layer structure from simultaneous SODAR, RASS, and ceilometer measurements. *Atmos. Env.*, **38**, 273–286.

Emeis, S. and K. Schäfer, 2006: Remote sensing methods to investigate boundary-layer structures relevant to air pollution in cities. *Bound.-Layer Meteor.*, **121**, 377–385.

Emeis, S., K. Schäfer, and C. Münkel, 2008: Long-term observations of the urban mixing-layer height with ceilometers. *Earth Environ. Sci.: Conf. Ser.*, **1**, 012 027 (9 pp).

Eresmaa, N., A. Karppinen, S. M. Joffre, J. Säsänen, and H. Talvitie, 2006: Mixing height determination by ceilometer. *Atmos. Chem. Phys.*, **6**, 1485–1493.

Estoque, M. A., 1973: Numerical modeling of the planetary boundary layer. *Workshop on Micrometeorology*, D. A. Haugen, Ed., American Meteorology Society, 217–270.

Estoque, M. A. and C. M. Bhumralkar, 1970: A method for solving the planetary boundary-layer equations. *Bound.-Layer Meteor.*, **1**, 169–194.

Foken, T., 2006: 50 years of the Monin-Obukhov similarity theory. *Bound.-Layer Meteor.*, **119**, 431–447.

Garratt, J. R., 1977: Review of drag coefficients over oceans and continents. *Mon. Wea. Rev.*, **105**, 915–929.

Grachev, A. A. and C. W. Fairall, 1996: Dependence of the Monin-Obukhov stability parameter on the bulk Richardson number over the ocean. *J. Appl. Meteor.*, **36**, 406–414.

Gryning, S.-E., E. Batchvarova, B. Brümmer, H. Jørgensen, and S. Larsen, 2007: On the extension of the wind profile over homogeneous terrain beyond the surface layer. *Bound.-Layer Meteor.*, **124**, 251–268.

Gryning, S.-E., A. A. M. Holtslag, J. S. Irwin, and B. Sivertsen, 1987: Applied dispersion modelling based on meteorological scaling parameters. *Atmos. Environ.*, **21**, 79–89.

Gryning, S.-E., A. A. A. P. van Ulden, and S. Larsen, 1983: Dispersion from a continuous ground-level source investigated by a K model. *Quart. J. Roy. Meteor. Soc.*, **109**, 355–364.

Hasager, C. B., N. W. Nielsen, N. O. Jensen, E. Boegh, J. H. Christensen, E. Dellwik, and H. Soegaard, 2003: Effective roughness calculated from satellite-derived land cover maps and hedge-information used in a weather forecasting model. *Bound.-Layer Meteor.*, **109**, 227–254.

Hess, G. D., 2004: The neutral, barotropic planetary boundary layer, capped by a low-level inversion. *Bound.-Layer Meteor.*, **110**, 319–355.

Hess, G. D., 2006: Reply to: "Comments on: The neutral, barotropic planetary boundary layer, capped by a low-level jet inversion". *Bound.-Layer Meteor.*, **119**, 181–194.

Hess, G. D. and J. R. Garratt, 2002: Evaluating models of the neutral, barotropic planetary boundary layer using integral measures: part I. Overview. *Bound.-Layer Meteor.*, **104**, 333–358.

Högström, U., 1988: Non-dimensional wind and temperature profiles in the atmospheric surface layer: a re-evaluation. *Bound.-Layer Meteor.*, **42**, 55–78.

Højstrup, J., 1982: Velocity spectra in the unstable boundary layer. *J. Atmos. Sci.*, **39**, 2239–2248.

Holtslag, A. A. M., 1984: Estimates of diabatic wind speed profiles from near-surface weather observations. *Bound.-Layer Meteor.*, **29**, 225–250.

Holtslag, A. A. M., E. I. F. D. Bruin, and H.-L. Pan, 1990: A high resulution air mass tranformation model for short range weather forecasting. *Mon. Wea. Rev.*, **92**, 235–242.

Holtslag, A. A. M. and F. T. M. Nieuwstadt, 1986: Scaling the atmospheric boundary layer. *Bound.-Layer Meteor.*, **36**, 201–209.

Izumi, Y. and M. L. Barad, 1970: Wind speeds as measured by cup and sonic anemometers and influenced by tower structure. *J. Appl. Meteor.*, **9**, 851–856.

Jørgensen, H. E., T. Mikkelsen, S.-E. Gryning, S. Larsen, P. Astrup, and P. E. Sørensen, 2008: Measurements from Høvsøre met mast. Tech. Rep. Risø-R-1592(EN), Risø National Laboratory, 32 pp.

Kaimal, J. C. and J. J. Finnigan, 1994: *Atmospheric boundary layer flows: Their structure and measurement*. Oxford University press, 289 pp.

Kaimal, J. C., J. C. Wyngaard, and D. A. Haugen, 1968: Deriving power spectra from a three-component sonic anemometer. *J. Appl. Meteor.*, **7**, 827–837.

Kaimal, J. C., J. C. Wyngaard, D. A. Haugen, O. R. Coté, Y. Izumi, S. J. Caughey, and C. J. Readings, 1976: Turbulence structure in the convective boundary layer. *J. Atmos. Sci.*, **33**, 2152–2169.

Kaimal, J. C., J. C. Wyngaard, Y. Izumi, and O. R. Cote, 1972: Spectral characteristics of surface-layer turbulence. *Quart. J. Roy. Meteor. Soc.*, **98**, 563–589.

Kindler, D., A. Oldroyd, A. MacAskill, and D. Finch, 2007: An eight month test campaign of the QinetiQ ZephIR system: Preliminary results. *Meteor. Z.*, **16 (5)**, 479–489.

Koracin, D. and R. Berkowicz, 1988: Nocturnal boundary layer height: observations by acoustic sounders and prediction in terms of surface layer parameters. *Bound.-Layer Meteor.*, **65**, 65–83.

Kraus, E. B., 1972: *Atmosphere-Ocean interaction*. Oxford University Press, 275 pp.

Kristensen, L., 1993: The cup anemometer and other exciting instruments. Tech. Rep. Risoe-R-615(EN), Risø National Laboratory, 83 pp.

Lange, B., S. Larsen, J. Højstrup, and R. Barthelmie, 2004a: Importance of thermal effects and the sea surface roughness for offshore wind resource assessment. *J. Wind Eng. Ind. Aerodyn.*, **92**, 959–988.

Lange, B., S. Larsen, J. Højstrup, and R. Barthelmie, 2004b: The influence of thermal effects on the wind speed profile of the coastal marine boundary layer. *Bound.-Layer Meteor.*, **112**, 587–617.

Lettau, H., 1950: A re-examination of the "Leipzig wind profile" considering some relations between wind and turbulence in the frictional layer. *Tellus*, **2**, 125–129.

Lettau, H., 1969: Note on aerodynamic roughness-parameter estimation on the basis of roughness-element description. *J. Appl. Meteor.*, **8**, 828–832.

Lettau, H. H., 1962: Theoretical wind spirals in the boundary layer of a barotropic atmosphere. *Beitr. Phys. Atmos.*, **35**, 195–212.

Lindelöw, P., M. Courtney, R. Parmentier, and J.-P. Cariou, 2008: Wind shear proportional errors in the horizontal wind speed sensed by focused, range gated lidars. *Earth Environ. Sci.: Conf. Ser.*, **1**, 012 023 (10 pp).

Lindelöw-Marsden, P., 2007: D1. uncertainties in wind assessment with lidar. Tech. Rep. Risø-I-1234(EN), Risø National Laboratory, 55 pp.

Long, R. R., 1974: Mean stresses and velocities in the neutral, barotropic boundary layer. *Bound.-Layer Meteor.*, **7**, 475–487.

Lumley, J. L. and A. M. Yaglom, 2001: A century of turbulence. *Flow, Turbul. Combust.*, **66**, 241–286.

Mann, J., 1994: The spatial structure of neutral atmospheric surface-layer turbulence. *J. Fluid Mech.*, **273**, 141–168.

Mann, J., E. Dellwik, F. Bingöl, and O. Rathmann, 2007: Laser measurements of flow over a forest. *J. Phys.: Conf. Ser.*, **75**, 012 057 (7 pp).

Mann, J., et al., 2008: Comparison of 3D turbulence measurements using three staring wind lidars and a sonic anemometer. *Earth Environ. Sci.: Conf. Ser.*, **1**, 012 012 (6 pp).

Mildner, P., 1932: Über die Reibung in einer speziellen Luftmasse in den untersten Schichten der Atmosphäre (On the friction inside a particular air mass in the lowest layers of the atmosphere). *Beitr. Phys. Atmos.*, **19**, 151–158.

Monin, A. S. and A. M. Obukhov, 1954: Osnovnye zakonomernosti turbulentnogo peremeshivanija v prizemnom sloe atmosfery (Basic laws of turbulent mixing in the atmosphere near the ground). *Trudy Geofiz. Inst. AN SSSR*, **24 (151)**, 163–187.

Nissen, J. N., 2008: On the application of a numerical model to simulate the coastal boundary layer. PhD-thesis, Risø-PhD-39(EN), Risø National Laboratory, 110 pp.

Obukhov, A. M., 1946: Turbulentnost v temperaturnoj – neodnorodnoj atmosfere (Turbulence in an atmosphere with an non-uniform temperature). *Trudy Geofiz. Inst. AN SSSR*, **1**, 95–115.

Ohmstede, W. D. and J. F. Appleby, 1964: Numerical solution of the distribution of wind and turbulence in the planetary boundary layer. Meteor. Res. Note No. 8 DA Task 1-A-0-11001-B-021-08, 43 pp.

Panofsky, H. A., 1973: Tower micrometeorology. *Workshop on Micrometeorology*, D. A. Haugen, Ed., American Meteorology Society, 151–176.

Panofsky, H. A. and J. A. Dutton, 1984: *Atmospheric turbulence*. John Wiley & Sons, 397 pp.

Peña, A., C. B. Hasager, S.-E. Gryning, M. Courtney, I. Antoniou, T. Mikkelsen, and P. Sørensen, 2007: Offshore wind using remote sensing techniques. *J. Phys.: Conf. Ser.*, **75**, 012 038 (11 pp).

Petersen, E. L., N. G. Mortensen, L. Landberg, J. Højstrup, and H. P. Frank, 1998: Wind power meteorology. part II: Siting and models. *Wind Energy*, **1**, 55–72.

Prandtl, L., 1925: Bericht über Untersuchungen zur ausgebildeten Turbulenz (Report on the investigations of developed turbulence). *Zs. angew. Math. Mech.*, **5**, 136–139.

Prandtl, L., 1932: Meteorologische Anwendung der Strömungslehre (Meteorological application of fluid mechanics). *Beitr. Phys. Atmos.*, 188–202.

Reynolds, O., 1883: An experimental investigation of the circumstances which determine whether the motion of water in parallel channels shall be direct or sinous and of the law of resistance in parallel channels. *Philos. Trans. Roy. Soc. London*, **186**, 123–164.

Rossby, C. G. and R. B. Montgomery, 1935: The layers of frictional influence in wind and ocean currents. *Pap. Phys. Oceanogr. Meteor.*, **3 (3)**, 101 pp.

Seibert, P., F. Beyrich, S.-E. Gryning, S. Joffre, A. Rasmussen, and P. Tercier, 1998: Mixing height determination for dispersion modelling. *COST Action 710 – Final report*, B. E. A. Fisher, J. J. Erbrink, S. Finardi, P. Jeannet, S. Joffre, M. G. Morselli, U. Pechinger, P. Seibert, and D. J. Thompson, Eds., European Commission.

Seibert, P., F. Beyrich, S.-E. Gryning, S. Joffre, A. Rasmussen, and P. Tercier, 2000: Review and intercomparison of operational methods for the determination of the mixing height. *Atmos. Env.*, **34**, 1001–1027.

Smedman, A.-S., X. G. Larsén, U. Högström, K. K. Kahma, and H. Peterson, 2003: Effect of the sea state on the momentum exchange over the sea during neutral conditions. *J. Geophys. Res.*, **108**, (C11), 3367, DOI:10.1029/2002JC001 526.

Smith, D. A., M. Harris, A. S. Coffey, T. Mikkelsen, H. E. Jørgensen, J. Mann, and R. Danielian, 2006: Wind lidar evaluation at the danish wind test site in Høvsøre. *Wind Energy*, **9**, 87–93.

Smith, R. B., 2008: A K-theory of dispersion, settling and deposition in the atmospheric boundary layer. *Bound.-Layer Meteor.*, DOI: 10.1007/s10 546–008–9321–y.

Smith, S. D., 1980: Coeficcients of sea surface wind stress, heat flux, and wind profiles as function of wind speed and temperature. *J. Geophys. Res.*, **93**, 467–472.

Sørensen, P. B., 2005: Wake effect east of the Horns Rev offshore wind farm. Tech. Rep. Doc. no. 209918, Elkraft System, PSO - F&U 2002/FU2103, Eltra no. 4158, ELSAM-VU111, Elsam Engineering, 24 pp.

Steyn, D. G., M. Baldi, and R. M. Hoff, 1999: The detection of mixed layer depth and entrainment zone thickness from lidar backscatter profiles. *J. Atmos. Ocean. Technol.*, **16**, 953–959.

Stull, R. B., 1988: *An introduction to boundary layer meteorology.* Kluwer Academic Publishers, 666 pp.

Taylor, G. I., 1915: Eddy motion in the atmosphere. *Philos. Trans. Roy. Soc. London*, **215**, 1–26.

Tennekes, H., 1973: The logarithmic wind profile. *J. Atmos. Sci.*, **30**, 234–238.

Tetens, O., 1930: Ûber einige meteorologische begriffe (On some meteorological definitions). *Z. Geophys.*, **6**, 297–309.

Troen, I. and E. L. Petersen, 1989: *European wind atlas.* Risø National Laboratory, 656 pp.

Weisse, R. and C. Schneggenburger, 2002: The effect of different sea-state-dependent roughness parameterizations on the sensitivity of the atmospheric circulation in a regional model. *Mon. Wea. Rev.*, **130**, 1593–1600.

Yordanov, D., D. Syrakov, and G. Djolov, 1983: A barotropic planetary boundary layer. *Bound.-Layer Meteor.*, **25**, 363–373.

Zilitinkevich, S., P.-E. Johansson, D. V. Mironov, and A. Baklanov, 1998: A similarity-theory model for wind profile and resistance law in stably stratified planetary boundary layers. *J. Wind Eng. Ind. Aerodyn.*, **74–76**, 209–218.

Zilitinkevich, S. S., 1975: Resistance laws and prediction equations for the depth of the planetary boundary layer. *J. Atmos. Sci.*, **32**, 741–752.

Zilitinkevich, S. S., 1989: Velocity profiles, the resistance law and the dissipation rate of mean flow kinetic energy in a neutrally and stably stratified planetary boundary layer. *Bound.-Layer Meteor.*, **46**, 367–387.

Zilitinkevich, S. S. and D. V. Mironov, 1996: A multi-limit formulation for the equilibrium depth of a stably stratified boundary layer. *Bound.-Layer Meteor.*, **81**, 325–351.

Paper I: Offshore Wind Profiling using Light Detection and Ranging Measurements

Authors: **Alfredo Peña**, Charlotte Bay Hasager, Sven-Erik Gryning, Michael Courtney, Ioannis Antoniou, and Torben Mikkelsen

Wind Energy (2009) 12:105–124

Available at http://www3.interscience.wiley.com/journal/121414709/abstract

Paper II: Charnock's Roughness Length Model and Non-dimensional Wind Profiles Over the Sea

Authors: **Alfredo Peña**, and Sven-Erik Gryning

Boundary-Layer Meteorology (2008) 128:191–203.

Available at http://www.springerlink.com/content/281762l582n10582

Paper III: Measurements and Modelling of the Wind Speed Profile in the Marine Atmospheric Boundary Layer

Authors: **Alfredo Peña**, Sven-Erik Gryning, and Charlotte Bay Hasager

Boundary-Layer Meteorology (2008) 129:479–495.

Available at http://www.springerlink.com/content/ww522t05433184p2

Paper IV: Length Scales of the Neutral Wind Profile over Homogeneous Terrain

Authors: **Alfredo Peña,** Sven-Erik Gryning, Jakob Mann, and Charlotte Bay Hasager

Submitted to Journal of Applied Meteorology and Climatology

Paper V: Comparing Mixing-Length Models of the Diabatic Wind Profile over Homogeneous Terrain

Authors: **Alfredo Peña,** Sven-Erik Gryning, and Charlotte Bay Hasager

Submitted to Tellus B

Paper VI: Remote Sensing Observation Used in Offshore Wind Energy

Authors: Charlotte Bay Hasager, **Alfredo Peña**, Merete Bruun Christiansen, Poul Astrup, Morten Nielsen, Frank Monaldo, Donald Thompson, and Per Nielsen

IEEE Journal of Selected Topics in Applied Earth Observations and Remote Sensing (2008) 1:67–79

Available at http://ieeexplore.ieee.org/xpls/abs%5Fall.jsp?arnumber=4637883

Paper VII: Lidar Scanning of Momentum Flux in and above the Surface Layer

Authors: Jakob Mann, Michael Courtney, Ferhat Bingöl, **Alfredo Peña**, and Rozenn Wagner

Manuscript in preparation for journal submission

To get a copy, please send an e-mail to aldi@risoe.dtu.dk

Resumen en Español

Este documento de tesis está dividido en dos partes. La primera consiste de una sinopsis de los fundamentos, las ideas, y el progreso teorético del doctorado. Esta sinopsis está basada en una colección de artículos que están siendo preparados ó estan publicados en revistas especializadas durante los últimos tres años, los cuales constituyen la segunda parte del documento. Los artículos tienen como objetivo el análisis, la medición, descripción, y el modelaje del perfil de viento dentro y más allá de la capa superficial de la atmósfera, a través de la combinación de los métodos tradicionales para la medición de la velocidad del viento, como lo son los anemómetros de copa o los sónicos con las observaciones de lidars comerciales. Las observaciones del lidar son necesarias para la extensión de las mediciones realizadas con los instrumentos tradicionales, los cuales están instalados en mástiles meteorológicos localizados en el parque eólico Horns Rev en el Mar del Norte danés y en la estación nacional de pruebas de turbinas eólicas en Høvsøre, Dinamarca. Las técnicas de detección basadas en los lidars y en los anemómetros sónicos o de copa muestran un alto grado de correlación y correspondencia para las mediciones de velocidad de viento tomadas a distintas alturas donde las observaciones de los instrumentos se superponen, en ambos emplazamientos, y para un amplio rango de condiciones de estabilidad atmosférica.

Las mediciones de velocidad de viento, tomadas en los mástiles sobre terreno plano y homogéneo en Høvsøre y sobre el mar dentro de un sector libre de estelas y de la influencia de la costa en Horns Rev, son promediadas dentro de distintas condiciones atmosféricas, basadas en intervalos de longitudes de Obukhov, y estas revelan un buen grado de comparación con el perfil tradicional de viento de la capa superficial. Para el análisis de los perfiles de viento en Høvsøre es suficiente con escalar la velocidad de viento con la velocidad de fricción superficial, mientras que para el análisis de los perfiles en Horns Rev se necesita una nueva escala, debido a que la rugosidad superficial observada en el agua es variable. Esta nueva escala es acoplada con modelos de perfil de viento basados en el flujo de aire sobre mar que usan la teoría de la longitud de mezcla y son comparados con los perfiles de viento medidos con los anemómetros de copa y extendidos con las observaciones del lidar que alcanzan los 160 m sobre el nivel del mar en Horns Rev. Los modelos, que tienen en consideración la altura de la capa límite atmosférica, muestran una mejor correspondencia con las mediciones que cuando estas son comparadas con la teoría tradicional.

Las parametrizaciones basadas en la longitud de mezcla para el perfil neutro de viento que difieren de la teoría tradicional de la capa superficial revelan una buena correspondencia con las mediciones de escala de longitud basadas en mediciones de velocidad de viento hasta 300 m en Høvsøre y hasta 950 m basadas en el re-análisis del perfil de viento de Leipzig. Los perfiles de viento derivados de dichas parametrizaciones se desvían ampliamente del perfil logarítmico de viento, pero concuerdan mucho mejor con las mediciones de velocidad de viento. Las mediciones y parametrizaciones de escala de longitud son también comparadas con la longitud de escala derivada de un análisis espectral de mediciones de turbulencia hasta 160 m en Høvsøre, mostrando proporcionalidad entre ambas escalas de longitud.

Dos de las parametrizaciones para la longitud neutral de mezcla son corregidas para tener en cuenta la estabilidad de la atmósfera y son usadas para derivar modelos de perfil de viento. La comparación de estos modelos con las mediciones de velocidad de viento adquiridas a través de la combinación del lidar y los anemómetros de copa hasta 300 m en Høvsøre muestra mejores resultados que cuando las mediciones son comparadas con el perfil tradicional de viento de la capa superficial. Para el rango de condiciones de estabilidad, la altura de la capa límite se convierte en un parámetro de escala, el cual se deriva en base a flujos turbulentos de momento para las condiciones cercanas a neutras y estables, como también es derivada de las mediciones en Horns Rev, y en base a

perfiles de retro-dispersión de aerosoles observados con un ceilómetro para las condiciones inestables.

La técnica de medición del lidar es estudiada, no solamente en el contexto de mediciones de velocidad de viento, sino también para la estimación de algunas características de la turbulencia, tales como el flujo de momento. Este último muestra una alta concordancia comparado con las mediciones de turbulencia de los anemómetros sónicos en Høvsøre y las observaciones derivadas de gradientes de velocidad de viento y temperatura en Horns Rev, cuando los efectos de filtro derivados del amplio volumen de medición del lidar son tomados en cuenta.

Risø DTU is the National Laboratory for Sustainable Energy. Our research focuses on development of energy technologies and systems with minimal effect on climate, and contributes to innovation, education and policy. Risø has large experimental facilities and interdisciplinary research environments, and includes the national centre for nuclear technologies.

Risø DTU
National Laboratory for Sustainable Energy
Technical University of Denmark

Frederiksborgvej 399
PO Box 49
DK-4000 Roskilde
Denmark
Phone +45 4677 4677
Fax +45 4677 5688

www.risoe.dtu.dk